Summer 6-25-2010

Numerical Methods for Simulating Multiphase Electrohydrodynamic Flows with Application to Liquid Fuel Injection

Bret Van Poppel
United States Military Academy, vanpoppelb@gmail.com

Numerical Methods for Simulating Multiphase Electrohydrodynamic Flows with Application to Liquid Fuel Injection

by

Bret P. Van Poppel

B.S., U.S. Military Academy, 1992

M.S., Massachusetts Institute of Technology, 2001

A thesis submitted to the

Faculty of the Graduate School of the

University of Colorado in partial fulfillment

of the requirements for the degree of

Doctor of Philosophy

Department of Mechanical Engineering

2010

This thesis entitled:
Numerical Methods for Simulating Multiphase Electrohydrodynamic Flows with Application to Liquid Fuel Injection
written by
Bret P. Van Poppel
has been approved for the Department of Mechanical Engineering

Prof. John W. Daily

Prof. Olivier Desjardins

Prof. Kamran Mohseni

Dr. James Nabity

Prof. Gary Pawlas

Date

The final copy of this thesis has been examined by the signatories, and we find that both the content and the form meet acceptable presentation standards of scholarly work in the above mentioned discipline.

Van Poppel, Bret P. (Ph.D., Mechanical Engineeering)

Numerical Methods for Simulating Multiphase Electrohydrodynamic Flows with Application to Liquid Fuel Injection

Thesis co-directed by Prof. John W. Daily and Prof. Olivier Desjardins

One approach to small-scale fuel injection is to capitalize upon the benefits of electrohydrodynamics (EHD) and enhance fuel atomization. There are many potential advantages to EHD aided atomization for combustion, such as smaller droplets, wider spray cone, and the ability to control and tune the spray for improved performance. Electrohydrodynamic flows and sprays have drawn increasing interest in recent years, yet key questions regarding the complex interactions among electrostatic charge, electric fields, and the dynamics of atomizing liquids remain unanswered. The complex, multi-physics and multi-scale nature of EHD atomization processes limits both experimental and computational explorations.

In this work, novel, numerically sharp methods are developed and subsequently employed in high-fidelity direct numerical simulations of electrically charged liquid hydrocarbon jets. The level set approach is combined with the ghost fluid method (GFM) to accurately simulate primary atomization phenomena for this class of flows. Surface effects at the phase interface as well as bulk dynamics are modeled in an accurate and robust manner. The new methods are implemented within a conservative finite difference scheme of high-order accuracy that employs state-of-the-art interface transport techniques. This approach, validated using several cases with exact analytic solutions, demonstrates significant improvements in accuracy and efficiency compared to previous methods used for EHD simulations. As a final validation, the computational scheme is applied in direct numerical simulation of a charged and uncharged liquid kerosene jet. Then, a detailed numerical study of EHD atomization is conducted for a range of relevant dimensionless parameters to predict the onset of liquid break-up, identify characteristic modes of liquid disintegration, and report elucidating

statistics such as drop size and spray dispersion. Because the methodologies developed and validated in this work open new, simulations-based avenues of exploration within a broader category of electrohydrodynamics, some perspectives on extensions or continuations of this work are offered in conclusion.

Dedication

A substantial portion of this achievement must be attributed to the tireless efforts of my wife and partner, Christina A. F. Van Poppel, who has performed myriad roles over the years with elegance and grace, not the least of which include *friend, coach, mentor, disciplinarian, motivator, confidant*, and *emotional stabilizer.* I wish to dedicate the accomplishments and effort embodied by this document to her and our children, Henry William and Charlee Allison.

Acknowledgements

My two advisors, John and Olivier, are owed significant acknowledgement for their tireless efforts in providing consistently high-quality guidance, mentorship, direction, coaching, and friendship. Both advisors, along with Dr. Jim Nabity, provided me with an exceptional education. I am convinced that my experience would not have been better anywhere else.

Sharon Anderson, graduate coordinator, must be recognized for her superior efforts in doing her job far beyond its description and with little expectation of advancement–her spirit and commitment are truly admirable. I have personally benefitted from her diligence, expertise, and friendship. She has kept me on track–essential support for the finite-timeline provided by the U.S. Army.

A number of students have been instrumental and inspirational over the years, and the short list includes Mark Czajkowski, Bradley Spatafore, Kim Jasch, Jesse Capecelatro, Qi Guan, Fan Wang, Matt Turner, Kathleen Stynes, Bradley Davidson, Tom Stovall, Jill Cooper, Chris Deluca, Kevin Long and Alicia Baca.

Funding and sponsorship from the U.S. Army and U.S. Military Academy, as well as research funding provided by Army Research Office Contracts W911NF-08-C-0081 and W911NF-09-C-0157, is gratefully acknowledged.

Go Army!

Contents

Chapter

Tables

Table

Figures

Figure

Chapter 1

Introduction

1.1 Motivation

Over the past decade, there has been a growing amount of attention paid to the emissions from small engines in the size range of 200 cm^3 or smaller. In 2002 the EPA published a study claiming small engine emissions were responsible for 9% Hydrocarbons (HC), 4% Carbon monoxide (CO), 3% NOx, and 2% particulate matter from all mobile sources in the United States [1]. As a result, there is considerable interest in controlling emissions for these small engines. One of the main reasons small engines produce high emissions is that they are carbureted. Carburetors mix fuel with air for combustion, but they are incapable of providing precise fuel timing. These deficiencies lead to partial combustion and decreased fuel efficiency while increasing emissions. Direct fuel injection may reduce the incidence of these pollutants. However, the cost of implementation is a barrier to large scale adoption. Fuel injectors used in the automotive industry are too costly to be implemented on small engines, with the average cost falling in the range of $35 dollar per unit (USD). In order to keep the production cost profitable, costs will have to be substantially lower.

The cost of fuel injection is driven by both the need to pump the fuel to the injection pressure and to add parts for the injector head. A potential solution is to use integrated circuit technology to produce a cost effective MEMS fuel pump/atomizer, integrating a pump and injector. Micropumps have been designed to deliver small fluid volumes in a variety of systems ranging from chemical and biological assay systems, to propulsion systems for space

exploration. By integrating a micropump with the injection nozzles, a very compact and potentially economic device can be constructed.

Another approach to small-scale fuel injection, and one that serves as the focus of this research effort, is to capitalize upon the benefits of electrohydrodynamics (EHD) and enhance fuel atomization. The application of a strong electric field within the domain of interest has been demonstrated by many researchers. There are many possible benefits to EHD aided atomization for combustion, such as smaller droplets, wider spray cone, and the ability to control or "tune" the spray, both spatially and temporally, for improved performance. For these reasons and others, a numerical investigation of electrohydrodynamic atomization is proposed here.

Electrohydrodynamic flows and sprays have drawn increasing interest in recent years, yet key questions regarding the complex interactions among electrostatic charge, electric fields, and the dynamics of atomizing liquids remain unanswered. DNS of realistic liquid breakup are challenging due to the computational expense involved. Combining recently advanced numerical simulation tools with validation experiments will permit exploration of EHD atomization with unprecedented accuracy and detail. The outcomes of this research will be a fundamental understanding of the dynamics of EHD atomization, and a point of departure for robust modeling of EHD sprays using advanced numerical methods or reduced order models.

In this work, the level set approach is combined with the ghost fluid method (GFM) to model primary atomization of an electrically charged liquid hydrocarbon fuel. A high electric Reynolds number regime is assumed, and surface effects as well as bulk dynamics are modeled. The model is implemented within a conservative finite difference scheme of high-order accuracy that employs a state-of-the-art interface transport technique. This approach, validated using several cases with exact analytical solutions, demonstrates significant improvements in accuracy and efficiency compared to previous methods used for EHD modeling. The model is applied in direct numerical simulation of a charged and uncharged

liquid Kerosene jet. Finally, a detailed numerical study of EHD atomization is conducted for a range of relevant dimensionless parameters to predict the onset of breakup, identify characteristic modes of liquid disintegration, and report elucidating statistics such as drop size and spray dispersion.

1.2 Achievements

The principal goal of this work is to develop numerical methods to accurately simulate electrohydrodynamic atomization of liquid hydrocarbon fuels, thereby enabling detailed computational studies of primary atomization phenomena for this class of flows. Several advances in the state-of-the-art can be reported:

1. A sharp numerical scheme for multiphase electrohydrodynamic (EHD) flows has been developed. This novel computational scheme enables high-fidelity, fully three-dimensional direct numerical simulation (DNS) of liquid hydrocarbon sprays influenced by electric fields and electric space charge. This tool permits unprecedented investigation of the fundamental physics and processes involved in EHD with application to combustion-type sprays. The key components of this scheme include:

    * An accurate and efficient solution for the electric potential Poisson equation. The electric potential Poisson equation contains EHD interface boundary conditions, which are implemented using the ghost fluid method (GFM).

    * A numerically sharp and accurate implementation for the EHD interface boundary conditions. A mathematical formulation for the pressure jump that includes the EHD stresses is derived, and subsequently the GFM is employed to develop an efficient numerical scheme to compute the normal and tangential electric field components at the phase interface. Again using the GFM, the EHD jump conditions are used to solve the pressure Poisson equation.

    * An efficient implementation of the Coulomb force.

2. Using this novel scheme, a detailed numerical study of primary atomization phenomena for charged liquid hydrocarbon jets has been performed and a clear picture of the atomization process has been laid out. A range of relevant parameters, including Reynolds number, Weber number, and electro-inertial number, were considered in this study. Simulations were performed for high electric Reynolds number liquid jets, striving to explore principal effects of electro-inertial number and liquid Weber number on the onset of atomization and drop-size distribution. The density ratio was set to $\rho_l/\rho_g = 50$, which is commonly observed in Diesel engines and low enough to avoid numerical issues that can plague higher density ratio simulations. A low Reynolds number was chosen to reduce the likelihood of natural breakup in an uncharged case so that this simulation may be used as a baseline for qualitative assessment. The numerical study revealed that the effects of aerodynamic lift are enhanced, with the orientation of liquid structures deflected toward the upstream end of the computational domain. The axial location at which atomization commences moves progressively upstream as the electro-inertial number, and therefore the level of electrical charge, increases. Structures dislodged from the liquid core increase with greater electro-inertial number, consistent with increased Coulombic repulsion and electrical surface stresses. The drop size data suggests a bi-modal distribution, with some preference for larger sized structures. Statistical results for simulations show reasonable agreement with models, even in the one-dimensional formulations presented, and suggest that liquid Weber number, electro-inertial number, and density ratio are principal determinants of atomization onset location as well as drop size. In the absence of detailed experimental data on primary atomization, statistics for velocity and liquid volume fraction are of great value and have therefore been reported here.

3. This work establishes a reference point for subsequent work, including the following relevant research opportunties:

    * Modeling secondary atomization modeling, which may incorporate evaporation models, Lagrangian particle tracking (LPT), and possibly "relaxed" surface charge on droplets;
    * Modeling different electro-physical classifications of liquids, in particular ionic or polar liquids with much higher electrical conductivities, for propulsion or spraying applications;
    * Simulating the complex electrohydrodynamic flows within a charge injecting nozzle, incorporating diffusion effects as well as modeling the electrochemical processes that introduce electric charge in the dielectric liquid;
    * Simulating multiple orifice, pulsed injection systems. Considering the challenges of single orifice systems, multiple-orifice designs offer a practical alternative. Simulating multiple orifice systems is a straightforward extension of this work, and would include droplet interactions from adjacent spray nozzles.

1.3 Organization of Thesis

This thesis is organized in chapters of relevant information. Chapter 2 provides a detailed background to frame the fundamentals of electrohydrodynamics, the challenges of atomization, a survey of previous relevant work, a summary of the governing continuum equations, the NGA code that is capable of simulating three-dimensional and turbulent multiphase flows, and the research objectives for this work. Chapter 3 discusses the numerical methods and modeling approach employed in simulating EHD atomization. Chapter 4 reports the results of a detailed numerical study of atomization of electrically charged liquid hydrocarbon fuels. Chapter 5 summarizes the work, and addresses conclusions and recommends future work.

Chapter 2

Simulating Electrohydrodynamic Atomization

2.1 Overview

In this chapter, a survey of relevant work in the areas of electrospraying, electrohydrodynamics, and charge injection atomization is summarized. The governing continuum equations for variable density hydrodynamic flows and electromechanics are presented, and relevant dimensionless parameters and time scales are identified. The NGA code, a high order conservative finite difference Navier-Stokes solver with state-of-the-art interface transport techniques, is introduced, and the chapter concludes with specific research objectives.

2.2 Previous Work

While the exploration of the effects of electric fields upon flowing liquids dates back to the seventeenth century, the seminal work of Lord Rayleigh is considered to be the most well-documented point of departure for the general subject that is now known as electrohydrodynamics, or EHD. John William Strutt, later designated Lord Rayleigh, revealed the competing forces and resulting dynamics of a liquid drop that is radially stressed by an applied electric field in his 1882 paper [150].

In 1909, Robert Millikan and Harvey Fletcher performed their now famous oil-drop experiment. The experiment strived to measure charge of the electron. The experiment entailed balancing the downward gravitational force with the upward buoyant and electric forces on tiny charged droplets of oil suspended between two metal electrodes. Since the

density of the oil was known, the droplets' masses, and therefore their gravitational and buoyant forces, could be determined from their observed radii. Using a known electric field, Millikan and Fletcher could determine the charge on oil droplets in equilibrium. By repeating the experiment for many droplets, they confirmed that the charges were all multiples of some fundamental value, and subsequently calculated the charge of an electron [113].

In early electrohydrodynamic study, Zeleny observed for electrically charged conducting liquids through a capillary that the liquid dispersed outwardly into a spray of small droplets. For perfectly conducting liquids, G.I. Taylor provided a theoretical explanation for the conical spray shape in Zeleny's work. Dichotomous behavior was observed among perfectly conducting and perfectly insulating materials. When non-conducting drops suspended in non-conducting (dielectric) liquids were deformed by a constant electric field, they assumed an oblate shape (flattened sphere). The deformation observed in these dielectric liquids resulted from polarization forces, since free charges were absent and the electric stresses were normal to the surface. By contrast, drops formed from perfectly conducting drops assumed a prolate (elongated sphere) [207, 183, 159]. Subsequent to the early efforts of Taylor and Zeleny, these jets of electrically-driven conducting liquids have been called Taylor cones and now contribute to a wide variety of electrospraying applications [8].

EHD surface instabilities have been studied using a variety of liquids. Until the 1960's most work focused on the behavior of perfect conductors or perfect insulators (non-polar liquids such as benzene). This began to change following studies on poorly conducting liquids, also called leaky dielectrics. One of the first efforts to study the region between true insulators and true conductors was conducted by Allan and Mason [2]. The leaky dielectric model, originally proposed by G.I. Taylor and later extended by J.R. Melcher, assumes a liquid has a low electrical conductivity such that a bulk charge density may not exist for non-inertial flows or stationary systems. However, a surface charge density can be induced at a fluid-fluid interface [110]. The model assumes that the charge carriers are of an ionic nature [159].

2.2.1 Experimental and Theoretical Work

Kim and Turnbull performed pioneering work in the field of electrohydrohynamics by enhancing the atomization of dielectric liquids for combustion applications. They used a similar technique to the previously demonstrated method for electrostatic spraying of conducting and semi-conducting liquids, whereby a sharp-tipped metallic electrode is charged to a high potential and immersed in a semi-insulating liquid. The experimental apparatus employed a very fine-tipped needle immersed in a low conducting (Freon 113) liquid and embedded in a nozzle housing. The researchers postulated three theoretical possibilities for the observed phenomena: a. emission of electrons (negative electrode); b. field ionization (positive electrode); c. corona discharge [88]. The authors demonstrate that high electric fields produce fine jets and subsequently breakup into drops.

Kelly developed a statistical model for electrospraying of liquid metals and electrically conducting liquids. The model predicted that charge-to-mass ratio varied as the inverse square of drop radius [84]. Kelly later extended his previous research by performing theoretical and experimental work demonstrating that the achievable drop size in Newtonian liquid sprays is governed by the magnitude of free charge on the surface of drops. The implications for the technique of charge injection included a wide range of flow rates and the 'tunability' of spray character and drop size [87]. Kelly later described an electrostatic fuel atomizer to inject charge into Jet-A. Approximately 10kV was applied between the electrodes to produce droplet distributions with SMDs between 38 and 76 μm. The smallest droplets were produced at the highest pressure conditions tested (4.4 to 5.9 bar). The spray contained two droplet zones; a central core and an outer sheath. It is the inner core that contained the largest droplets. The outer sheath contained a large number of droplets as small as 4.3 μm, but concluded that drops on the order of 50 μm comprised a very low proportion of the total volume. This conclusion suggests that a simple charge injector may not produce a spray of sufficient fineness to fire a spark ignition engine with a Kerosene-based fuel such as JP-8.

Lehr and Hiller used experimental methods to confirm the observations of Kim and Turnbull, and Kelly. They predicted the limit of charge density and therefore droplet size. They used the "spray triode" system for stationary and moving operational conditions, and predicted that corona discharge limited the charge density to 5 C/m^3 [97].

Felici performed an analytical investigation of the possibilities of transferring charge from a metallic surface to a dielectric liquid. His analysis suggested that the injected charge results from electrochemical reactions and can be a significant source of electrification of the liquid. The development of a "double layer" contributed to the charging of available free ions in the dielectric liquid, since it was assumed that even insulating liquids have a non-zero electrical conductivity [53].

Rulison and Flagan experimentally demonstrated linear arrays of Taylor cones to ascertain the possiblity of increasing the liquid flowrate, and thereby increase the specific impulse and thrust that can be generated by electrosprays for micro-scale propulsion applications [156]. In related work, Rulison and Flagan reported experimental results on droplet production by electrospray atomization of electrolytic solutions. The spray resulted from the formation of liquid droplets at the tip of a Taylor cone. Experiments used sodium iodide dissolved in n-propyl alcohol to demonstrate that as the solution concentration increases, the volumetric flow rate decreases, the electrical current increases, and the aerosol size distribution of the solid residue particles shifts to smaller sizes. This work asserted that there is no complete analytical description of the electrospray. The investigators offered some analytical insights addressing the behavior of its three distinct components: the Taylor cone, the jet, and the charged droplet spray [157].

Shrimpton explored the charge injection technique by comparing insulating (dielectric) liquids and semi-conducting liquids. Flow visualization and phase Doppler anemometry measurements demonstrated similarities between the two classes of liquids under the influence of electrostatic enhancement. For insulating liquids, the quality of atomization was shown to improve with increasing flow rate under the dual action of greater aerodynamic forces and

higher spray specific charge. The work demonstrated combustion of these charged hydrocarbon sprays, revealing efficient and stable combustion due to multiple benefits of electrostatically aided atomization [170]. In later work, Shrimpton and co-workers experimentally investigated sub-critical and supercritical regimes to identify limitations of each operational mode. Subcritical regime did not produce fine sprays. Supercritical regime was limited by partial discharge outside the nozzle, but fine droplets were produced. The limit of spray specific charge in the supercritical regime increased with increasing nozzle velocitites, thereby enhancing atomization by greater electrostatic and aerodynamic forces [171]. A separate set of experiments explored electrostatic atomizer design and subsequently quantify the maximum electrical charging that can be achieved for different nozzle-charger geometries. The atomizer internal geometry, as well as modifications to the electrical characteristics of the atomizer, yielded substantial improvements in atomization [172]. More recently, Shrimpton and co-workers have pursued experimental work with multiple orifice nozzles and pulsed flow atomizers [90].

Zhang and co-workers conducted an experimental investigation of dielectric liquids under the action of a high applied electric field. 10 different silicone oils with similarly low electrical conductivity (10^{-13} S/m) and a range of viscosities were flown through a capillary needle and subjected to a range of electric field strengths up to 1.5 kV/mm. The low electrical conductivity and relatively high electrical relaxation time produced only unsteady transient jets [208].

Grimm conducted an experimental study of the evaporation and discharge dynamics of highly charged droplets generated by electrospray ionization from n-heptane, n-octane, and p-xylene doped with Stadis-450, a conductivity enhancing agent. A phase Doppler anemometer (PDA) characterized individual droplets moving through a uniform electric field within an ion mobility cell according to size, velocity, and charge. Results were compared to previous experiments, theoretical models for droplet evaporation and discharge, and predictions from the Rayleigh model [66].

Yule and Shrimpton experimentally investigated the use of electrostatics to control a fuel spray. The so-called "charge injection" method of applying a high-strength electric field and adding charge carriers to hydrocarbon oils of low electrical conductivity was evaluated with experiments and subsequently used to validate two computer models. Results revealed that this technique can be employed at flow rates commensurate with practical combustion systems. Additionally, the charge injection technique was useful for enhanced atomization of dielectric liquids, such as hyrdrocarbon oils [204].

2.2.2 Numerical Modeling

Shrimpton, in a continuation of the numerical work published in 2003, used numerical methods to model the charge injection method and its applicability in direct injection spark ignition (DISI) engines. The model extended previous 2D model to include multiple mechanisms for charge transport and an evaporation model. The modeling work predicted spray dispersion and evaporation rate, and it suggested that electrostatic techniques can serve as an effective method to tune the spray for some injection-engine load strategies in the DISI engines. This work also postulated that the electrostatic activation of fuel sprays injected late during the compression stroke encouraged secondary atomization, whereas little benefit was observed when the fuel was injected early during the intake stroke. The results reported that the optimal charge densities to impart to the fuel are between 5 and 10 C/m^3 [168].

Carretero and co-workers employed numerical methods to model a Taylor cone electrospray. The model employed local phenomenon in spherical coordinates and "exact" free surface boundary conditions to preserve the equilibrium shape of the jet. Charge conservation was modelled with a normal electric field (conduction current from bulk flow to the surface) and tangential electric field (rate of change of conduction current in the axial direction). This assumed no free volumetric charge within liquid. Surface charge was conserved with temporal and spatial components [17].

Nhumaio and co-workers modeled electrically charged spray injected into aDISI engine

to evaluate the effects of various cylinder wall materials. The spray was modeled as emitted from a plain orifice electrostatic atomizer in the EPISO code. Researchers found that dielectric in-cylinder materials improved spray characteristics of charged sprays, and that charge drainage required for metallic surfaces yielded poor spray quality [128].

Balachandran reported results of numerical modeling of electrically charged viscous fuel flow in a charge injection scheme. The model demonstrated the importance of the role of the field emission of charge carriers from the charging electrode tip. The model accounted for the two principal constituents of the total current–spray current and the leakage current that is conducted away by the nozzle body. The model predicted that the space charge density and its corresponding electric field strongly affects the atomization of the expelled jet [5].

Baygents and co-workers conducted a detailed numerical study of EHD deformations and interactions in paris of droplets. The drops were asumed to be charge-free in the presence of an externally applied electric field. The study explored the leaky dielectric model and a range of conductivities and permittivoties. Dielectrophoretic effects were analyzed for the two-drop systems, revealing oblate or prolate deformations in agreement with Taylor's theory and the leaky dielectric model. All simulations were performed under axisymmetric assumptions, with a plane of symmetry to represent the second drops [10].

Collins and co-workers conducted a detailed numerical investigation of the breakup dynamics of an incompressible, Newtonian liquid with a high electrical conductivity that is stressed by aerodynamic forces of a surrounding gas and a radial electric field. Relevant parameters were studied over a wide range of Ohnesorge and electric Bond numbers. Effects of surface charge on interface overturning, as well as effects of electrostatic field on pinch-off and child drop formation were reported. Two numerical algorithms were employed in this study include: a three-dimensional axisymmetric Galerkin FEM was used to solve axisymmetric Navier-Stokes equations and Laplace's equation; and a hybrid Galerkin FEM coupling one-dimensional slender-jet with a three-dimensional axisymmetric representation

of the electric field [31].

Tomar and co-workers developed a numerical methodology to simulate two-phase electrohydrodynamic flows using a volume-of-fluid approach. The electric force is modeled for highly conducting liquids and the dichotomous situation of highly insulating liquids. The continuum model assumes an electric field is applied to the liquid, and the subsequent electromechanical coupling manifests at the phase interface only. In the case of a highly conducting material, this comes as a natural consequence of the high electrical conduction and corresponding short charge relaxation time. In the case of the dielectric liquid, the authors argue that the interface dynamics result from polarization forces of the applied field. The authors employ a weighted harmonic mean interpolation scheme to smoothen the electric properties in at the interface. A coupled level set and volume-of-fluid (CLSVOF) algorithm is used for tracking the phase interface, and the continuum surface force (CSF) method is used for the electric surface forces. The work does not stipulate any immediate applications or flow classifications for which the numerical model may be employed or uniquely suited [186].

Bjorklund presented work that demonstrated the combination of the level-set method and the ghost-fluid method for two-dimensional simulations of charge-free droplets immersed in an externally applied electric field. employed to simulate two-dimensional droplet dynamics in the presence of an electric field. Simulations revealed good accuracy and efficiency. The methods were demonstrated in the prediction of droplet breakup and coalescence due to the electrically induced forces [13].

Most recently, Guildenbecher, in his PhD thesis, reported no observed effects of electric charge on *secondary atomization* for either dielectric or conducting drops. He recommended DNS to fully elucidate the role of electrostatics in *primary atomization* and subsequently employ DNS results to develop predictive models for EHD atomization [69, 68].

2.2.3 Assessment of previous work

No reports of three-dimensional modeling of primary atomization mechanisms for multiphase, multiphysics electrohydrodynamics or charge injection have been found in the literature. Shrimpton [168] reported a robust model of secondary atomization that included evaporation, but results were shown as two-dimensional. Collins *et al* [31] reported axisymmetric results using advanced numerical methods and meshing techniques, but the liquid was assumed to be a perfect conductor moving through an applied electric field, thereby reducing the investigation to one governed by Laplace's equation (instead of Poisson's equation) for the electric field. This effort also restricted the investigation to the interaction of capillary and viscous forces and electrostatic effects at the liquid-gas interface. Tomar and co-workers report interface-tracking numerical techniques for electrohydrodynamic flows whereby the electromechanical coupling occurs exclusively at the phase interface. As in [31], the applied electric potential and corresponding electric field are governed by Laplace's equation in the absence of free space charge held in the liquid volume. Additionally, the choice of CSF methods to model the electric surface forces and surface discontinuities requires a fairly fine mesh to achieve reasonable accuracy, especially in regions of high gradients. Numerical methods that employ techniques to directly account for material discontinuities are expected to yield improvements in both accuracy and efficiency.

2.3 Governing Equations

In EHD flows, intertial, viscous, capillary, and electric forces are relevant and contribute to the behavior of the system. Conservation of mass and momentum for a variable density, low Mach number flow are given as

$$\frac{\partial \rho}{\partial t} + \nabla \cdot (\rho \boldsymbol{u}) = 0, \tag{2.1}$$

$$\frac{\partial \rho \boldsymbol{u}}{\partial t} + \nabla \cdot (\rho \boldsymbol{u} \otimes \boldsymbol{u}) = -\nabla p + \nabla \cdot (\boldsymbol{\sigma^f} + \boldsymbol{\sigma^e}) + \boldsymbol{g}. \tag{2.2}$$

where $\boldsymbol{u}$ is the velocity field, p is the hydrodynamic pressure, ρ is the mass density, $\boldsymbol{g}$ is gravitational acceleration, and μ is the dynamic viscosity. The viscous stress tensor, $\boldsymbol{\sigma^f}$ is given by

$$\boldsymbol{\sigma^f} = \mu\left(\nabla\boldsymbol{u} + \nabla\boldsymbol{u}^t\right) - \frac{2}{3}\mu\nabla\cdot\boldsymbol{u}\mathbb{I}, \tag{2.3}$$

with $\mathbb{I}$ the identity tensor. The Maxwell stress tensor, $\boldsymbol{\sigma^e}$, and an equivalent electric body force, $\boldsymbol{f_e}$, are described by

$$\boldsymbol{\sigma}^e = \epsilon\boldsymbol{E}\boldsymbol{E} - \frac{\epsilon}{2}\boldsymbol{E}\cdot\boldsymbol{E}\left(1 - \frac{\rho}{\epsilon}\frac{\partial\epsilon}{\partial\rho}\right)\mathbb{I}, \tag{2.4}$$

$$\boldsymbol{f_e} = q\boldsymbol{E} - \frac{1}{2}\boldsymbol{E^2}\nabla\epsilon + \nabla\left[\frac{1}{2}\rho\frac{\partial\epsilon}{\partial\rho}\boldsymbol{E}^2\right], \tag{2.5}$$

where ϵ is the electric permittivity, q is a volumetric electric charge density, and $\boldsymbol{E}$ is the electric field vector. The three components of $\boldsymbol{f_e}$ represent the Coulomb force, the dielectric force, and the electrostrictive force, respectively. The electric displacement vector is assumed to vary linearly with the electric field vector, as

$$\boldsymbol{D} = \epsilon\boldsymbol{E}. \tag{2.6}$$

The electric field vector, $\boldsymbol{E}$, is the gradient of the scalar electric potential, ϕ, and the Gauss law can be employed for a dielectric material to relate the electric displacement vector to the volumetric charge, as

$$\boldsymbol{E} = -\nabla\phi, \tag{2.7}$$

$$\nabla\cdot\boldsymbol{D} = \nabla\cdot\epsilon\boldsymbol{E} = -\nabla\cdot(\epsilon\nabla\phi) = q. \tag{2.8}$$

The electric field is also irrotational, and therefore

$$\nabla\times\boldsymbol{E} = 0. \tag{2.9}$$

The electric charge conservation equation is described by

$$\frac{\partial q}{\partial t} + \nabla\cdot\boldsymbol{J} = 0, \tag{2.10}$$

where $\boldsymbol{J}$ is the current density. The current density, $\boldsymbol{J}$, can be expressed by its components as

$$\boldsymbol{J} = \mu_i q \boldsymbol{E} - D_i \nabla q + q\boldsymbol{u}, \tag{2.11}$$

where D_i is the molecular diffusion coefficient.

2.4 Boundary conditions

The interface boundary and jump conditions are essential to capturing the dominant mechanisms influencing the flow and atomization. While the velocity and tangental electric field components are continuous across the interface, the mass density, viscosity, and electric displacement vector experience jumps, described by

$$[\boldsymbol{u} \cdot \boldsymbol{n}]_\Gamma = 0, \tag{2.12}$$

$$[\boldsymbol{u} \cdot \boldsymbol{t}_i]_\Gamma = 0 \qquad i = 1, 2, \tag{2.13}$$

$$[\rho]_\Gamma = \rho_l - \rho_g, \tag{2.14}$$

$$[\mu]_\Gamma = \mu_l - \mu_g, \tag{2.15}$$

$$[\epsilon]_\Gamma = \epsilon_l - \epsilon_g, \tag{2.16}$$

$$[\boldsymbol{D}]_\Gamma = \boldsymbol{n} \cdot [\epsilon \boldsymbol{E}]_\Gamma = q_s, \tag{2.17}$$

$$\boldsymbol{n} \times [\boldsymbol{E}]_\Gamma = 0, \tag{2.18}$$

where $[(\cdot)]_\Gamma$ represents the jump of "$(\cdot)$" across the interface, Γ, and for example, $[\boldsymbol{D}]_\Gamma$ represents the jump of the electric displacement vector across the interface, $\boldsymbol{n}$ and $\boldsymbol{t}$ represent the normal and tangential vector components at the interface and q_s the surface charge. A direct consequence of the irrotational jump condition, Eq. (2.18), ensures that the tangential components of the electric field, and therefore the electric potential, ϕ, are continuous,

$$[E_{t_1}]_\Gamma = 0 \quad [E_{t_2}]_\Gamma = 0, \tag{2.19}$$

$$[\phi]_\Gamma = 0. \tag{2.20}$$

The pressure interface jump condition includes contributions from hydrodynamic pressure, viscous, electric and surface tension forces, and is represented as

$$-[p]_\Gamma + [\boldsymbol{n}^\mathsf{T} \cdot (\boldsymbol{\sigma}^e + \boldsymbol{\sigma}^f) \cdot \boldsymbol{n}]_\Gamma = -\gamma\kappa,$$

$$[p]_\Gamma - 2[\mu]_\Gamma \boldsymbol{n}^\mathsf{T} \cdot \nabla \boldsymbol{u} \cdot \boldsymbol{n} - \gamma\kappa = \left[\frac{1}{2}\epsilon E_n^2\right]_\Gamma - \left[\frac{1}{2}\epsilon E_{t_i}^2\right]_\Gamma, \tag{2.21}$$

where $[p]_\Gamma$ is the jump across the interface, γ the surface tension coefficient, and κ the local interface curvature. Superscripts l and g represent quantities in the liquid and gas phases, respectively. The tangential shear stress balance yields

$$[\boldsymbol{n}^\mathsf{T} \cdot (\boldsymbol{\sigma}^e + \boldsymbol{\sigma}^f) \cdot \boldsymbol{t_i}]_\Gamma = 0, \tag{2.22}$$

$$\left[\boldsymbol{n}^\mathsf{T} \cdot (\boldsymbol{\sigma}^f) \cdot \boldsymbol{t_i}\right]_\Gamma + q_s \boldsymbol{E} \cdot \boldsymbol{t_i} = 0. \tag{2.23}$$

The conservation of charge at the interface is described by

$$[\boldsymbol{J} \cdot \boldsymbol{n}]_\Gamma + \nabla_s \cdot \boldsymbol{J_s} = (\boldsymbol{n} \cdot \boldsymbol{u})[q]_\Gamma - \frac{\partial q_s}{\partial t} - \boldsymbol{u_s} \cdot \nabla_s q_s + q_s \boldsymbol{n} \cdot (\boldsymbol{n} \cdot \nabla)\boldsymbol{u}, \tag{2.24}$$

where $\boldsymbol{J_s}$ is the surface current density, $\boldsymbol{u_s}$ the interface surface velocity, and ∇_s represents a surface gradient operator.

2.5 Relevant Time Scales and Non-dimensional Parameters

The following list defines and describes some of the relevant process time scales and dimensionless parameters of electrohydrodynamics. The *transport time*, τ, represents the typical times for inertial processes. With representative length, l, and velocity, u, scales, the transport time is given by

$$\tau = \frac{l}{u}. \tag{2.25}$$

The *charge relaxation time*, τ_e, represents the typical time for volumetric charge, q, to decay. Two principal mechanisms account for charge decay, the first of which is the neutralization

of charge by charge carriers in the fluid. This mechanism usually dominates in liquids with conductivity greater than 10^{-12} S/m. The second mechanism is mutual repulsion of like charges, which applies to highly insulating liquids and most gases. Both forms of τ_e are provided below, corresponding to the first and second mechanisms described here. A dimensionless parameter comparing the relative importance of charge decay by each mechanism, $\mathrm{N}_{\sigma q}$, is also introduced [33], as

$$\tau_e = \frac{\varepsilon}{\sigma}, \tag{2.26}$$

$$\tau_e = \frac{\varepsilon}{q\mu_i}, \tag{2.27}$$

$$\mathrm{N}_{\sigma q} = \frac{\sigma}{q\mu_i}. \tag{2.28}$$

The *viscous diffusion time*, τ_v, describes processes related to viscosity by

$$\tau_v = \frac{\rho l^2}{\mu}. \tag{2.29}$$

The *molecular diffusion time*, τ_d, represents the time for ionic diffusion processes,

$$\tau_d = \frac{l^2}{D_i}. \tag{2.30}$$

The *Reynolds Number* compares hydrodynamic inertial to viscous process times,

$$\mathrm{Re} = \frac{\rho \mathbf{u} l}{\mu}. \tag{2.31}$$

The *Electric Reynolds Number*, Re_e, compares charge relaxation and inertial time scales. For large values of RE_e, volumetric charge density will remain in the bulk of the liquid, and values much less than one can be treated as fully relaxed. Two forms are given: one for conduction dominated processes and one to represent space charge dominated processes. The ratio of conduction to ion mobility time scales, given above in Eq. (2.28) as $\mathrm{N}_{\sigma q}$, determines which form of Re_e will be used.

$$\mathrm{Re}_e = \frac{\tau_e}{\tau} \quad = \quad \frac{\varepsilon u}{l\sigma} \quad = \quad \frac{\varepsilon u}{l q \mu_i} \tag{2.32}$$

The *Electric Bond Number*, N_E, compares the importance of electrostatic and capillary forces, as

$$\mathrm{N}_E = \frac{\varepsilon E^2 l}{2\gamma}. \tag{2.33}$$

In terms of volumetric space charge, q, the electric field can be scaled as $E \approx \frac{ql}{\varepsilon}$, and subsequently provide an alternative form of the electric Bond number for situations where volumetric space charge dominates over an applied electric field or when there exists no externally applied electric field

$$\mathrm{N}_{E_q} = \frac{(q)^2 l^3}{2\gamma\varepsilon}. \tag{2.34}$$

The *Ohnesorge Number*, O_h, is a common dimensionless number in two-phase atomizing flows. It compares the relative importance of viscous and capillary forces, given by

$$\mathrm{O}_h = \sqrt{\frac{\mu^2}{\gamma\rho l}}. \tag{2.35}$$

The *Electroviscous number*, N_{ev}, compares the relative importance of electrostatic forces–usually the Coulomb force–to inertial forces.

$$\mathrm{N}_{ev} = \frac{\varepsilon E^2 l}{\mu u} \approx \frac{(q)^2 l^3}{\varepsilon\mu u} \tag{2.36}$$

The *Electroinertial number*, N_{ei}, compares the relative importance of electrostatic and inertial forces, described by

$$\mathrm{N}_{ei} = \frac{\varepsilon E^2}{\rho u^2} \approx \frac{(q)^2 l^2}{\varepsilon\rho u^2}. \tag{2.37}$$

A relevant scaling factor for pressure and velocity are given as [159]

$$P^* = \varepsilon_0 E_0^2, \tag{2.38}$$

$$u_e^* = \frac{qlE_0}{\mu}. \tag{2.39}$$

Table 2.1: Relevant Non-dimensional parameters and scaling factors

Parameter	*Symbol*	*Relationship*	*Force Ratio*
Reynolds	Re	$\frac{\rho \mathbf{u} \mathbf{l}}{\mu}$	inertia to viscous
Charge decay	$N_{\sigma q}$	$\frac{\sigma}{q\mu_i}$	conduction to SCL relax
Elec Reynolds	Re_e	$\frac{\varepsilon U}{l\mu}$	convection to electrostatic relax
Ohnesorge	O_h	$\frac{\mu}{\sqrt{\gamma \rho l}}$	viscous to capillary
Elec Bond	N_E	$\frac{\varepsilon E^2 l}{2\gamma}$	coulomb to capillary
Elec Bond, SCL	N_{E-scl}	$\frac{(q)^2 l^3}{2\gamma\varepsilon}$	space charge to capillary
Electroviscous	N_{ev}	$\frac{\varepsilon E^2 l}{\mu u} \approx \frac{(q)^2 l^3}{\varepsilon \mu u}$	coulomb to viscous
Electroinertial	N_{ei}	$\frac{\varepsilon E^2}{\rho u^2} \approx \frac{(q)^2 l^2}{\varepsilon \rho u^2}$	electrostatic to inertial
Pressure	P^*	$\varepsilon_0 E_0^2$	scale factor
Electric velocity	u_e	$\frac{q l E_0}{\mu}$	scale factor
Surface charge	q^*	$\varepsilon_0 E_0$	scale factor

2.6 NGA Code

Because primary atomization represents a challenge for experimentalists, numerical modeling should provide a much needed alternative. However, numerical studies of primary atomization have also been very sparse. To simulate two-phase flows, various techniques have been developed, that all enjoy some benefit and suffer from limitations. Because no clear gold standard has emerged on how to conduct a numerical simulation of complex two-phase flows, the number of direct numerical studies of primary atomization remains limited. Several key issues remain, such as the discontinuous nature of the flow properties across the phase-interface, the singularity of the surface tension forces, and the very large range of scales involved in atomization [48].

Previous work aiming at extending high order fully conservative numerical algorithms to complex reacting turbulent flows ultimately led to the development of an efficient multi-physics code or arbitrary accuracy has been developed. The code, named NGA, has been used in numerous DNS and LES studies including liquid atomization, spray dynamics, spray combustion, premixed, partially-premixed, and non-premixed turbulent jets and combustion

in technical devices, such as large-scale furnaces, internal combustion engines, and aircraft engine afterburners. This accurate and robust numerical tool provides a unique platform upon which physical phenomena can be studied through detailed simulations, and new LES models can be developed and tested [48]. NGA is fully parallelized using Message Passing Interface (MPI). NGA extends the family of high order fully conservative finite difference schemes proposed by Morinishi and Vasilyev [115, 116, 189] to variable density low-Mach number flows [40, 38, 48]. These schemes, tailored for DNS and LES, provide excellent accuracy, while retaining exceptional numerical robustness since they discretely conserve mass, momentum, and kinetic energy.

2.6.1 Interface Transport

The NGA code employs two interface transport techniques, the first of which is called Spectrally Refined Interface, SRI. The SRI method achieves local refinement in the form of quadrature points in each grid cell that contains the phase-interface, so that the level set function can be reconstructed using high order polynomials–thereby providing spectral accuracy [43]. Consequently, the local numerical errors in interface transport are reduced by the combined effect of increased resolution and increased order of accuracy. To render this method computationally efficient the transport of the level set function is performed using a semi-Lagrangian technique, removing all constraints on the time step size. Increased spatial resolution is achieved without noticeably reducing the time step size for level set transport, which is a unique feature of this method. Level set based methods usually show good accuracy, but suffer from poor mass conservation properties. By increasing the local resolution of the level set function, this new approach reduces numerical errors, thereby limiting mass conservation errors [43, 47, 46].

The SRI method was recently improved by introducing several key modifications. First, the number of quadrature points is allowed to vary from cell to cell, enabling the sub-cell resolution to be adapted to the interface topology. Two strategies for adaptive refinement

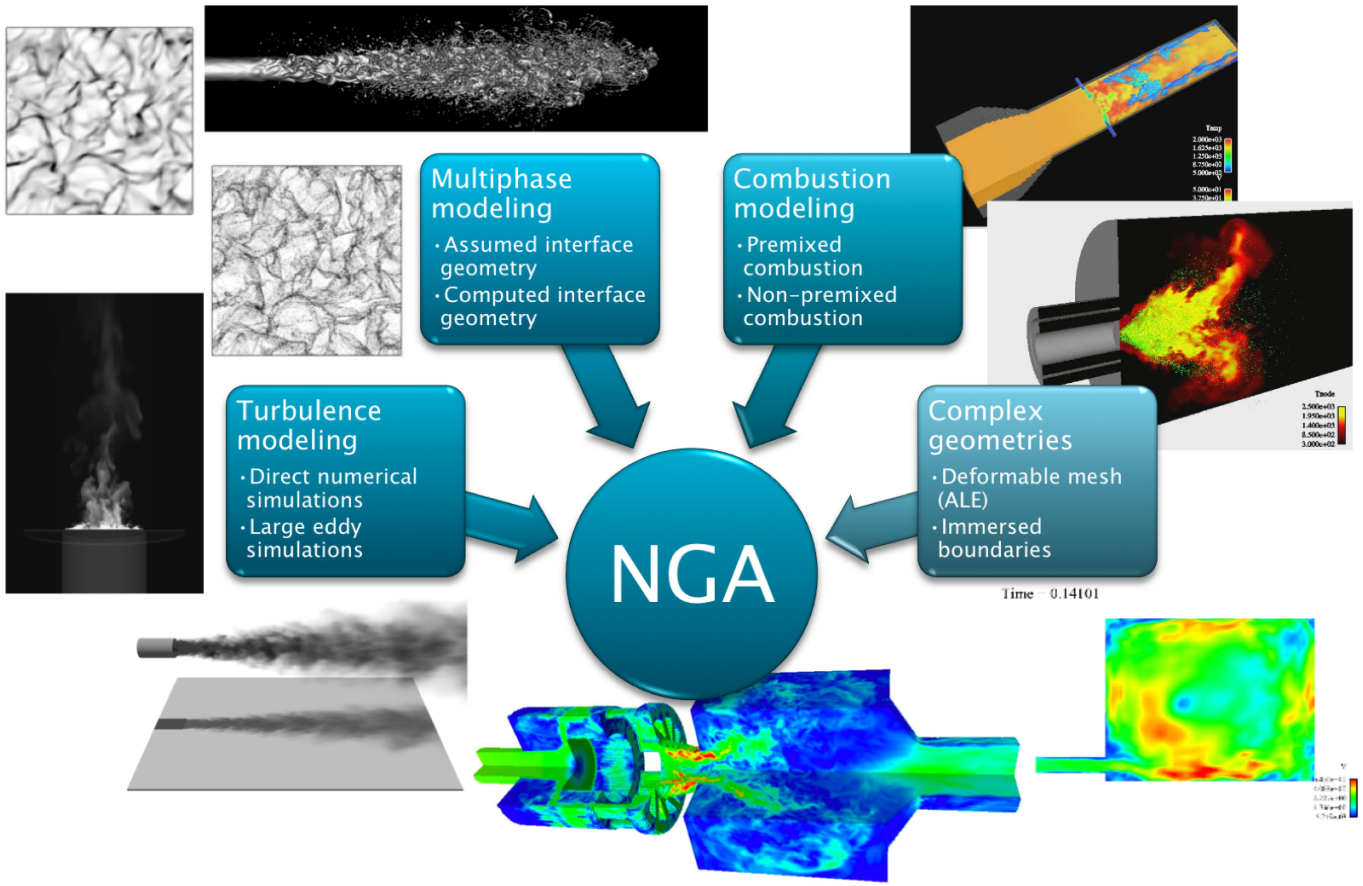

Figure 2.1: NGA–an integrated computational tool [48]

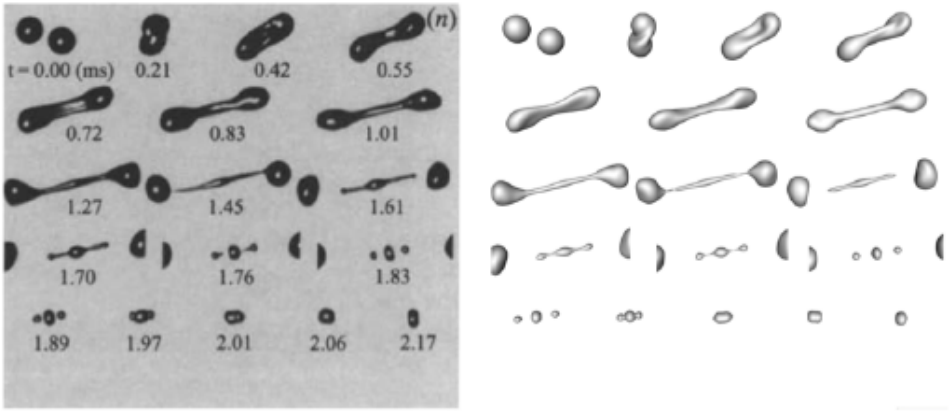

Figure 2.2: Droplet collision experiments (left) [100] and simulation with 20 cells per diameter using ASRI in NGA (right)

have been implemented: refinement based on the distance from the phase-interface, and refinement based on the local front curvature. The curvature is computed from the sub-cell quadrature data, allowing to achieve up to third order convergence, which was found to virtually eliminate spurious currents. The adaptive scheme is easier to implement, and is shown to be more accurate and computationally efficient than the original SRI approach. For a range of Reynolds and Weber numbers, ASRI was found to give very accurate results, even with a limited resolution (20 cells per diameter), as shown in Fig 2.2. Because of its excellent accuracy for interface description and transport, the ASRI strategy constitutes a method of choice for highly detailed numerical simulations of turbulent breakup [43, 47, 46].

A second interface transport technique, known as Accurate Conservative Levels Set, ACLS, combines an improved version of the conservative level set technique introduced in Olsson *et al.* [133] with a ghost fluid approach [52]. By employing a hyperbolic tangent level set function that is transported and re-initialized using fully conservative numerical schemes, mass conservation issues that are known to affect level set methods are greatly reduced. In order to improve the accuracy of the conservative level set method, high order numerical schemes are used. The overall robustness of the numerical approach is increased

by computing the interface normals from a signed distance function reconstructed from the hyperbolic tangent level set by a fast marching method [42]. The convergence of the curvature calculation is ensured by using a least squares reconstruction. The ghost fluid technique provides a way of handling the interfacial forces and large density jumps associated with two-phase flows with good accuracy, while avoiding artificial spreading of the interface. Since the proposed approach relies on partial differential equations, its implementation is straightforward in all coordinate systems, and it benefits from high parallel efficiency. The robustness and efficiency of the approach is further improved by using implicit schemes for the interface transport and re-initialization equations, as well as for the momentum solver. In this work, the ACLS method is used for simulations of atomizing liquid jets to leverage its good mass conservation qualities with the accompanying severe interface topology changes. For all other numerical results, the SRI method is used.

2.6.2 Time integration

The NGA code employs an iterative temporal advancement scheme with staggering in time between the velocity field and the scalar and density fields. For multiphase flow simulations, the level set field is advanced from $t^{n-1/2}$ to $t^{n+1/2}$ using the velocity at t^n. A semi-implicit Crank-Nicholson scheme is used, based on the time-advancement scheme of Pierce and Moin [140]. The velocity field is advanced from t^n to t^{n+1}, and the level set data is used at $t^{n+1/2}$ to solve the variable-coefficient Poisson equation for pressure and the electric potential.

2.6.3 Solving the Pressure and Electric Potential Poisson Equations

The equations for the pressure and the electric potential are Poisson equations with discontinuous coefficients. Solving these equations consumes a considerable quantity of computational time. With this challenge in mind, it is clear that an efficient and robust Poisson solver is essential to the performance of an incompressible CFD code. It is typical for the

Poisson solver to account for 60% or more of the time spent per time step. Incorporating electrostatic effects adds an additional variable coefficient Poisson equation, thereby increasing the cost of an already expensive simulation. A recent study evaluated several solvers, including Krylov-based solvers such as preconditioned conjugate gradient, deflated conjugate gradient, and multigrid solvers such as algebraic, geometric, and matrix-based multigrid for problems similar to multiphase flows [105]. The study concluded that the black-box multigrid (BBMG) solver of Dendy [37] is the most robust and efficient method. Based on this evaluation, the choice was made to implement a BBMG solver in NGA. The implementation follows the three-dimensional description introduced in Dendy [37]. The BBMG was introduced as a preconditioner to a conjugate gradient solver. The full solver, referred to henceforth as PCG-BBMG, is ideally suited for efficiently solving the pressure and electric potential Poisson equations. The PCG-BBMG solver was employed for all test cases and multiphase simulations reported in this work.

2.6.4 Summarized solution procedure

The solution methodology follows [48]:

- Advance the interface implicitly from $t^{n-1/2}$ to $t^{n+1/2}$ using the velocity at t^n.
- Advance the velocity field implicitly from t^n to t^{n+1} by the incompressible Navier-Stokes equations, Eq. (2.2) without the pressure term and without the electrostatic force density, $\mathbf{f}_e$.
- Project the velocty field by solving the pressure and electric potential Poisson equations using the GFM.
- Correct the velocity at t^{n+1} using the pressure gradient and electrostatic force density.

2.7 Research Objectives

Three-dimensional modeling of EHD for fuel injection applications is a complex problem. In a general sense, there are three relevant, contiguous regions in which the multiphase problem may be explored: the injecting nozzle, a region encompassing primary atomization, and one comprising secondary atomization. Figure 2.3 depicts a schematic of these regions. The region of primary atomization, downstream of a charge injecting nozzle, is considered in this work with the following research objectives:

- Develop a robust and accurate technique for modeling three-dimensional EHD atomization in dielectric liquids such as hydrocarbon fuels. This will require the coupling of multiphase methods for liquid atomization with the dynamics of self-precipitating electric fields and / or externally applied electric fields. The research proposed here is fundamental; it will focus on the dynamics of primary atomization and it will establish a point of departure for larger simulations.

- Conduct detailed numerical study of EHD atomization for liquid hydrocarbon fuels, such as kerosene. Large-scale, high fidelity DNS of electrically charged jets will yield an improved understanding of interactions among geometry, fluid and electrical properties, and EHD to inform experiment and guide design of fuel-injection devices for a range of combustion applications.

- Develop a DNS database for follow-on work in this project and future work within the engineering community.

- Appraise existing and propose new reduced order models (including LES models) for drop size and spray characteristics for EHD flows.

While only the domain of primary atomization will be considered in this work, the upstream and downstream regions represent topics of study that will improve the engineering commu-

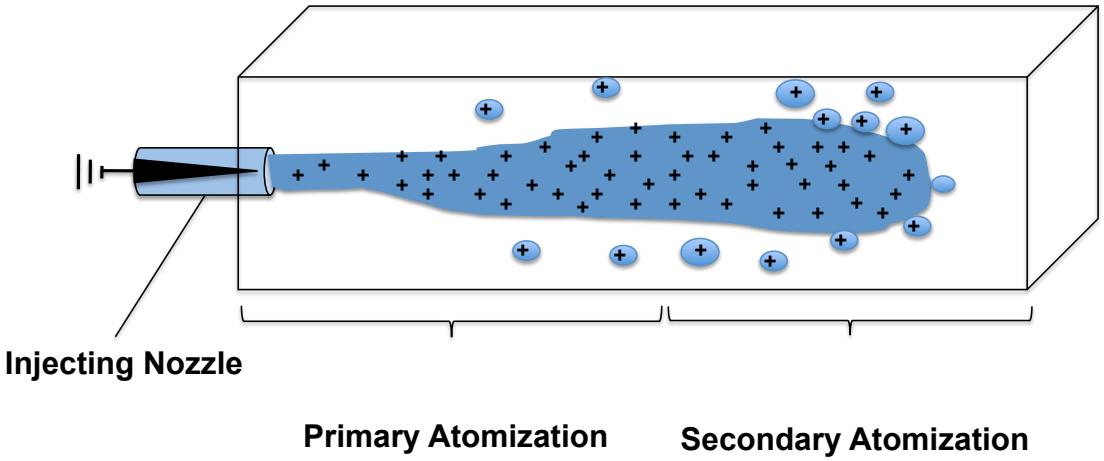

Figure 2.3: Schematic of a full charge injection system, highlighting distinct regions of study.

nity's understanding of EHD atomization and therefore contribute to advancing the state of the art. With the future in mind, an additional objective is therefore proposed:

- Establish a reference point for follow-on work, such as:
  - Secondary atomization modeling, which may incorporate evaporation models, Lagrangian particle tracking (LPT), and possibly "relaxed" surface charge on droplets;
  - Modeling different electro-physical classifications of liquids, inparticular ionic or polar liquids with much higher electrical conductivities, for the propulsion or spraying applications
  - Simulating the complex electrohydrodynamic flows within a charge injecting nozzle, incorporating diffusion effects as well as modeling the electrochemical processes that introduce electric charge in the dielectric liquid

Perspectives on this final objective are developed in §5.1-5.4 in Chapter 5.

Chapter 3

A Ghost Fluid, Level Set Approach for Simulating Electrohydrodynamic Atomization of Liquid Fuels

3.1 Overview

Electrohydrodynamics may provide a viable means to enhance atomization. EHD is an interdisciplinary topic that describes the complex interaction between fluid mechanics and electric fields. EHD may enable improved spray control and finer atomization so that fuel injection schemes can be inexpensively developed for the small combustion engine class. Moreover, EHD may provide efficient enhancements to hydrocarbon fuel atomization that could benefit a much broader range of engines and even other, non-combustion applications. An application of immediate interest is that of fuel injection for small interal combustion engines, with an approximate volumetric displacement of 200 cm^3 and smaller. A technique for leveraging the electric stresses to provide enhanced atomization that has shown experimental promise is that of "charge injection." Shrimpton and co-workers have studied the technique of charge injection through experimental [153, 154, 169, 170, 171, 204] and numerical [166, 168] investigations. A conceptual sketch of the technique is depicted in Fig 3.1. The mechanism for injecting electric charge includes a metallic emitting electrode, usually a sharp-tipped needle that generates a very high local electric field at the tip [84, 88, 97, 170, 171, 172, 204]. The dynamics of the electric field and the space charge are characterized by complex interactions and EHD-generated turbulence [90, 165, 167].

The amount of space charge that can be injected into a dielectric liquid is limited by

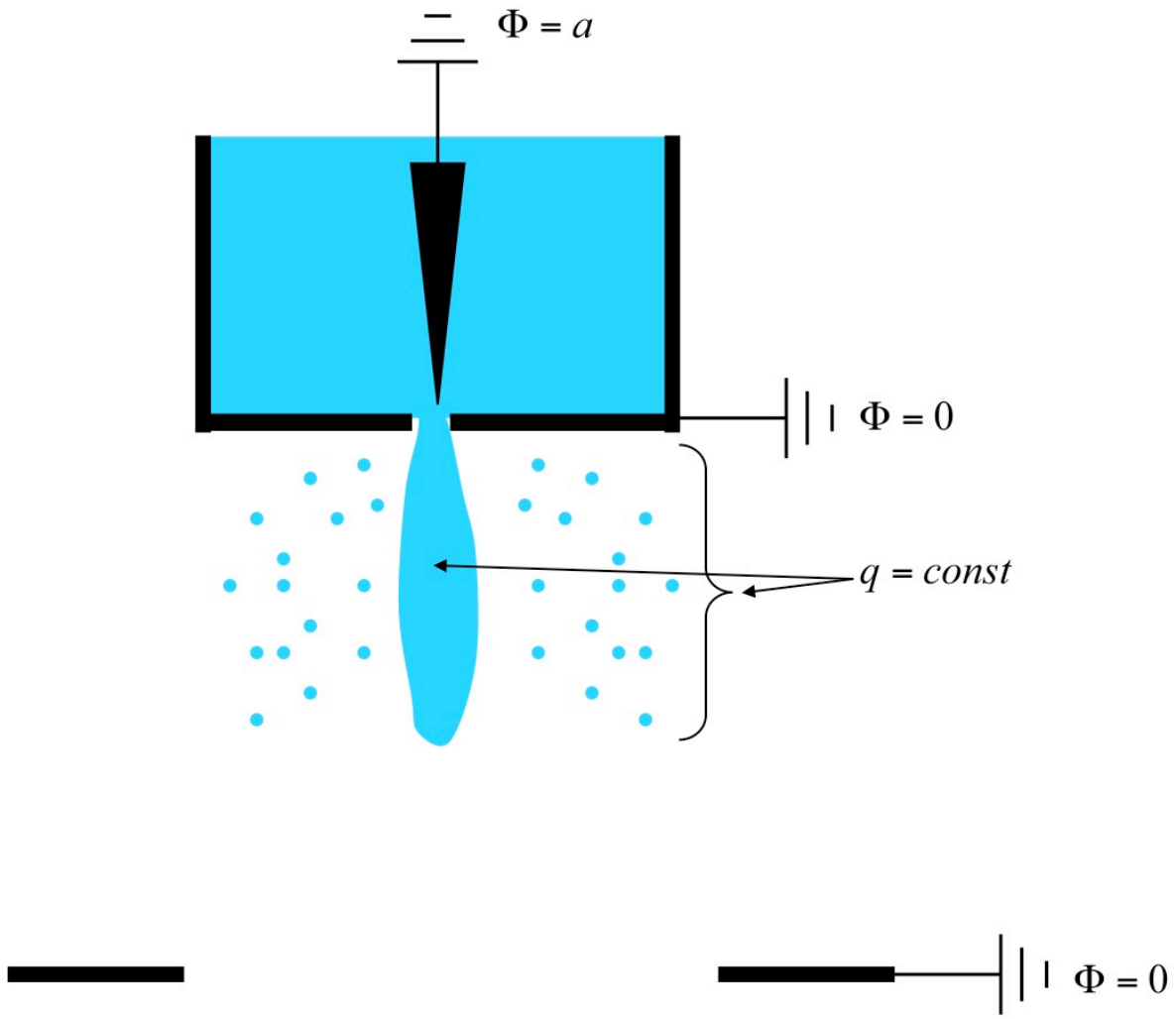

Figure 3.1: Concept sketch of unipolar, direct charge injection for electrohydrodynamic atomization

corona discharge, an ionization of the liquid that has been observed in many experiments [85, 88, 97, 170, 171, 166, 172]. Numerical results will diverge from physics if volumetric charge exceeds practical values [170, 204]. Values of space charge injected into dielectric liquid hydrocarbon fuels have been reported as high as 4 - 5 C/m^3 [97, 166], and the work proposed here will use this range as a reasonable upper limit for space charge density.

Recent numerical work by Tomar and co-workers [186] implemented a weighted harmonic mean (WHM) interpolation scheme to smoothen the electric properties at the interface, a coupled level set and volume-of-fluid (CLSVOF) algorithm for tracking the phase interface, and the continuum surface force (CSF) method for the electric surface forces. The work did not stipulate any immediate applications or flow classifications for which the model may be employed or uniquely suited, and the numerical methods employed in this work required a large number of grid points to achieve reasonable accuracy for simple canonical test cases [186]. Most recently, Guildenbecher, in his PhD thesis, reported no observed effects of electric charge on *secondary atomization* for either dielectric or conducting drops. He recommended DNS to fully elucidate the role of electrostatics in *primary atomization* and subsequently employ DNS results to develop predictive models for EHD atomization [69].

Considering the challenges and expense of experiments, high-fidelity numerical simulations should be able to provide some assistance in answering questions about the fundamentals and dynamics of EHD atomization. Its scientific promise nothwithstanding, numerical simulations of realistic liquid break-up are quite challenging due to the computational expense involved. This necessitates the use of large parallel computational resources. The long-term goals of this research effort are to understand the dynamics of EHD atomization, simulate classic experiments such as the shadowgraph in Fig. 3.2, and to pave the way for robust modeling of EHD sprays using advanced numerical methods.

This chapter presents the development of a sharp numerical scheme for EHD atomization. The regime of high electric Reynolds number, $Re_e \gg 1$, serves as the focus of the proposed numerical schemes. A ghost fluid method (GFM) approach is employed to solve

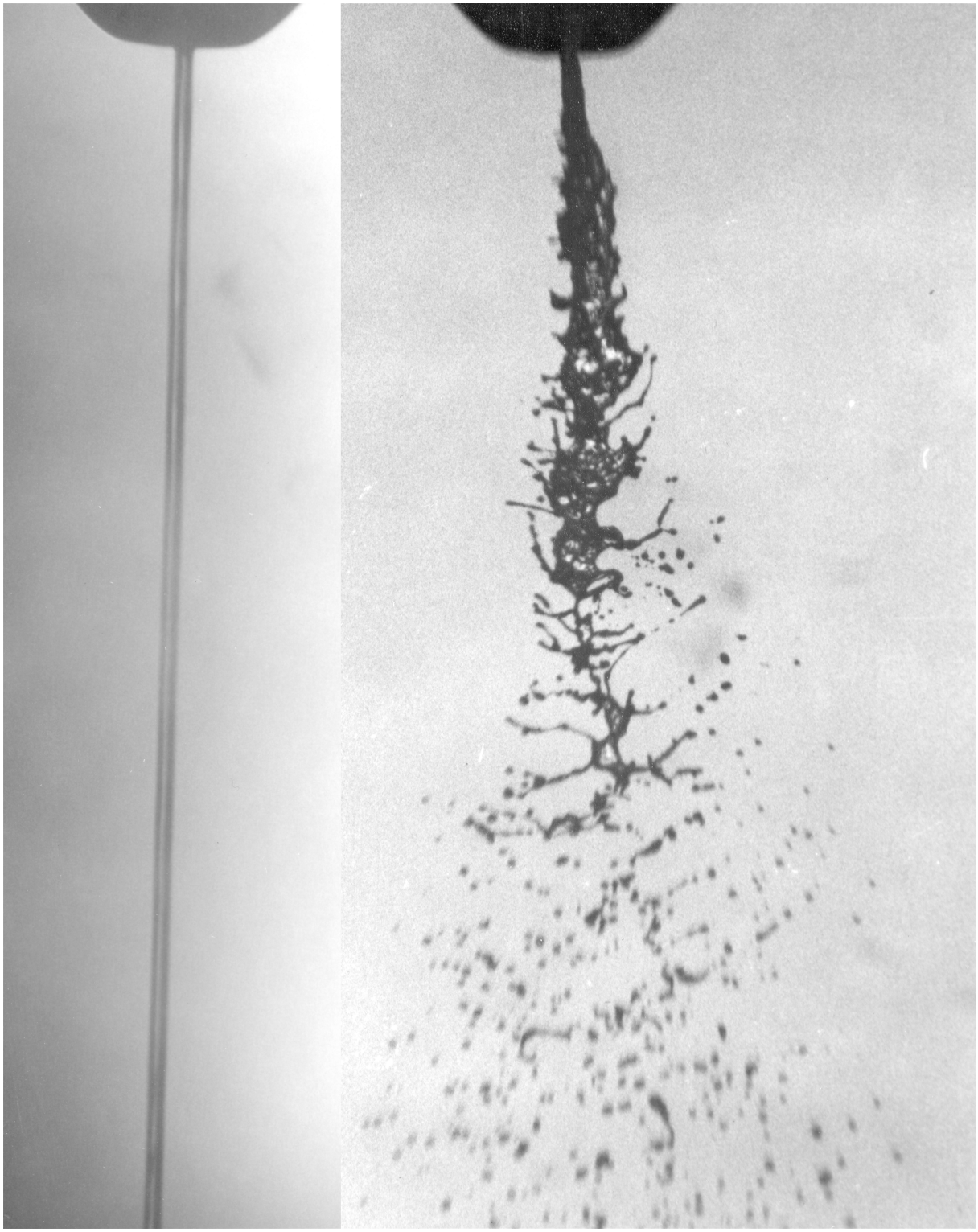

Figure 3.2: Comparison of uncharged (left) and charged (right, 0.5 C/m^3) kerosene jets [166]

for the electric potential Poisson equation in a sharp, accurate and robust manner. EHD boundary and jump conditions are implemented using a similar methodology, and subsequently used to solve the pressure Poisson equation. Electric charge is modeled in the bulk, with an initial assumption of no surface charge. The methods detailed here are implemented within the NGA code, which employs state-of-the-art interface tracking technique coupled to a robust and accurate Navier-Stokes/Ghost fluid solver. Test cases with exact or approximate analytical solutions are used to assess the robustness and accuracy of the EHD modules within NGA.

3.2 Modeling Strategy for High Electric Reynolds Number

Rigorous modeling of the governing equations and interface boundary conditions presents many challenges, one of which is the accumulation of bulk volumetric charge as a surface charge in a thin electric boundary layer much smaller than the hydrodynamic boundary layer. Furthermore, the surface charge interface boundary condition, Eq. (2.24), is difficult to implement and its complexity is compounded by time-varying accumulation of surface charge. Considering these challenges, it seems logical to model the electric charge as either a bulk or a surface charge.

The classic leaky dielectric model, first proposed by Taylor [183] and subsequently summarized in [110, 159], is frequently used to describe the effects of electric charge in dielectric liquids. The model contends that no real dielectric is perfect, and conduction processes cannot be completely ignored. One fundamental assumption of this model is that electric charge, however introduced into a dielectric liquid, has sufficient time to fully relax from a bulk volumetric charge to a surface charge. In low-inertia systems dominated by viscosity, surface tension or both, this assumption is relevant. For inertial flows, however, the advection time scale is often the governing time scale, which in some cases can be much shorter than the space charge relaxation time scale. For a situation of unipolar space charge injected into a dielectric liquid, charge relaxation will occur as the result of mutual

repulsion of like charges rather than through pure conduction processes [21]. The space charge relaxation time, τ_{sc}, represents the typical time for volumetric charge, q, to decay [33, 90], and the advection time scale, τ_f, is a characteristic time for a fluid element to move a distance defined by a relevant length scale, l_o. The two time scales are described by

$$\tau_{sc} = \frac{\epsilon}{\mu_i q}, \tag{3.1}$$

$$\tau_f = \frac{l_o}{u}. \tag{3.2}$$

The electric Reynolds number, Re_e, is defined here as the ratio of charge relaxation and advection times,

$$\mathrm{Re}_e = \frac{\tau_{sc}}{\tau_f}. \tag{3.3}$$

For illustration, consider a liquid dielectric hydrocarbon fuel into which unipolar electric charge is injected via field emission or field ionization processes. Numerous experiments have been conducted using this "charge injection" technique, most notably those performed by Lehr and Hiller [97] and Yule, Shrimpton and co-workers [170, 171, 172, 204]. Using properties for liquid kerosene and experimental parameters provided in [170] for nozzle diameter, $d_o = 500$ μm, injection charge, $q = 0.5$ C/m^3, Reynolds number, Re = 1900, and electric permittivity, $\epsilon = \kappa_e \epsilon_o = 1.95\text{e-}11$ F/m, a time scale comparison using $l_o = d_o$ yields

$$\begin{aligned} \tau_{sc} &\approx 0.039 \text{ s}, \\ \tau_f &\approx 0.00005 \text{ s}, \\ \mathrm{Re}_e &\approx 780, \end{aligned}$$

where typical values of ion mobility, $\mu_i = 1\text{e-}9$ m^2/V·s, dielectric constant, $\kappa_e = 2.2$, and vacuum permittivity, $\epsilon_o = 8.854\text{e-}12$ F/m, are used. More reasonably, the advection length scale should represent a domain of sufficient extent to capture relevant physical phenomena. For an advection length scale equal to twenty diameters ($20 d_o$), the electric Reynolds number is approximately 39. This suggests that the electric regime does not belong to a distinctly

high or low Re_e classification, and the corresponding dynamics likely include convection of bulk charge as well as charge relaxation through ionic drift. Nevertheless, the time scales do not support an assumption of fully relaxed charge. Indeed, the more reasonable approximation for electric behavior in this range, $10 < \mathrm{Re_e} < 400$, is one in which the charge is "bound" and moves with the fluid velocity. In this chapter, we assume constant volumetric charge and use this assumption as the foundation for the model described in the remainder of this section.

The assumption of constant volumetric space charge implies negligible surface charge. This assumption, along with incompressibility and material homogeneity within a phase, permit some simplifications of the governing equations and interface boundary conditions. Considering the electric body force, $\boldsymbol{f}_e$, given in Eq. (2.5), the electrostriction term can be neglected [21, 90]. The dielectric force appears in the pressure jump in Eq. (2.21), and subsequently the force density, Eq. (2.5), reduces to the Coulomb force in the bulk

$$\boldsymbol{f}_e = q\boldsymbol{E}. \tag{3.4}$$

Constant volumetric charge reduces the charge conservation equation to a solenoidal current density, described by

$$\nabla \cdot \boldsymbol{J} = 0, \tag{3.5}$$

and also eliminates the diffusion term in the current density, Eq. (2.11). For inertial flows of dielectric liquids, the ionic mobility term in Eq. (2.11) can be neglected for electric field strengths less than 10^7 V/m, and therefore the current density can be described as charge convecting with the fluid velocity,

$$\boldsymbol{J} = q\boldsymbol{u}. \tag{3.6}$$

Negligible surface charge implies that the normal component of the electric displacement vector is continuous. However, the jump in electric permittivity across the phase interface imposes a discontinuity in the normal component of the electric field, and Eq. (2.17) becomes

$$\boldsymbol{n} \cdot [\boldsymbol{D}]_\Gamma = \boldsymbol{n} \cdot [\epsilon \boldsymbol{E}]_\Gamma = [\epsilon E_n]_\Gamma = 0. \tag{3.7}$$

With negligible surface charge, constant permittivity within each phase, and negligible electrostriction, the jump in the tangential electric stress is zero, and hence Eq. (2.23) reduces to

$$\left[\boldsymbol{n}^{\mathsf{T}} \cdot (\boldsymbol{\sigma}^{f}) \cdot \boldsymbol{t}_{i}\right]_{\Gamma} = 0. \tag{3.8}$$

In the proceeding sections, we implement this model, employing the ghost fluid method to solve the electric potential Poisson equation and to develop a numerically sharp technique for computing the EHD pressure jump.

3.3 Ghost Fluid Method Implementation for Electric Potential Poisson Equation

Different strategies have been developed to handle the large density ratio and the surface tension force in a flow solver. The continuum surface force approach (CSF) [15] spreads out both the density jump and the surface tension force over a few cells surrounding the interface in order to facilitate the numerical discretization. Consequently, this approach tends to misrepresent the smallest front structures. In the context of finite differences, the ghost fluid method (GFM) [52] provides a very attractive way of handling discontinuities by using generalized Taylor series expansions that directly include these discontinuities. Because GFM explicitly deals with the density jump, the resulting discretization is not affected by the density ratio. Similarly, the surface tension force can be included directly in the form of a pressure jump, providing an adequate sharp numerical treatment of this singular term. As detailed in the following sections, the GFM is used for the electric potential Poisson equation and also for a sharp implementation of the EHD jump conditions.

An initial step in implementing an EHD module is to solve for the electric potential, ϕ, which is an additional variable coefficient Poisson equation given in Eq. (2.8). In previous work, a generalized Taylor series expansion was employed to provide a sharp implementation for the pressure Laplacian across an interface jump [38, 42, 48]. Using a similar approach, a sharp formulation is presented for the gradient and Laplacian of the electric potential, in

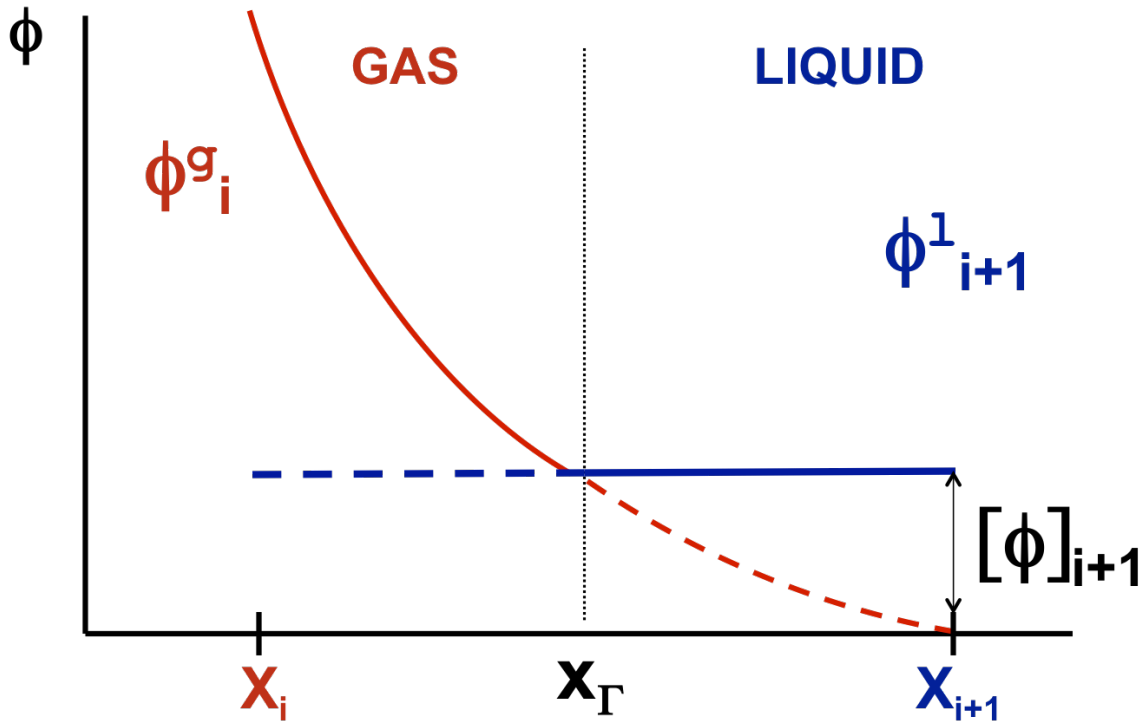

Figure 3.3: Illustration of Ghost Fluid Method for a variable, such as the electric potential, ϕ, which displays a discontinuity at x_Γ. Dashed lines depict Taylor series expansions across the interface [48].

either the gas or the liquid phase.

Using the simplification of no surface charge from Eq. (3.7), a convenient expression for the jump in the normal component of the electric field can be derived using an algebraic extension of the methodology set forth in Appendix A as

$$[\epsilon E_n]_\Gamma = [\epsilon]_\Gamma E_n^g + \epsilon_l [E_n]_\Gamma = 0. \tag{3.9}$$

Hence,

$$[E_n]_\Gamma = \frac{-[\epsilon]_\Gamma}{\epsilon_l} E_n^g = \frac{(\epsilon_g - \epsilon_l)}{\epsilon_l} E_n^g = (1/\epsilon_r - 1) E_n^g, \tag{3.10}$$

or equivalently,

$$[E_n]_\Gamma = \frac{-[\epsilon]_\Gamma}{\epsilon_g} E_n^l = \frac{(\epsilon_g - \epsilon_l)}{\epsilon_g} E_n^l = (1 - \epsilon_r) E_n^l, \tag{3.11}$$

where ϵ_r is the ratio of electric permittivities. In addition, we still have continuous tangential electric field components,

$$[E_{t_1}]_\Gamma = 0 \quad \text{and} \quad [E_{t_2}]_\Gamma = 0.$$

The jump in the electric displacement vector can be written as the product of the scalar permittivity and the electric field vector, $[\boldsymbol{D}]_\Gamma = [\epsilon \boldsymbol{E}]_\Gamma$, assuming electrically linear behavior. Re-arranging the jump algebraically, we can describe the product of permittivity and the electric field vector as

$$[\epsilon \boldsymbol{E}]_\Gamma = \epsilon_l [\boldsymbol{E}]_\Gamma + \boldsymbol{E}^g [\epsilon]_\Gamma, \tag{3.12}$$

and with the continuous tangential components, the first term on the right-hand side reduces, yielding

$$[\epsilon \boldsymbol{E}]_\Gamma = \epsilon_l [E_n] \boldsymbol{n} + [\epsilon]_\Gamma \boldsymbol{E}^g. \tag{3.13}$$

Expressing the jump in vector form for its Cartesian dimensions gives

$$\begin{aligned} [\epsilon \boldsymbol{E}]_\Gamma &= [\epsilon (E_x \boldsymbol{e}_x + E_y \boldsymbol{e}_y + E_z \boldsymbol{e}_z)]_\Gamma, \\ &= [\epsilon E_x]_\Gamma \boldsymbol{e}_x + [\epsilon E_y]_\Gamma \boldsymbol{e}_y + [\epsilon E_z]_\Gamma \boldsymbol{e}_z. \end{aligned} \tag{3.14}$$

The Cartesian components can be expressed as

$$[\epsilon E_x]_\Gamma = [\epsilon \boldsymbol{E} \cdot \boldsymbol{e}_x]_\Gamma = [\epsilon \boldsymbol{E}]_\Gamma \cdot \boldsymbol{e}_x, \tag{3.15}$$

$$[\epsilon E_y]_\Gamma = [\epsilon \boldsymbol{E} \cdot \boldsymbol{e}_y]_\Gamma = [\epsilon \boldsymbol{E}]_\Gamma \cdot \boldsymbol{e}_y, \tag{3.16}$$

$$[\epsilon E_z]_\Gamma = [\epsilon \boldsymbol{E} \cdot \boldsymbol{e}_z]_\Gamma = [\epsilon \boldsymbol{E}]_\Gamma \cdot \boldsymbol{e}_z. \tag{3.17}$$

Substituting Eq. (3.13) yields,

$$[\epsilon E_x]_\Gamma = \epsilon_l [E_n](\boldsymbol{n} \cdot \boldsymbol{e}_x) + [\epsilon]_\Gamma E_x^g, \tag{3.18}$$

$$[\epsilon E_y]_\Gamma = \epsilon_l [E_n](\boldsymbol{n} \cdot \boldsymbol{e}_y) + [\epsilon]_\Gamma E_y^g, \tag{3.19}$$

$$[\epsilon E_z]_\Gamma = \epsilon_l [E_n](\boldsymbol{n} \cdot \boldsymbol{e}_z) + [\epsilon]_\Gamma E_z^g, \tag{3.20}$$

and substituting Eq. (3.10) yields the following for each Cartesian component,

$$[\epsilon E_x]_\Gamma = [\epsilon]_\Gamma (E_x^g - E_n^g n_x), \tag{3.21}$$

$$[\epsilon E_y]_\Gamma = [\epsilon]_\Gamma (E_y^g - E_n^g n_y), \tag{3.22}$$

$$[\epsilon E_z]_\Gamma = [\epsilon]_\Gamma (E_z^g - E_n^g n_z), \tag{3.23}$$

where $n_x = \boldsymbol{n} \cdot \boldsymbol{e}_x$, $n_y = \boldsymbol{n} \cdot \boldsymbol{e}_y$, and $n_z = \boldsymbol{n} \cdot \boldsymbol{e}_z$, represent the Cartesian components of the interface normal vector.

Equations (3.21-3.23) are challenging to implement within a staggered mesh numerical scheme. The electric potential, ϕ, level set, G, and interface normals are known at the cell centers, while vector quantities are computed at the faces. Direct computation of the normal electric field component, E_n, would require a very large stencil, thereby greatly increasing the cost of solving the electric potential Poisson equation.

Following the methodology proposed by Liu *et al.* [102], we employ a simplification that enables an efficient, dimension-by-dimension application of the jump, described by

$$[\epsilon \boldsymbol{E}]_\Gamma \approx [\epsilon E_n]_\Gamma \boldsymbol{n}. \tag{3.24}$$

As suggested by Liu *et al.* [102], this assumption accurately and efficiently captures the jump in the normal component, but leads to the generally false identity $[\epsilon E_{t_i}]_\Gamma = 0$. However, we know $[\epsilon E_{t_i}]_\Gamma = [\epsilon]_\Gamma E_{t_i}$ since $[E_{t_i}]_\Gamma = 0$. For cases of interest in this work, the normal component of the electric field vector is expected to be significantly larger than its tangential component, and therefore the error in the tangential jump is likely to remain small. The simplification described by Eq. (3.24) is employed only for the electric potential in order to enable an efficient solution for this variable coefficient Poisson equation.

The Cartesian components of the jump were specified in Eq. (3.14). Assuming the components are uniquely zero and following the methodology in Eqs. (3.9-3.11) yields,

$$[E_x]_\Gamma = \frac{-[\epsilon]_\Gamma}{\epsilon_l} E_x^g = \frac{(\epsilon_g - \epsilon_l)}{\epsilon_l} E_x^g = (1/\epsilon_r - 1) E_x^g, \tag{3.25}$$

$$[E_x]_\Gamma = \frac{-[\epsilon]_\Gamma}{\epsilon_g} E_x^l = \frac{(\epsilon_g - \epsilon_l)}{\epsilon_g} E_x^l = (1 - \epsilon_r) E_x^l. \tag{3.26}$$

Summarizing for all three dimensions,

$$[E_x]_\Gamma \approx (1/\epsilon_r - 1) E_x^g = (1 - \epsilon_r) E_x^l, \tag{3.27}$$

$$[E_y]_\Gamma \approx (1/\epsilon_r - 1) E_y^g = (1 - \epsilon_r) E_y^l, \tag{3.28}$$

$$[E_z]_\Gamma \approx (1/\epsilon_r - 1) E_z^g = (1 - \epsilon_r) E_z^l. \tag{3.29}$$

Equations (3.27-3.29) represent an efficient set of dimension-by-dimension interface jumps. To discretize these equations, consider a Taylor series expansion of ϕ at stencil points x_i and

x_{i+1}, as

$$[\phi]_i = [\phi]_\Gamma + (x_i - x_\Gamma)[\nabla\phi]_\Gamma + O((x_i - x_\Gamma)^2), \tag{3.30}$$

$$[\phi]_{i+1} = [\phi]_\Gamma + (x_{i+1} - x_\Gamma)[\nabla\phi]_\Gamma + O((x_{i+1} - x_\Gamma)^2). \tag{3.31}$$

The electric potential is continuous at the interface, guaranteed by Eq. (2.20). We employ the jump in the gradient, $[\nabla\phi]_\Gamma$, to provide a sharp representation for the jump in ϕ between neighboring stencil points,

$$[\phi]_i \approx (x_i - x_\Gamma)[\nabla\phi]_\Gamma, \tag{3.32}$$

$$[\phi]_{i+1} \approx (x_{i+1} - x_\Gamma)[\nabla\phi]_\Gamma. \tag{3.33}$$

Note, the jump in the electric potential gradient is equivalent to the jump in the electric field vector, $[\nabla\phi]_\Gamma = -[\boldsymbol{E}]_\Gamma$. Applying the Cartesian dimension jump in Eqs. (3.27-3.29) yields

$$[\nabla_x\phi]_\Gamma = -[E_x]_\Gamma = \frac{-[\epsilon]_\Gamma E_x^g|_\Gamma}{\epsilon_l}, \tag{3.34}$$

where,

$$E_x^g|_\Gamma \approx E_x^g|_{i+1/2} = \frac{\phi_{i+1}^g - \phi_i^g}{\Delta x} = \frac{\phi_{i+1}^l - \phi_i^g}{\Delta x} - \frac{[\phi]_{i+1}}{\Delta x}, \tag{3.35}$$

and therefore

$$[\phi]_{i+1} = -(x_{i+1} - x_\Gamma)\frac{[\epsilon]_\Gamma}{\epsilon_l}\left(\frac{\phi_{i+1}^l - \phi_i^g}{\Delta x} - \frac{[\phi]_{i+1}}{\Delta x}\right). \tag{3.36}$$

Defining a gas fraction index, $\theta = (x_\Gamma - x_i)/\Delta x$, and modified permittivity, $\epsilon^\star = \epsilon_l\theta + \epsilon_g(1-\theta)$, yields

$$[\phi]_{i+1} = \left(1 - \frac{\epsilon_l}{\epsilon^\star}\right)(\phi_{i+1}^l - \phi_i^g). \tag{3.37}$$

Employing the modified permittivity yields a discretized expression for the gradient of the

potential, given by

$$\begin{aligned}\epsilon_g \frac{\partial \phi}{\partial x}\bigg|^g_{i+1/2} &= \epsilon_g \left(\frac{\phi^l_{i+1} - \phi^g_i}{\Delta x} - \frac{[\phi]_{i+1}}{\Delta x} \right) \\ &= \left(\frac{\phi^l_{i+1} - \phi^g_i}{\Delta x} - \left(1 - \frac{\epsilon_l}{\epsilon^\star}\right) \left(\frac{\phi^l_{i+1} - \phi^g_i}{\Delta x} \right) \right) \\ &= \frac{\epsilon_g \epsilon_l}{\epsilon^\star} \left(\frac{\phi^l_{i+1} - \phi^g_i}{\Delta x} \right). \end{aligned} \tag{3.38}$$

Simplifying provides a direct expression for the gradient of the electric potential in the gas,

$$\frac{\partial \phi}{\partial x}\bigg|^g_{i+1/2} = \frac{\epsilon_l}{\epsilon^\star} \left(\frac{\phi^l_{i+1} - \phi^g_i}{\Delta x} \right). \tag{3.39}$$

Recognizing that in the liquid, the gas fraction becomes $\theta = (x_{i+1} - x_\Gamma)/\Delta x$ provides a similar expression for the gradient in the liquid, described by

$$\frac{\partial \phi}{\partial x}\bigg|^l_{i+1/2} = \frac{\epsilon_g}{\epsilon^\star} \left(\frac{\phi^g_{i+1} - \phi^l_i}{\Delta x} \right). \tag{3.40}$$

Extending this methodology yields a discretization for the Laplacian of the electric potential, written in either the liquid or the gas phase as

$$\frac{\partial}{\partial x}\left(\epsilon_l \frac{\partial \phi}{\partial x} \right)\bigg|^l_{i+1/2} = \frac{\epsilon_l \epsilon_g}{\epsilon^\star} \left(\frac{\phi^g_{i+1} - \phi^l_i}{\Delta x^2} \right) - \epsilon_l \left(\frac{\phi^l_i - \phi^l_{i-1}}{\Delta x^2} \right), \tag{3.41}$$

$$\frac{\partial}{\partial x}\left(\epsilon_g \frac{\partial \phi}{\partial x} \right)\bigg|^g_{i+1/2} = \frac{\epsilon_l \epsilon_g}{\epsilon^\star} \left(\frac{\phi^l_{i+1} - \phi^g_i}{\Delta x^2} \right) - \epsilon_g \left(\frac{\phi^g_i - \phi^g_{i-1}}{\Delta x^2} \right). \tag{3.42}$$

Equations (3.39-3.42) are implemented within the EHD module of NGA to provide a robust, efficient and accurate solution for the electric potential.

3.4 Sharp Numerical Method for EHD Pressure Jump

A second step to developing an EHD module is to implement a sharp, numerically accurate scheme for the EHD interface jump conditions in Eq. (2.21). Even with perfect dielectrics, EHD effects can be noticed due to the strong coupling through the jump conditions at the interface. The right hand side of Eq. (2.21) shows how the electrostatics contribute

to the pressure jump across the interface through the normal and tangential components of the electric field. In this section, we derive a mathematical formulation for the pressure jump that includes the EHD stresses, and then use the GFM to develop an efficient numerical scheme to compute the normal and tangential electric field components at the phase interface.

Considering the right-hand side of Eq. (2.21), we expand the EHD contributions to the overall pressure jump. Employing algebraic manipulation similar to that in Section 3.3 yields

$$\left[\frac{1}{2}\epsilon E_n^2\right]_\Gamma = \epsilon_l [E_n]_\Gamma \left(E_n^l + E_n^g\right) + (E_n^g)^2 [\epsilon]_\Gamma. \tag{3.43}$$

Combining Eqs. (3.10) and (3.43) yields

$$\left[\frac{1}{2}\epsilon E_n^2\right]_\Gamma = -[\epsilon]_\Gamma (E_n^g E_n^l). \tag{3.44}$$

Recognizing that the jump in the square of the tangential component, $[E_{t_i}^2]_\Gamma$, is identically zero provides a convenient simplification for the jump in the tangential field terms. Superscripts g and l are omitted since they are irrelevant for the continuous tangential components, and therefore

$$\left[\epsilon E_{t_i}^2\right]_\Gamma \quad = \quad E_{t_i}^2 [\epsilon]_\Gamma. \tag{3.45}$$

Combining Eqs. (3.44-3.45) to form the right hand side of Eq. (2.21) yields

$$\left[\frac{1}{2}\epsilon E_n^2\right]_\Gamma - \left[\frac{1}{2}\epsilon E_{t_1}^2\right]_\Gamma - \left[\frac{1}{2}\epsilon E_{t_2}^2\right]_\Gamma = \frac{-[\epsilon]_\Gamma}{2}\left(E_n^g E_n^l + (E_{t_1})^2 + (E_{t_2})^2\right). \tag{3.46}$$

The quantity $E_n^g E_n^l$ is challenging to evaluate. This product can be re-cast in terms of either the gas or liquid side, as

$$E_n^g E_n^l = \begin{cases} (E_n^g)^2 \frac{1}{\epsilon_r} & \text{(gas side)}, \\ (E_n^l)^2 \epsilon_r & \text{(liquid side)}. \end{cases} \tag{3.47}$$

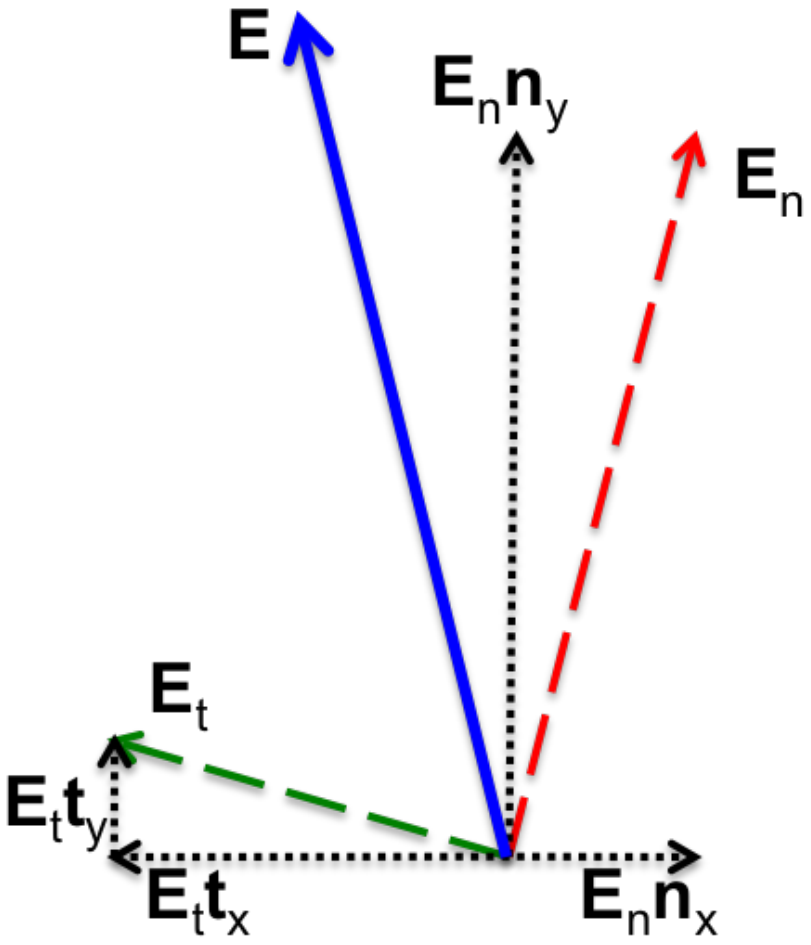

Figure 3.4: Components of the electric field vector

Combining Eqs. (3.46-3.47) and Eq. (2.21) yields a final form of the pressure jump, which accounts for EHD, viscous, and surface tension stresses,

$$[p]_\Gamma - 2[\mu]_\Gamma \boldsymbol{n}^\mathsf{T} \cdot \nabla \boldsymbol{u} \cdot \boldsymbol{n} - \gamma\kappa = \begin{cases} \frac{(\epsilon_g - \epsilon_l)}{2}\left((E_n^g)^2 \frac{1}{\epsilon_r} + (E_{t_1})^2 + (E_{t_2})^2\right) & \text{(gas)}, \\ \\ \frac{(\epsilon_g - \epsilon_l)}{2}\left((E_n^l)^2 \epsilon_r + (E_{t_1})^2 + (E_{t_2})^2\right) & \text{(liquid)}. \end{cases} \tag{3.48}$$

To implement the pressure jump, $[p]_\Gamma$, in Eq. (3.48), the normal and tangential components of the electric field are required. The interface normal vectors are known at the cell centers and the Cartesian components of the electric field are known at the cell faces, presenting a challenge for direct computation of the normal and tangential electric field components. Therefore, it is necessary to interpolate the Cartesian components of the electric field to the cell center across the phase interface, re-construct a cell-centered electric field vector, and subsequently partition the vector into normal and tangential components. The normal component of the electric field experiences a jump across the interface, and the GFM is employed to handle this discontinuity. The jump in the electric field can be written in vector form,

$$\begin{aligned} [\boldsymbol{E}]_\Gamma &= [(E_n \boldsymbol{n} + E_{t_1} \boldsymbol{t}_1 + E_{t_2} \boldsymbol{t}_2)]_\Gamma, \\ &= [E_n]_\Gamma \boldsymbol{n} + [E_{t_1}]_\Gamma \boldsymbol{t}_1 + [E_{t_2}]_\Gamma \boldsymbol{t}_2. \end{aligned} \tag{3.49}$$

Incorporating the continuous tangential electric field jump condition given in Eq. (2.19) simplifies Eq. (3.49) to

$$[\boldsymbol{E}]_\Gamma = [E_n]_\Gamma \boldsymbol{n}. \tag{3.50}$$

The Cartesian components of the jump can be derived,

$$[E_x]_\Gamma = [\boldsymbol{E}]_\Gamma \cdot \boldsymbol{e}_x = [E_n]_\Gamma \boldsymbol{n} \cdot \boldsymbol{e}_x = [E_n] n_x, \tag{3.51}$$

$$[E_y]_\Gamma = [E_n] n_y, \tag{3.52}$$

$$[E_z]_\Gamma = [E_n] n_z. \tag{3.53}$$

Combining with Eq. (3.10) and Eq. (3.11) gives

$$[E_x]_\Gamma = (1/\epsilon_r - 1) E_n^g n_x = (1 - \epsilon_r) E_n^l n_x, \tag{3.54}$$

$$[E_y]_\Gamma = (1/\epsilon_r - 1) E_n^g n_y = (1 - \epsilon_r) E_n^l n_y, \tag{3.55}$$

$$[E_z]_\Gamma = (1/\epsilon_r - 1) E_n^g n_z = (1 - \epsilon_r) E_n^l n_z. \tag{3.56}$$

Equations (3.54-3.56) are used to interpolate the electric field components to the cell center. For the stencil shown in Fig. 3.5, the interpolation scheme depends on whether the cell center is in the liquid or the gas phase. Since the electric field vector components are computed at the cell faces, it is also necessary to determine the phase at the cell faces. To determine whether the cell face is in the liquid or gas, the value of the level set function is interpolated to the cell face between neighboring cell centers.

Begining with general expressions for a cell center point in the liquid or the gas phase, a second-order accurate interpolation for the electric field with a first-order approximation

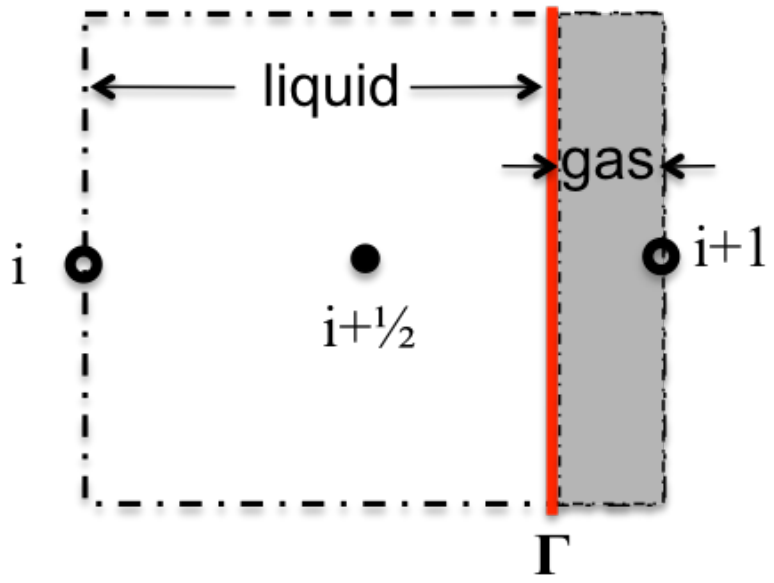

Figure 3.5: $x-$stencil showing interface location; gas fraction, θ, less than 50%.

for the jump can be written as

$$\begin{aligned} E^l_{x,i+1/2} &= \frac{E^l_{x,i} + E^l_{x,i+1}}{2} \\ &= \frac{E^l_{x,i} + E^g_{x,i+1}}{2} + \frac{[E_x]_\Gamma}{2}, \end{aligned} \tag{3.57}$$

$$\begin{aligned} E^g_{x,i+1/2} &= \frac{E^g_{x,i} + E^g_{x,i+1}}{2} \\ &= \frac{E^g_{x,i} + E^l_{x,i+1}}{2} - \frac{[E_x]_\Gamma}{2}. \end{aligned} \tag{3.58}$$

Since the interface normal is known at the cell center, we use the formulation in Eqs. (3.51-3.53) to accurately represent each Cartesian component of the jump. Combining with Eqs. (3.57-3.58) yields a dimension by dimension expression for the electric field jump at the cell center. Written only in the $x-$component for brevity, but in both the liquid and gas

phase, gives

$$[E_x]^l_{\Gamma,(i+1/2)} = \frac{-(\epsilon_l - \epsilon_g)}{\epsilon_g}(E_{x,i+1/2}n_x + E_{y,j+1/2}n_y + E_{z,k+1/2}n_z)^l n_x$$

$$= (1-\epsilon_r)(E_{x,i+1/2}n_x + E_{y,j+1/2}n_y + E_{z,k+1/2}n_z)^l n_x, \tag{3.59}$$

$$[E_x]^g_{\Gamma,(i+1/2)} = \frac{-(\epsilon_l - \epsilon_g)}{\epsilon_l}(E_{x,i+1/2}n_x + E_{y,j+1/2}n_y + E_{z,k+1/2}n_z)^g n_x$$

$$= \left(\frac{1}{\epsilon_r} - 1\right)(E_{x,i+1/2}n_x + E_{y,j+1/2}n_y + E_{z,k+1/2}n_z)^g n_x, \tag{3.60}$$

$$[E_y]_{\Gamma,(i+1/2)^l} = (1-\epsilon_r)(E_x n_x + E_y n_y + E_z n_z)^l n_y, \tag{3.61}$$

$$[E_y]_{\Gamma,(i+1/2)^g} = (1-1/\epsilon_r)(E_x n_x + E_y n_y + E_z n_z)^g n_y, \tag{3.62}$$

$$[E_z]_{\Gamma,(i+1/2)^l} = (1-\epsilon_r)(E_x n_x + E_y n_y + E_z n_z)^l n_z, \tag{3.63}$$

$$[E_z]_{\Gamma,(i+1/2)^g} = (1-1/\epsilon_r)(E_x n_x + E_y n_y + E_z n_z)^g n_z. \tag{3.64}$$

For simplicity, we introduce a coefficient, $C^{l,g}_{x,y,z}$, to represent the jump conditions for one or two jumps within a cell for each Cartesian dimension. With superscripts l and g representing

the liquid and gas phases at the cell center, respectively, the coefficient is described as

$$C^{l,g}_{x,y,z} = \begin{cases} 0 & \text{if no jump,} \\ (1-\epsilon_r) & \text{single jump, liquid at cell center,} \\ (1-1/\epsilon_r) & \text{single jump, gas at cell center,} \\ 2(1-\epsilon_r) & \text{double jump, liquid at cell center,} \\ 2(1-1/\epsilon_r) & \text{double jump, gas at cell center.} \end{cases} \tag{3.65}$$

Re-writing Eqs. (3.59) - (3.64), and accounting for the sign difference (+/-) of Eqs. (3.57) and (3.58)

yields

$$E^l_{x,i+1/2} = \frac{1}{2}\Bigg(E^l_{x,i} + E^g_{x,i+1} + C^l_x (E_{x,i+1/2} n_x + E_{y,j+1/2} n_y + E_{z,k+1/2} n_z)^l n_x \Bigg), \tag{3.66}$$

$$E^g_{x,i+1/2} = \frac{1}{2}\Bigg(E^l_{x,i} + E^g_{x,i+1} + C^g_x (E_{x,i+1/2} n_x + E_{y,j+1/2} n_y + E_{z,k+1/2} n_z)^g n_x \Bigg), \tag{3.67}$$

$$E^l_{y,j+1/2} = \frac{1}{2}\Bigg(E^l_{x,i} + E^g_{x,i+1} + C^l_y (E_{x,i+1/2} n_x + E_{y,j+1/2} n_y + E_{z,k+1/2} n_z)^l n_x \Bigg), \tag{3.68}$$

$$E^g_{y,j+1/2} = \frac{1}{2}\Bigg(E^l_{x,i} + E^g_{x,i+1} + C^g_y (E_{x,i+1/2} n_x + E_{y,j+1/2} n_y + E_{z,k+1/2} n_z)^g n_x \Bigg), \tag{3.69}$$

$$E^l_{z,k+1/2} = \frac{1}{2}\Bigg(E^l_{x,i} + E^g_{x,i+1} + C^l_z (E_{x,i+1/2} n_x + E_{y,j+1/2} n_y + E_{z,k+1/2} n_z)^l n_x \Bigg), \tag{3.70}$$

$$E^g_{z,k+1/2} = \frac{1}{2}\Bigg(E^l_{x,i} + E^g_{x,i+1} + C^g_z (E_{x,i+1/2} n_x + E_{y,j+1/2} n_y + E_{z,k+1/2} n_z)^g n_x \Bigg). \tag{3.71}$$

Equations (3.66-3.71) fully describe the electric field vector at the cell center, interpolated from the cell faces across an interface. This cell-centered electric field is partitioned into normal and tangential components, which are used to compute the right hand side of the pressure jump in Eq. (2.21) at the cell center. The pressure jump is linearly interpolated to the interface and then used to solve the pressure Poisson equation, which also employs the

GFM [42, 43].

3.5 Implementation of Coulomb Force

The Coulomb force, Eq. (3.4), is implemented as a face-centered source term in the Navier-Stokes equations. For each Cartesian dimension, charge is computed at each cell face using a height function of the liquid volume fraction according to Eq. (3.72), and then multiplied by the local face value of the electric field. The height function, $\lambda_{i+\frac{1}{2},j,k}$, is defined by

$$\lambda_{i+\frac{1}{2},j,k} = \begin{cases} 1 & \text{if } G_{i,j,k} \text{ and } G_{i+1,j,k} \geq 0, \\ 0 & \text{if } G_{i,j,k} \text{ and } G_{i+1,j,k} < 0, \\ \frac{G^+_{i,j,k}+G^+_{i+1,j,k}}{\left|G_{i,j,k}\right|+\left|G_{i+1,j,k}\right|} & \text{otherwise,} \end{cases} \tag{3.72}$$

where $G^+ = \max(G_{i,j,k}, 0)$.

3.6 Validation and Numerical Results

Several canonical test cases were employed to validate the numerical solutions for the electric field: a one-dimensional rectangle with a flat interface separating regions of two permittivities; a one-dimensional interface with constant charge density; a charged droplet in an applied electric field accelerating to terminal velocity; a dielectric drop in a uniform electric field; and a deforming dielectric spheroid stressed by an electric field. To assess the performance of the proposed approach and demonstrate its robustness, simulations of a charged and uncharged liquid kerosene jet in quiescent air are conducted and qualitatively compared.

All simulations performed in this work employ an in-house code named NGA, for which the numerical methods presented here have been implemented in parallel using Message Passing Interface (MPI). NGA extends the family of high order fully conservative finite difference schemes proposed by Morinishi and Vasilyev [115, 116, 189] to variable density

low-Mach number flows [38, 48]. These schemes, tailored for DNS and LES, provide both excellent accuracy and numerical robustness since they discretely conserve mass, momentum, and kinetic energy.

To fully capture liquid break-up, the NGA code employs state-of-the-art interface transport techniques, the first of which is called Spectrally Refined Interface (SRI). The SRI method achieves local refinement in the form of quadrature points in each grid cell that contains the phase-interface, so that the level set function can be reconstructed using high order polynomials, thereby providing spectral accuracy [43]. Consequently, the local numerical errors in interface transport are reduced by the combined effect of increased resolution and increased order of accuracy. To render this method computationally efficient, the transport of the level set function is performed using a semi-Lagrangian technique, removing all constraints on the time step size. Increased spatial resolution is achieved without noticeably reducing the time step size for level set transport, which is a unique feature of this method. Level set based methods usually show good accuracy, but suffer from poor mass conservation properties. By increasing the local resolution of the level set function, this new approach reduces numerical errors, thereby limiting mass conservation errors [43, 47, 46].

A second interface transport technique, known as Accurate Conservative Level Set (ACLS) [42], is based on the conservative level set technique introduced in Olsson *et al.* [133]. By employing a hyperbolic tangent level set function that is transported and re-initialized using fully conservative numerical schemes, mass conservation issues that are known to affect level set methods are greatly reduced. The overall robustness of the numerical approach is increased by computing the interface normals from a signed distance function reconstructed from the hyperbolic tangent level set by a fast marching method [42]. In this chapter, the ACLS method is used for simulations of atomizing liquid jets in Sec. 3.7 to leverage its excellent mass conservation qualities with the accompanying severe interface topology changes. For all other simulations, the SRI method is used to capitalize on its exceptional accuracy.

3.6.1 Horizontal Interface

The analytic solution for a horizontal, flat interface in an electric field was initially used to validate the Poisson solver for the electric potential. As depicted in Fig. 3.6, the domain is rectangular of height L with Dirichlet boundary conditions for the potential, set to a constant value on top of the domain, ϕ_o, and zero at the bottom. The phase interface is located at H. Above the interface, the permittivity is ϵ_l and below ϵ_g with $\epsilon_l > \epsilon_g$. The analytic solution for the electric fields above and below the interface is

$$E^l = \frac{\phi_o}{(L-H)+(\frac{\epsilon_l}{\epsilon_g})H} \quad \text{and} \quad E^g = \frac{\phi_o}{\left(\frac{(L-H)}{(\epsilon_l/\epsilon_g)}+H\right)}. \tag{3.73}$$

Figure 3.7 shows computational results for one representative test case where $L = 1$, $\epsilon_r = 5$, $\phi_o = 100$, and $H = 0.4$, with $n = 60$ mesh points across the domain. The ghost fluid method provides a sharp and accurate solution for the electric field, and the error for this test case is zero to machine accuracy. This result is expected because the electric field in this case is constant in each phase, the jump in the electric field is both constant and normal to the interface, and therefore the implemented GFM scheme is exact.

3.6.2 Horizontal Interface with Charge Density

The analytic solution for a horizontal, flat interface with charge density is used to validate the PCG-BBMG Poisson solver for a case with a non-zero right hand side. The geometry is the same as in the preceding example discussed in Section 3.6.1 and Fig. 3.6. The upper region, representing the liquid, maintains a constant volumetric charge, q_o. The analytic solution for the liquid is governed by Poisson's equation, while the charge-free gas region is governed by the Laplace equation, as

$$\frac{d^2\phi^l}{dy^2} = q_o \quad \text{and} \quad \frac{d^2\phi^g}{dy^2} = 0, \tag{3.74}$$

with the electric field in the liquid and gas described by

$$E^l(y) = \frac{qy}{\epsilon_l} - \beta \text{ and } E^g = \epsilon_r\left(\frac{qH}{\epsilon_l} - \beta\right), \tag{3.75}$$

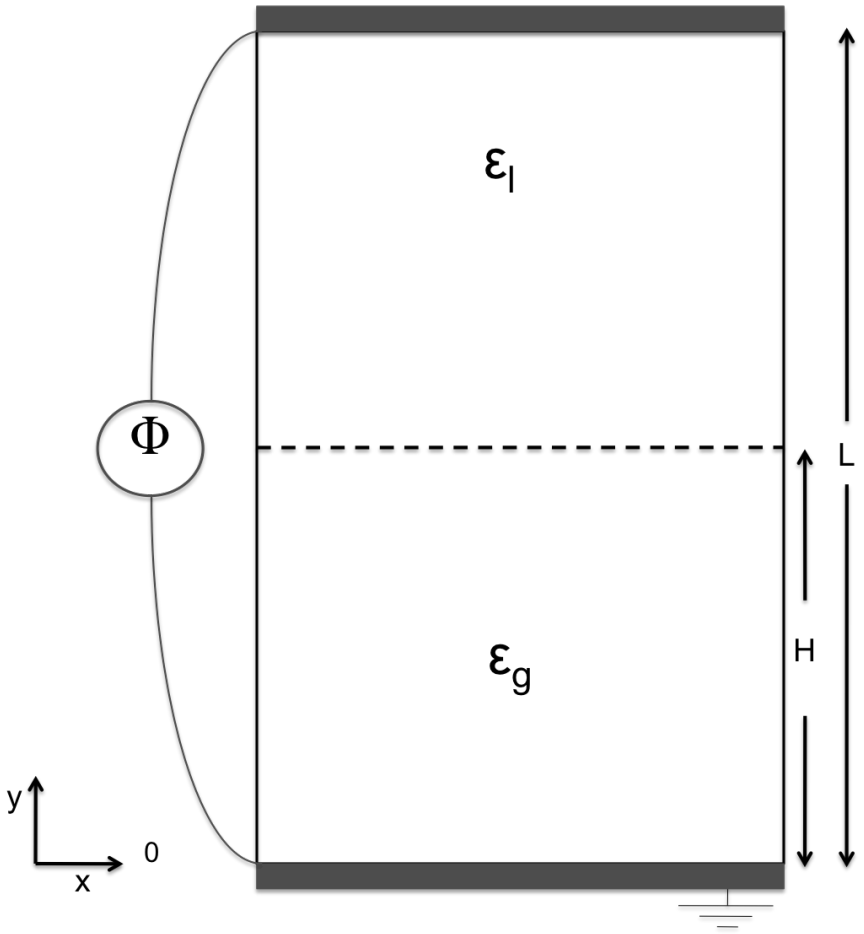

Figure 3.6: Schematic for the flat, horizontal interface case.

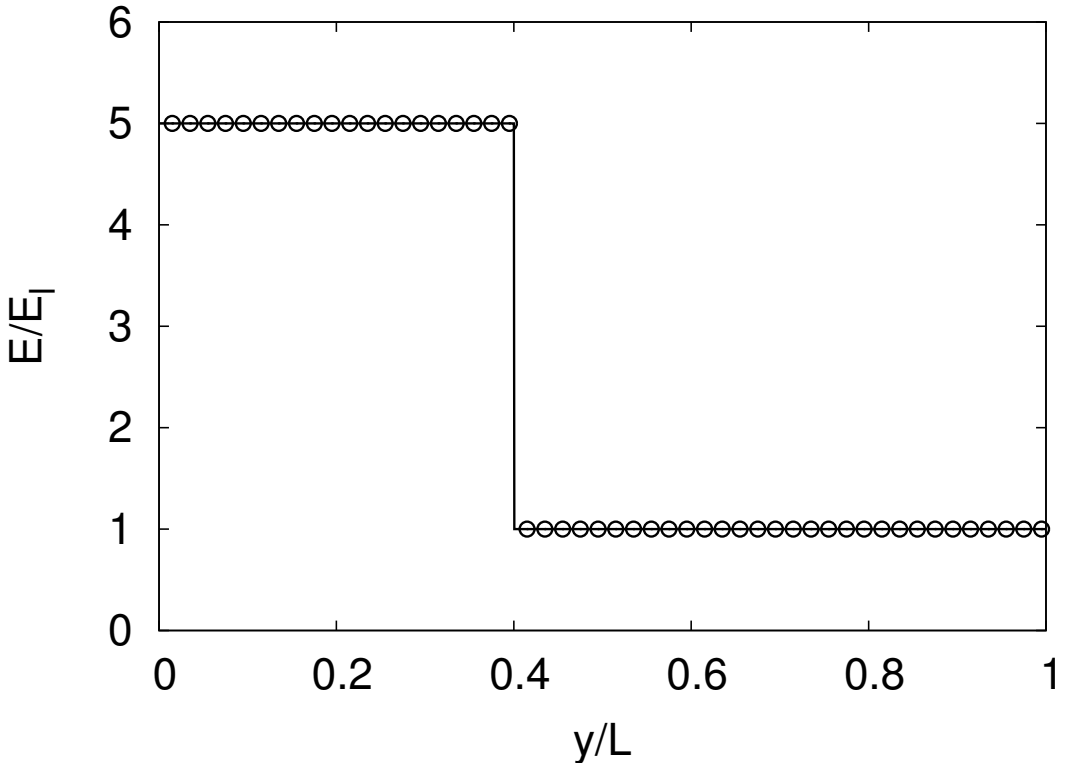

Figure 3.7: Distribution of normalized electric field normal to interface for horizontal interface test case. Symbols represent simulation, solid line represents theory.

where

$$\beta = \frac{\phi_o + ql^2/(2\epsilon_l) + \epsilon_r q H^2/\epsilon_l - qH^2/(2\epsilon_r)}{L - H + \epsilon_r H}. \tag{3.76}$$

The simulation parameters are the same as the uncharged horizontal interface test case. The value of q_o is chosen such that the ratio of charge to applied potential is unity. Figure 3.8 shows computational results for this case, illustrating excellent agreement of simulation and theory. Table 3.1 reports the normalized error in the y-direction electric field for this test case, showing second order convergence with mesh refinement.

Table 3.1: Normalized error in y-direction electric field for a horizontal interface with charge density.

Mesh	err E_y	order
50	1.1e-5	-
100	2.7e-6	2.02
200	6.8e-7	1.98

3.6.3 Motion of a Small Charged Droplet

A small point charge in a uniform electric field accelerates due to the Coulomb force, $\boldsymbol{f}_e = q\boldsymbol{E}$. In an attempt to reproduce this behavior, a small, spherical, charged droplet is placed in a uniform electric field. If the drop charge is small relative to the applied field, the spherical drop will not modify the electric field significantly, while feeling the effect of the Coulomb force. Provided that the Reynolds number is small enough, the droplet will also experience Stokes drag and will eventually reach a terminal velocity. Although a simple case, the charged drop test case evaluates the accuracy of the Coulomb force, as well as the interaction of the electric and viscous forces.

With the previous assumptions, the motion of the charged drop is governed by the ordinary differential equation

$$\rho_l V_l q E_y - 6\pi\mu R_o \frac{dy}{dt} = \rho_l V_l \frac{d^2y}{dt^2}, \tag{3.77}$$

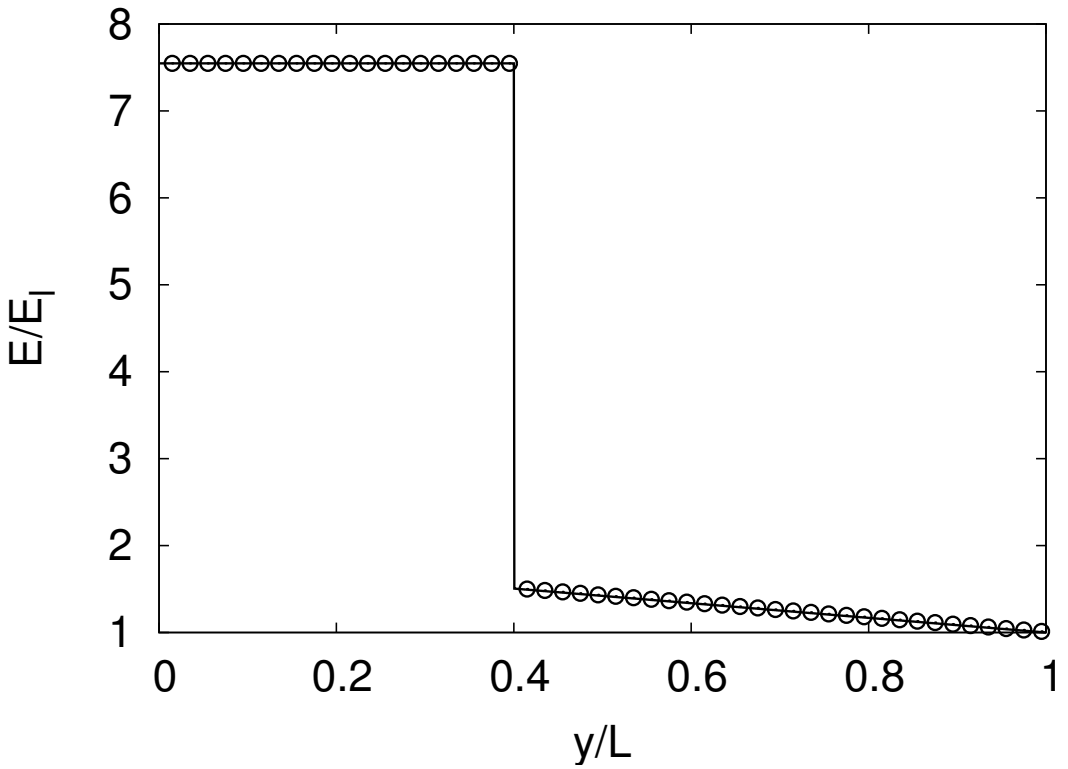

Figure 3.8: Distribution of normalized electric field for charged horizontal interface test case. Symbols represent simulation, solid line represents theory.

where V_l represents the liquid volume and R_o the drop radius. The corresponding terminal velocity, u_t, and time scale, τ are given as

$$u_t = \frac{\rho_l V_l q E_y}{6\pi\mu R_o} \quad \text{and} \quad \tau = \frac{R_o}{u_t}. \tag{3.78}$$

The relevant simulation parameters include the ratio of space charge to electric field strength, $\mathrm{Q_E} = qR_o/\epsilon E$, set to a value of 0.4, the viscosity ratio and density ratio to 10, the surface tension, $\gamma = 0.2$, relative permittivity, $\epsilon_r = 1$, and domain size of $10R_o \times 20R_o$. To limit temporal errors, the CFL is kept constant at 0.1. Figure 3.9 shows the velocity of the drop over time as it accelerates to terminal velocity for three levels of mesh refinement. Simulation results are compared to the theoretical solution for Eq. (3.77). The normalized error of simulation compared to theory at $t/\tau = 3$ converges on mesh refinement: 11% at $R_o/h = 3$; 2.2% at $R_o/h = 6$; and 0.4% at $R_o/h = 9$, where R_o/h represents the number of grid cells across the drop radius, thereby demonstrating good convergence and excellent accuracy even with coarse resolution. Importantly, the drop remains spherical throughout the simulation, as expected.

3.6.4 Dielectric Drop in a Uniform Electric Field

For a subsequent test case, we demonstrate a three-dimensional dielectric sphere placed in a uniform electric field. The drop is ideally suited to assess the accuracy and robustness of the EHD module. Spherical shapes are commonly observed in atomization processes and represent a canonical geometry for fuel injection applications. Additionally, the electric potential at the interface decays with r^{-2} and the electric field experiences large jumps proportional to the relative permittivity, ϵ_r. Since we explicitly address the jump conditions with the GFM approach, we expect this approach to accurately capture the physical phenomena with only a few grid points across the drop radius.

The analytic solution is provided in several references [81, 93] and has been demonstrated in other work as a representative test case to validate numerical methods [186, 10].

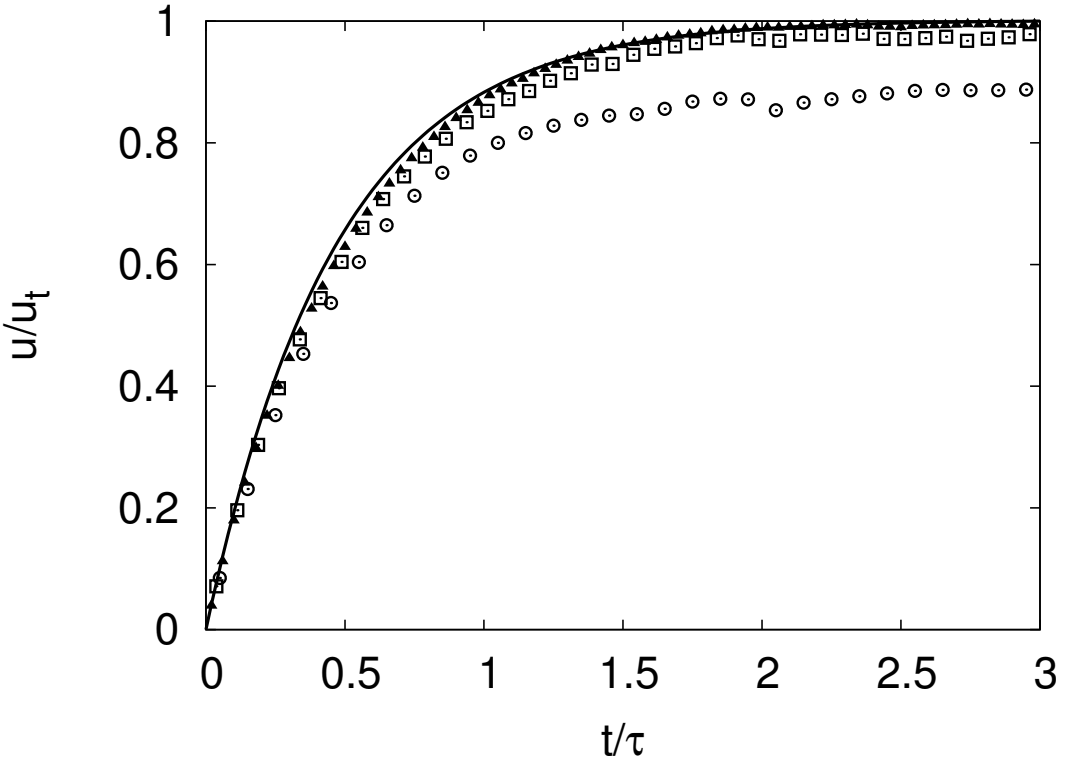

Figure 3.9: Simulation of charged drop accelerating to terminal velocity. $R_o/h = 3$ (circles), $R_o/h = 6$ (squares), $R_o/h = 9$ (triangles) compared to theory (line).

In this case we compare the numerical simulation result of the pressure in a spherical drop with the analytic prediction. The geometry is shown in Fig. 3.10. The electric field, E_o, is applied in the y-direction far away from the sphere. Since this case assumes a perfect dielectric, the environment is free of charge, and therefore the governing equation is Laplace's equation with appropriate boundary conditions. Superscripts l and g represent regions inside and outside the drop, respectively, and specifically ϕ^l is the potential inside the drop. The permittivities are known with $\epsilon_l > \epsilon_g$ and therefore the ratio of permittivities $\epsilon_r > 1$. The analytic solutions for the electric potential and magnitude of the electric field components are

$$\phi^l(r,\theta) = E_o r\left(\frac{-3}{\epsilon_r+2}\right)\sin\theta, \tag{3.79}$$

$$\phi^g(r,\theta) = -E_o r\sin\theta + \left(\frac{\epsilon-1}{\epsilon+2}\right)E_o\frac{R^3}{r^2}\sin\theta, \tag{3.80}$$

$$E_{t,r=R_o} = \left(\frac{3E_o}{\epsilon_r+2}\right)\cos\theta, \tag{3.81}$$

$$E^l_{n,r=R_o} = \left(\frac{3E_o}{\epsilon_r+2}\right)\sin\theta, \text{ and} \tag{3.82}$$

$$E^g_{n,r=R_o} = \epsilon_r\left(\frac{3E_o}{\epsilon_r+2}\right)\sin\theta. \tag{3.83}$$

The pressure jump across the drop is given by

$$[p]_\Gamma = \frac{2\gamma}{R} + \frac{1}{2}\left(\frac{3E_o}{\epsilon_r+1}\right)^2\left[\epsilon_l(1-\epsilon_r)\sin^2\theta + \epsilon_g(1-\epsilon_r)\cos^2\theta\right]. \tag{3.84}$$

A simulation is conducted with parameters $\mathrm{N}_E = \epsilon E^2 R_o/\gamma = 0.33$, $\epsilon_r = 10$, density and viscosity ratios set to unity, drop radius $R_o = 0.1$, and surface tension, $\gamma = 0.32$ for various levels of mesh refinement on a domain of $10R_o \times 20R_o$. Results for the convergence of the y-component of the electric field at two circumferential locations are reported in Table 3.2. The electric field at the cell center is very accurate at the pole and the equator, points where the field is exclusively defined by either the normal or the tangential component. At both points, the electric field shows reasonable convergence, with the error decaying between first- and second-order with mesh refinement. Table 3.3 reports the convergence of the electric

potential at all grid points in the neighborhood of the interface, which is defined by a sign change in the level set function compared to a neighboring cell in any direction. The electric potential shows limited convergence, remaining below first-order accuracy. These results are expected, since, as mentioned in Section 3.3, the numerical scheme is true to the normal jump in the electric displacement vector, $[\epsilon E_n]_\Gamma$, but smears the tangential jump, $[\epsilon E_{t_i}]_\Gamma$. Similar observations and rates of convergence were reported by Liu *et al.* [102]. It should also be noted that the choice of the GFM methodology represents an exchange of convergence for accuracy. In modeling multiphase and atomization processes, with characteristically small structures, numerical accuracy is expected to be the more important property. Figure 3.11

Table 3.2: Normalized error in y-direction electric field at the pole and equator of a dielectric drop.

R_o/h	err, $\theta = 0°$	order	err, $\theta = 90°$	order
5	2.3%	-	2.0%	-
10	0.8%	1.5	2.8%	-
20	0.4%	1.0	0.7%	2.0

Table 3.3: Convergence for electric potential, ϕ, at the interface of a dielectric drop.

R_o/h	L_2	order	L_∞	order
5	0.0137	–	0.0777	–
10	0.0086	0.67	0.0748	0.06
20	0.0061	0.50	0.0551	0.44

compares the simulation results to the analytic prediction of Eq. (3.84) for the pressure jump at the surface of the drop. The pressure jump is obtained across the sharp interface after one time step, prior to any deformation, and computed results agree well with theory. Table 3.4 shows the accuracy of the pressure jump at the equator, $\theta = 0°$, which is the point of the maximum pressure jump. The GFM scheme shows improvements in the accuracy of the

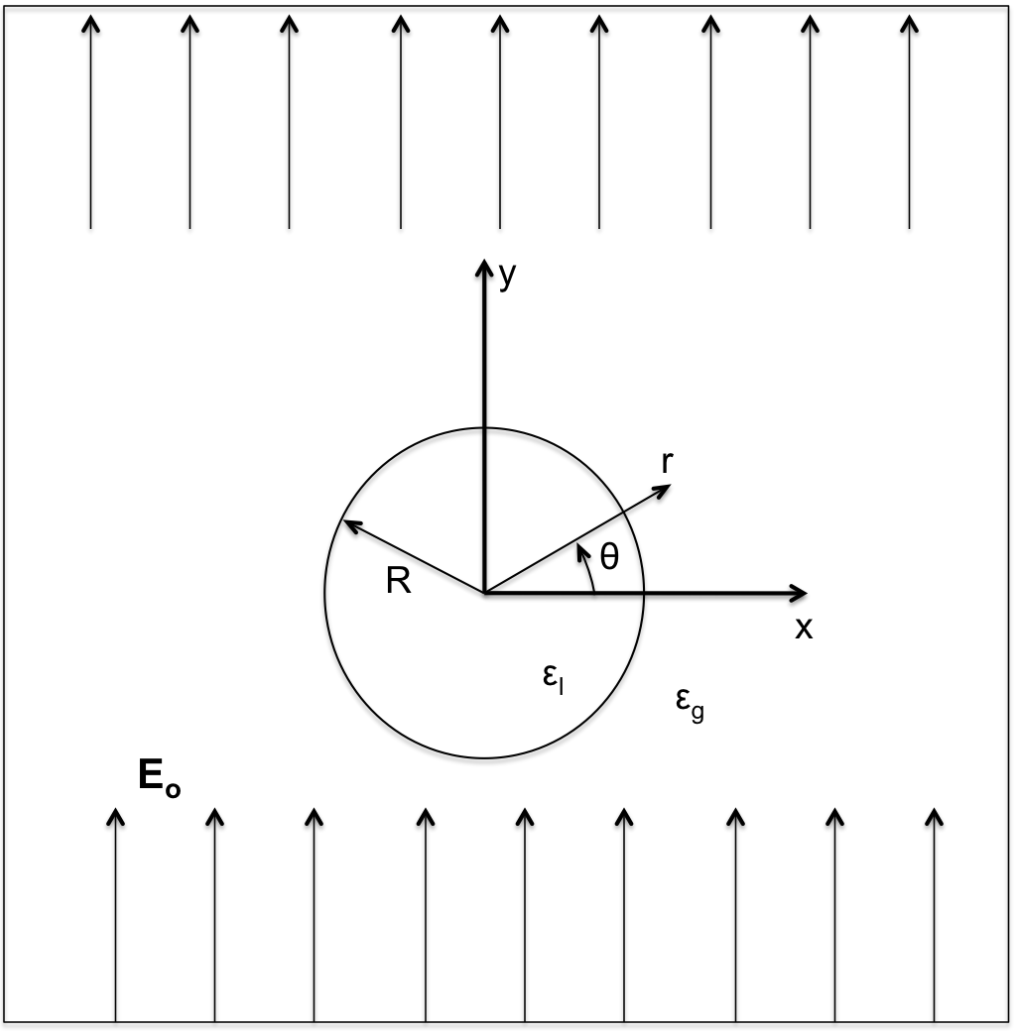

Figure 3.10: Schematic for dielectric cylinder in a uniform electric field test case.

pressure jump even with coarse resolution compared to previous work, such as the results reported for the same problem by Tomar *et al.* [186].

Table 3.4: Normalized error in pressure jump at equator ($\theta = 0°$) for a dielectric drop in uniform electric field.

	R_o/h	err $[p]_\Gamma$	order
NGA EHD	4	2.12%	-
NGA EHD	8	1.03%	1.09
NGA EHD	16	0.63%	0.71
Tomar *et al.* [186]	20	4.49%	-
Tomar *et al.* [186]	40	2.24%	1.00
Tomar *et al.* [186]	80	1.15%	0.96

3.6.5 Deforming Spheroidal Drop

A number of researchers have explored the case of a suspended drop in a uniform electric field, including Taylor [184], Landau and Lifshitz [93], Cheng and Chaddock [24], Sozou [176], Baygents and Rivette [10, 155], and Tomar *et al.* [186]. For this case, the geometry and electric field alignment are identical to that for the dielectric drop in the preceding section, as shown in Fig. 3.10. A spherical drop deforms when stressed by an externally applied electric field. A dielectric drop always deforms into a prolate spheroid with the major axis aligned with the electric field.

The eccentricity, e, depolarization constant, n, and the electric field inside the spheroidal drop are given by Landau [93]

$$\begin{aligned} e &= \sqrt{1 - a^2/b^2}, \\ n &= \frac{(1-e^2)}{(2e^3)}\left(\ln\left(\frac{(1+e)}{(1-e)}\right) - 2e\right), \\ E_l &= \frac{E_o}{(1-n) + n\epsilon_r}. \end{aligned} \tag{3.85}$$

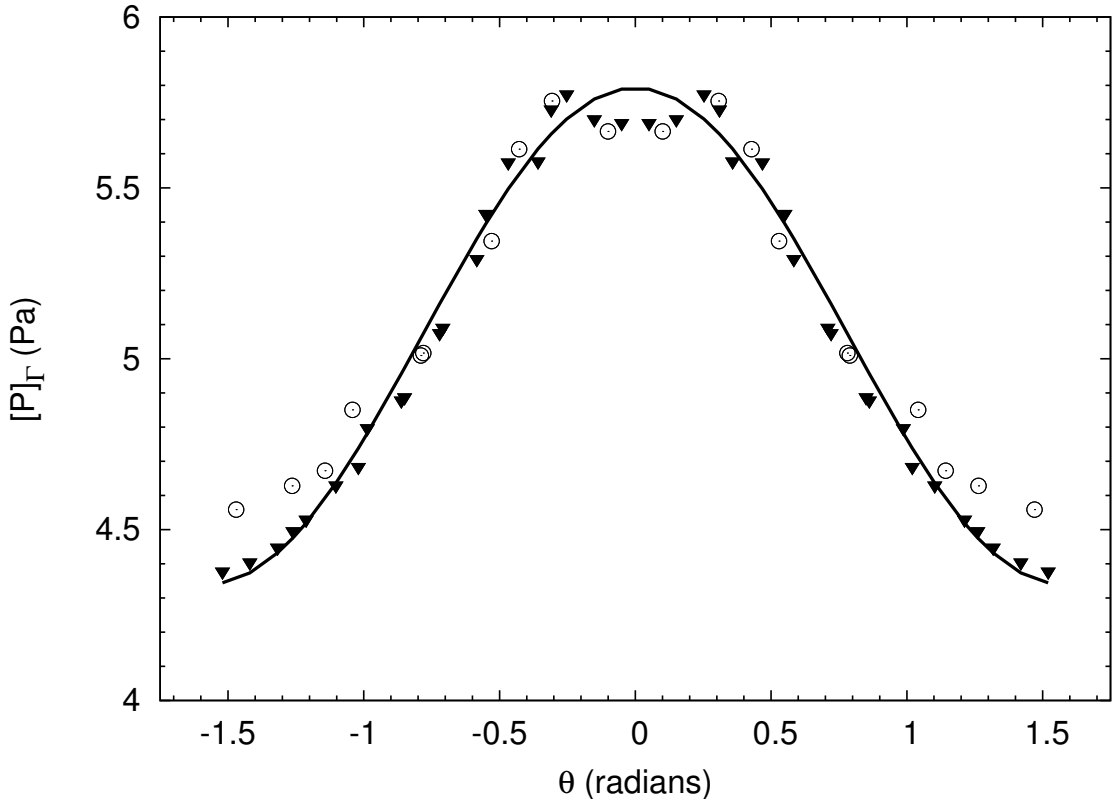

Figure 3.11: Pressure jump at the interface of a dielectric cylinder. Simulation results for $R_o/h = 4$ (circles), $R_o/h = 8$ (filled triangles) compared to analytic solution (line).

The force balance at the interface is

$$[p]_\Gamma \;=\; \gamma\kappa + \frac{\epsilon_g}{2}\left(\epsilon_r(E_n^l)^2 - (E_n^g)^2 + E_t^2(1-\epsilon_r)\right). \tag{3.86}$$

Considering two particular points, the *equator* ($x = a$) and the *pole* ($y = b$), the mean curvature, κ, is defined by the two principal radii of curvature, R_1 and R_2. For a prolate spheroid, these radii of curvature are given by

$$R_1 = a^2b^2\left(\frac{x^2}{a^4} + \frac{y^2}{b^4}\right)^{3/2} \quad \text{and} \quad R_2 = a^2\left(\frac{x^2}{a^4} + \frac{y^2}{b^4}\right)^{1/2}. \tag{3.87}$$

The mean curvature at the end of the major axis (*i.e.* at the pole) and the curvature at the end of the minor axis (*i.e.* at the equator) are given by Taylor [184] as

$$R_1^{-1} + R_2^{-1} \;=\; \begin{cases} \frac{2b}{a^2} & \text{at the pole,} \\ \\ \frac{a}{b^2} + \frac{1}{a} & \text{at the equator.} \end{cases}$$

The electric stress at the pole is due exclusively to the normal component (E_n); similarly the electric stress at the equator is due only to the tangential component (E_t). The tangential component is continuous at the equator, that is $E_t = E_t^l = E_t^g$ at $\theta = 0^o$. Therefore the pressure jump at these locations can be expressed as

$$[p]_\Gamma = \begin{cases} \gamma\left(\frac{2b}{a^2}\right) + \frac{\epsilon_g}{2}\left(\epsilon_r(E_n^l)^2 - (E_n^g)^2\right) & \text{at the pole,} \\ \gamma\left(\frac{a}{b^2} + \frac{1}{a}\right) + \frac{\epsilon_g}{2}\left(E_l^2(1-\epsilon_r\right) & \text{at the equator.} \end{cases} \tag{3.88}$$

Simulation parameters are based upon Cheng and Chaddock's stability analysis [24] and reported in Tomar *et al.* [186]: $\mathrm{N}_E = 0.49$, $r_a = R_o/1.2$, $r_b = 1.44R_o$, $[p]_\Gamma = 4.24$ Pa, $R_o = 0.1$, $\gamma = 0.32$, $\epsilon_r = 10.0$, and density and viscosity ratios of unity. The domain size used is $10R_o \times 20R_o$. To limit temporal errors, the CFL is kept constant at 0.1.

Results for the equilibrium drop pressure using the NGA EHD module are compared to results from previous work in Table 3.5. Equilibrium pressure is computed as a volume

average of all cells with a liquid volume fraction of 0.99 or greater. The NGA EHD module again shows good accuracy with few grid points. Figure 3.12 depicts the evolution of an initially spherical dielectric drop deforming into a prolate spheroid under the stress of an applied electric field, showing a smooth interface and iso-contours of electric potential.

Table 3.5: Dielectric drop in uniform electric field. Comparison of simulation with Tomar *et al.* [186] for computed equilibrium pressure jump at different levels of mesh refinement. Simulation L_1 and L_2 errors compared to theoretical predictions of Taylor [184], Landau [93], and Cheng and Chaddock [24].

	R_o/h	L_1 Δp	order	L_2 Δp	order
NGA EHD	3	0.029	-	0.09	-
NGA EHD	6	0.004	3.00	0.03	1.63
Tomar *et al.* [186]	4	0.145	-	0.22	-
Tomar *et al.* [186]	8	0.073	0.99	0.05	2.13

3.6.6 Interacting drops

To demonstrate the robustness of the numerical methods, a three-dimensional case of interacting droplets is demonstrated. Two identical spherical dielectric drops are placed in a uniform electric field. The drops are perfect dielectrics, which guarantees no charge in the bulk or at the interface. This test is similar to ones conducted by Baygents *et al.* [10] and Tomar *et al.* [186]. Drop parameters used in simulations include a relative permittivity, $\epsilon_r = 8.0$, electric Bond number, $N_e = 1.5$, and drop radius, $R_o = 0.1$, and drop spacing $h = 2R_o$, where $2h$ is the distance from drop center to drop center. The simulation is performed on a domain of size $10R_o \times 20R_o \times 10R_o$ discretized on a mesh of $64 \times 128 \times 64$. To limit temporal errors, the CFL is kept constant at 0.1. The evolution of the drops with time is depicted in Figs 3.13 and 3.14.

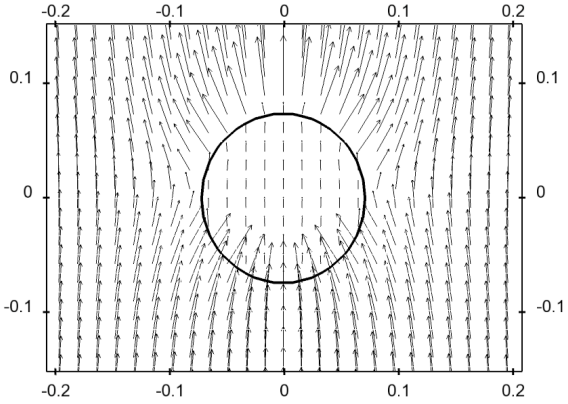

(a) Initial drop shape and electric field vectors, t=0.

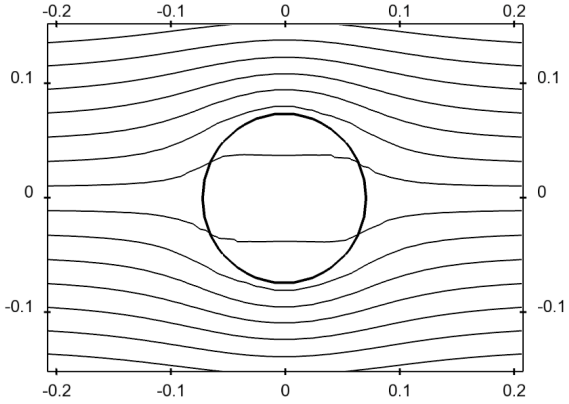

(b) Deformed drop and equipotential lines, t=0.1 s.

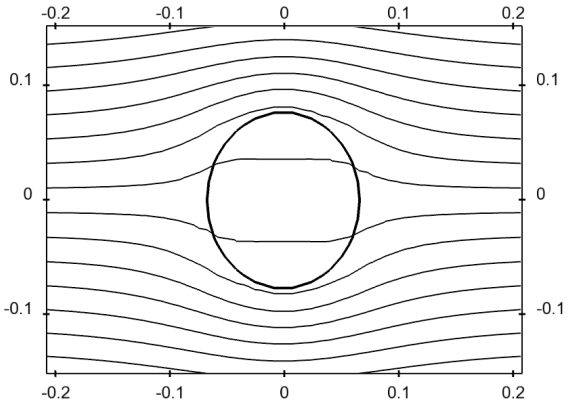

(c) Deformed drop and equipotential lines, t=0.5 s.

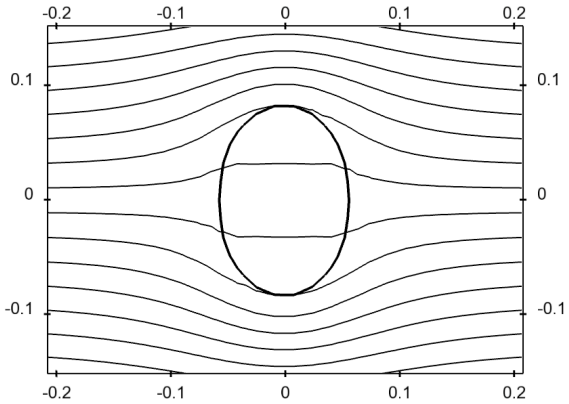

(d) Deformed drop and equipotential lines, t=8.0 s.

Figure 3.12: Evolution of a deforming, dielectric drop stressed by a uniform electric field.

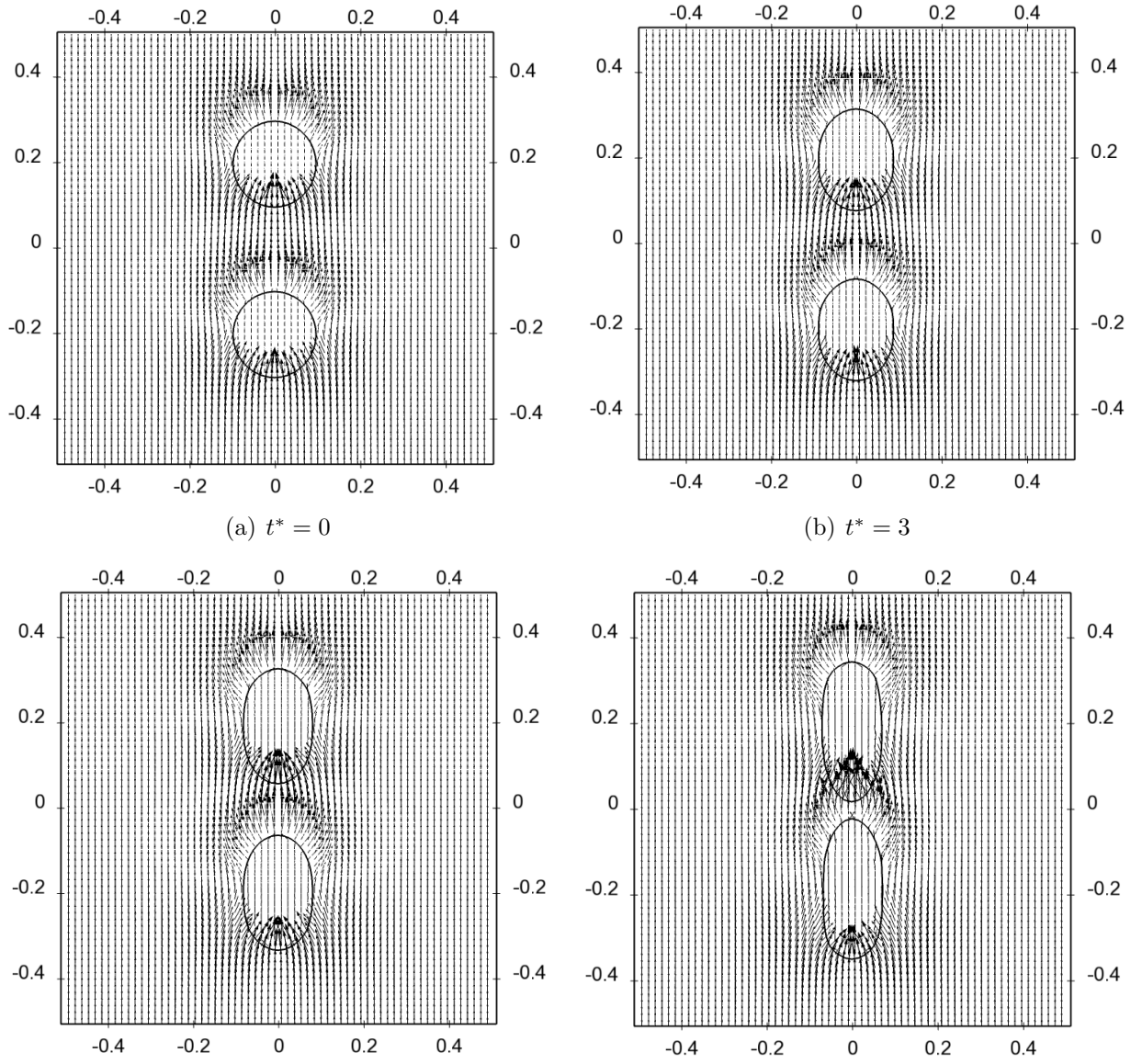

(a) $t^* = 0$

(b) $t^* = 3$

(c) $t^* = 5$

(d) $t^* = 7$

Figure 3.13: Interaction of deforming, dielectric drops stressed by a uniform electric field. Drops shown with electric field vectors.

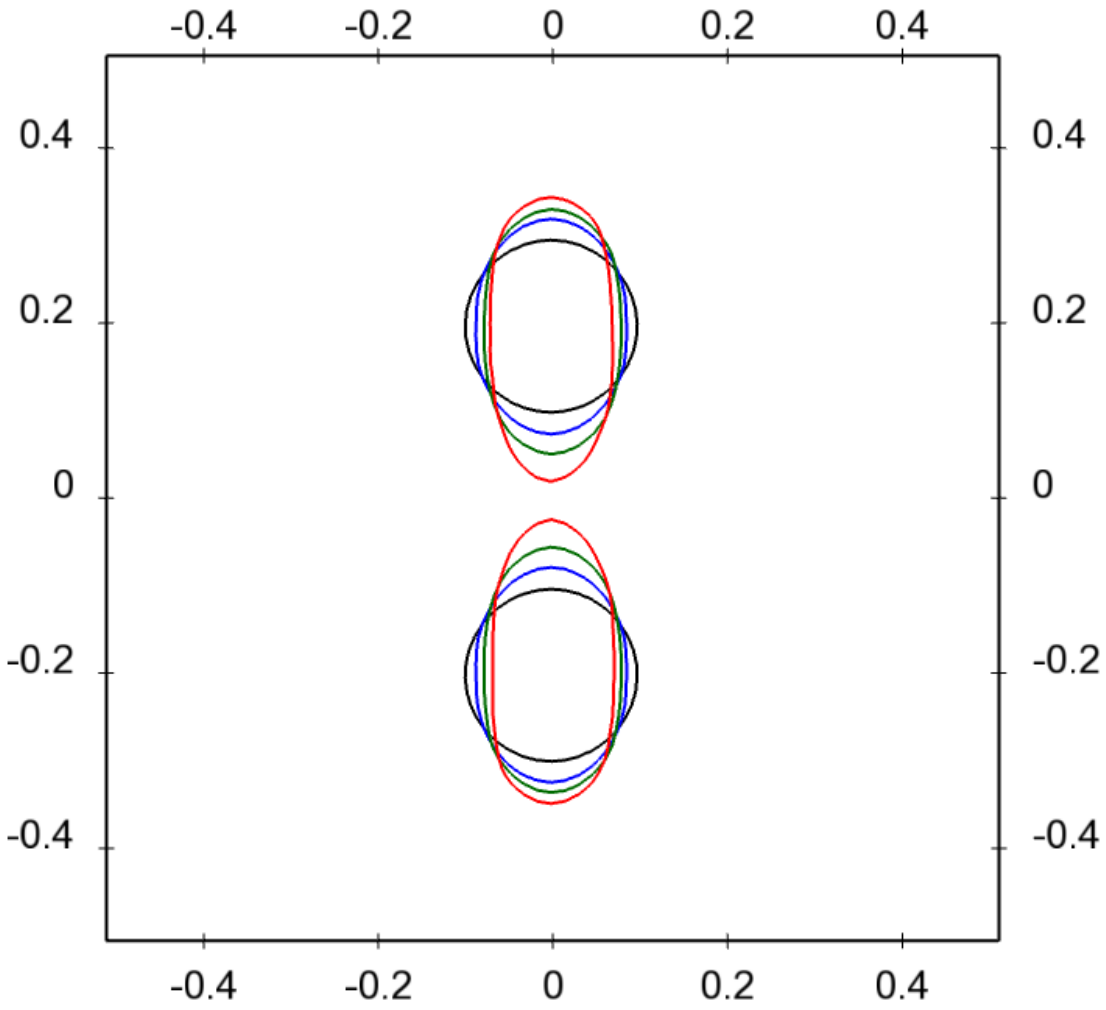

Figure 3.14: Evolution of two dielectric drops stressed by uniform electric field.

3.7 Simulation of a Charged and Uncharged Kerosene Jet

The validation cases presented heretofore are very limited in terms of complexity, covering flows governed by surface tension and viscous effects. In order to assess the performance of the proposed approach and demonstrate its robustness, charged and uncharged liquid jets in quiescent air are simulated. A charge injection scheme is modeled, similar to that investigated by many researchers elsewhere [204, 170, 87, 88, 97, 177]. The properties for the simulation are inspired by charge injection experiments performed by Shrimpton and co-workers [170, 171, 172, 204]. Parameters employed in both simulations are summarized in Table 3.6, with the electro-inertial number defined by $\mathrm{N}_{ei} = q^2 d_o^2/\epsilon\rho u^2$. Both charged and

Table 3.6: Parameters for charged and uncharged liquid kerosene jet. Total mesh size is 50.3 million grid points; d_o/h represents number of grid points across nozzle diameter

	Simulation		
Parameter	Uncharged	Charged	Charged Experiment
N_E	0	70	19
N_{ei}	0	1.25	0.09
q [C/m^3]	0	4	0.5
Re	2000		4900
We	850		1700
d_o [μm]	250		500
d_o/h	36		n/a
ρ_l/ρ_g	652		
μ_l/μ_g	56		
ϵ_r	2.2		
γ [N/m]	0.0235		

uncharged simulations correspond to a fast liquid jet of kerosene injected from a circular port of diameter d_o into quiescent air. For the charged simulation, we use a domain size of $L_x = 21d_o$, and $L_y = L_z = 7d_o$ discretized on a $768 \times 256 \times 256$ mesh. The boundary conditions implemented for this simulation are inflow and outflow conditions on the upstream and downstream $x-$faces, respectively, and zero electric potential on the $y-$ and $z-$faces.

The interface is initialized as a liquid cylinder spanning the domain. In Fig. 3.15, the uncharged and charged simulations are shown side-by-side for comparison. As expected, the uncharged simulation shows no disruption or break-up. Figure 3.16 depicts both simulations and the experimental shadowgraph presented in Fig. 3.2, and Fig. 4.6 highlights the qualitative similarities in the disintegration of the liquid core, droplet formation and ligament orientation between the charged simulation and experiment. Compared to the charged experiment shown in Fig. 3.2, the charged simulation employs a higher level of volumetric charge, q, to enhance liquid break-up in the absence of flow disturbances. In the charged simulation, many complex phenomena interact, resulting in a liquid break-up into ligaments and drops. The presence of numerous ligaments oriented radially outward from the axial centerline bears strong resemblance to the experiment photograph, Fig. 3.2. The charged simulation requires 70% more computational time than an uncharged jet. The addition of the electric potential Poisson equation and a complex space charge electric field account for the increase in computational expense in the charged simulation. Table 3.7 reports the proportion of time per time step required for each of the major computational components for the charged simulation using the NGA EHD module.

Table 3.7: Proportion of time taken by each solver for each time step for a charged liquid kerosene jet simulation. The multiphase step in this simulation includes the computational time for the electric potential Poisson solver.

Multiphase including EHD	44%
Velocity	12%
Pressure	42%
Other	2%

3.8 Summary

This chapter details the development, implementation, and validation of a sharp numerical scheme for multiphase electrohydrodynamic flows. A ghost fluid method (GFM)

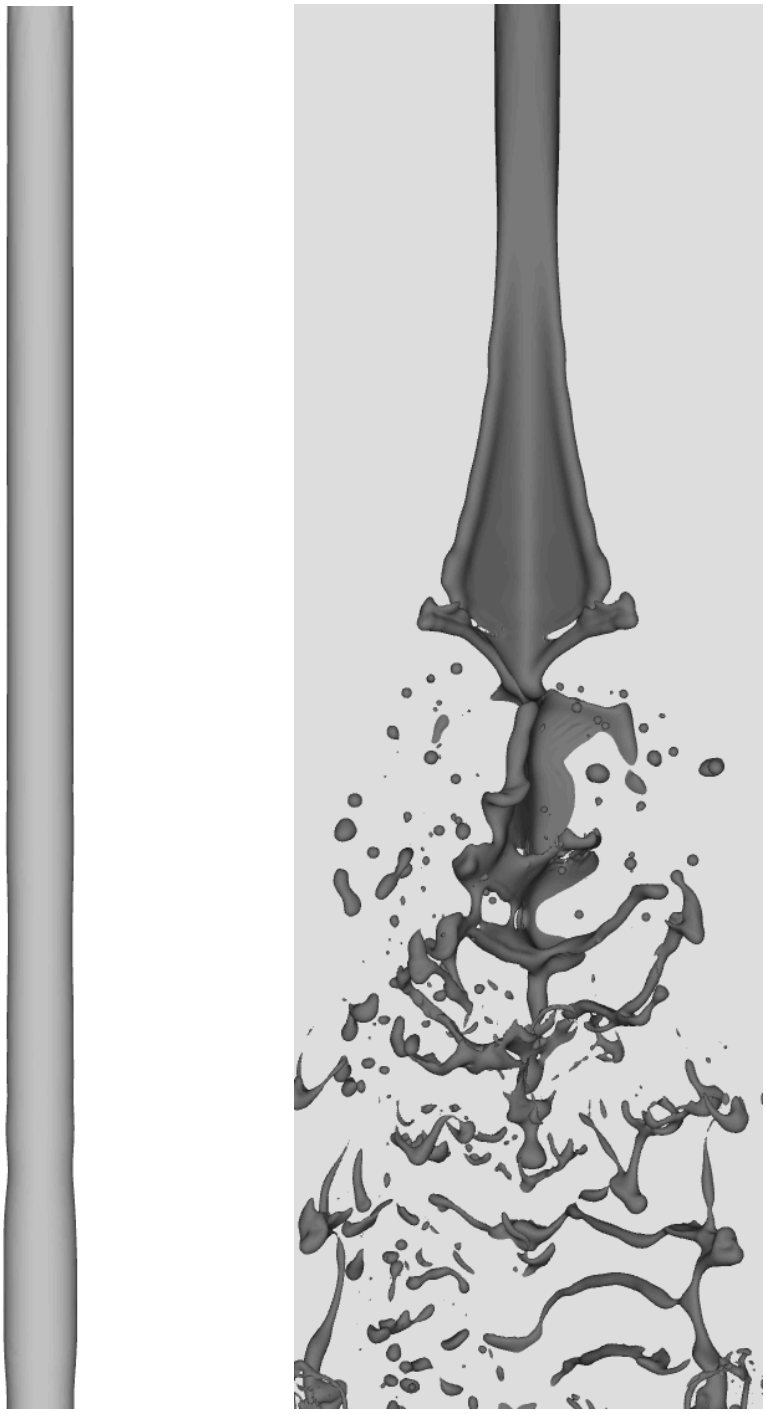

(a) Uncharged simulation. (b) Charged simulation.

Figure 3.15: Comparison of uncharged and charged simulations of liquid kerosene jet.

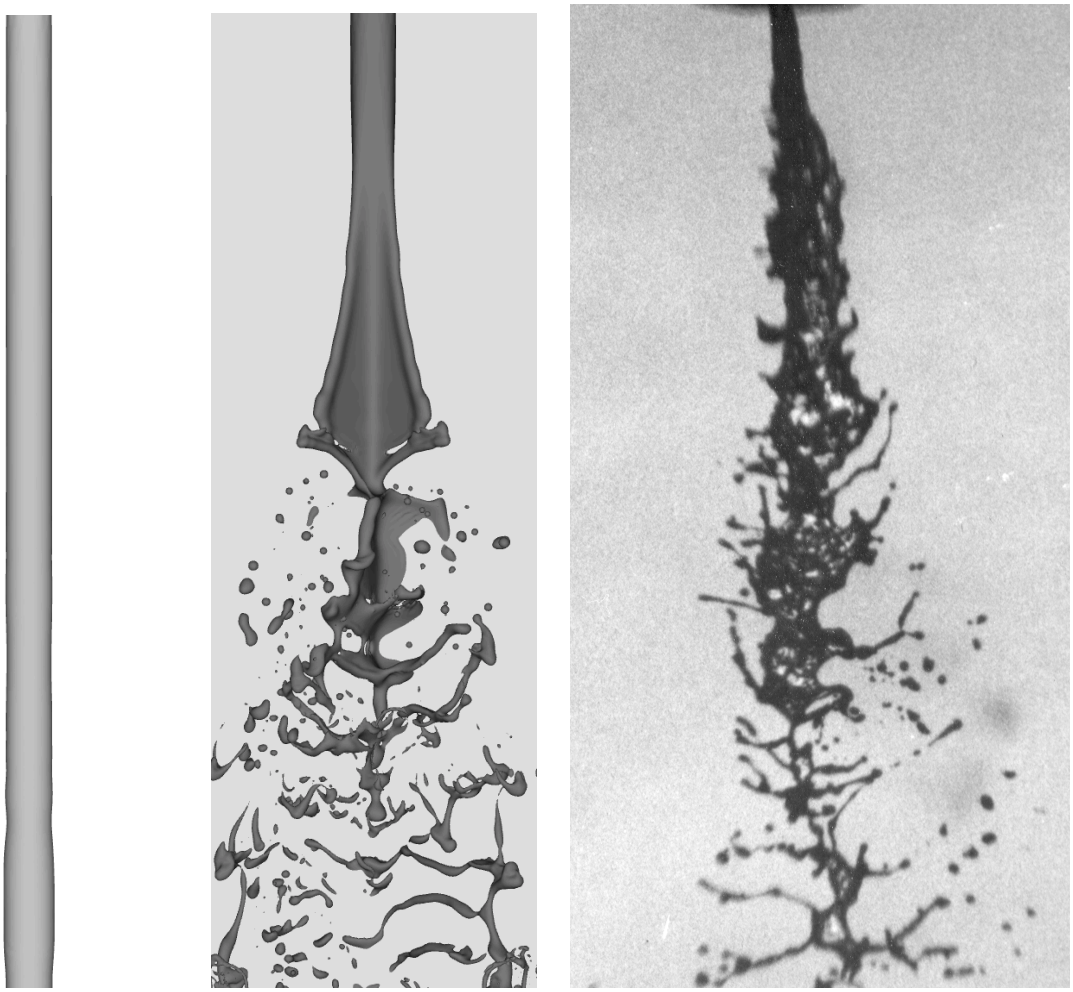

(a) Uncharged simulation. (b) Charged simulation. (c) Charged simulation.

Figure 3.16: Comparison of uncharged and charged simulations of liquid kerosene jet, and experiment [170].

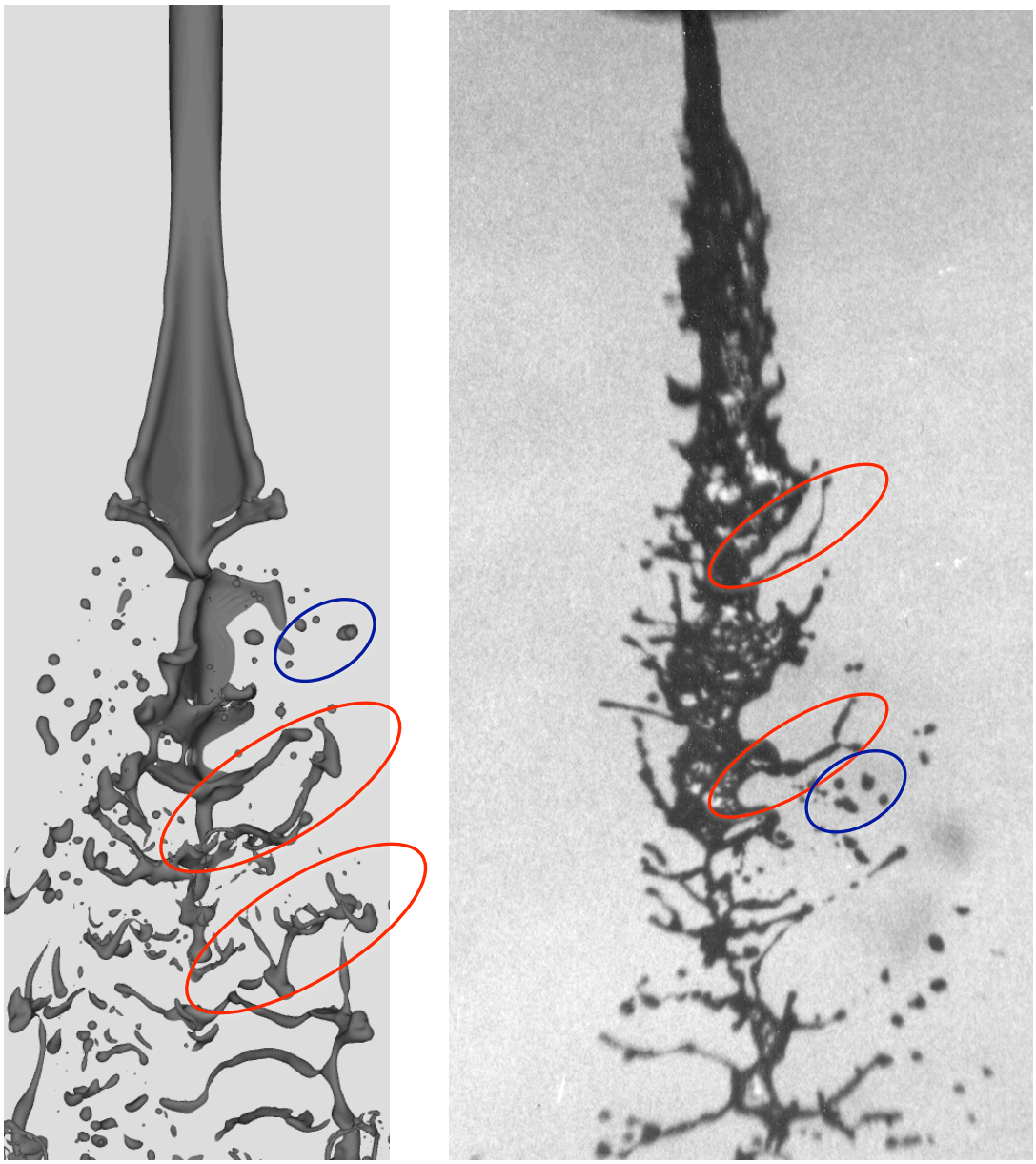

(a) Charged simulation.

(b) Charged experiment [170].

Figure 3.17: Comparison of charged simulation and experiment [170], highlighting qualitative similarity in drop and ligament formations.

approach is employed to solve for the electric potential Poisson equation in a sharp, accurate and robust manner. EHD boundary and jump conditions are implemented using a similar methodology, and subsequently used to solve the pressure Poisson equation. Electric charge is modeled in the bulk, with an initial assumption of no surface charge. The methods detailed here are implemented within the NGA code, which employs state-of-the-art interface tracking technique coupled to a robust and accurate Navier-Stokes/Ghost fluid solver.

Previous work by Tomar [186] implemented a weighted harmonic mean (WHM) interpolation scheme to smoothen the electric properties at the interface, a coupled level set and volume-of-fluid (CLSVOF) algorithm for tracking the phase interface, and the continuum surface force (CSF) method for the electric surface forces. We develop a new representation for the interface jump conditions, employing a generalized Taylor series expansion to directly and accurately account for the discontinuities across the interface. We show that the GFM can be extended to solve the electric potential Poisson equation. The GFM is also extended to the EHD jump conditions to accurately model the strong interfacial coupling. Compared to a CSF-type approach for handling discontinuities, the application of GFM in the NGA code yields more accurate results with fewer grid points. Several test cases validate the overall methodology and demonstrate the improvements in both accuracy and efficiency compared with the current state of the art for EHD modeling. The model is applied in direct numerical simulation of a charged and uncharged liquid Kerosene jet to demonstrate the robustness of the methods. The simulation results are compared to classic experiments and suggest reasonable qualitative agreement.

To fully explore the dynamics of EHD and its role in primary atomization, fully three-dimensional DNS of atomizing EHD liquid jets must be conducted. The complicated interplay between classical liquid disintegration mechanisms and electric disruption will require large-scale simulations to resolve. Several fundamental yet unanswered research questions will guide initial simulations of EHD atomization, such as the roles that the electric Bond number, N_E, and the electro-inertial number, N_{ei}, play in electrostatic-enhanced atomiza-

tion for complex geometries and three-dimensional flows. The methodology proposed and validated in this chapter establishes a point of departure for large-scale, high-fidelity DNS of EHD atomization. Results of a detailed numerical study of electrostatic-aided atomization are the focus of Chapter 4.

Chapter 4

Detailed Simulations of Electrically Charged Diesel-type Jets

EHD flows and sprays have drawn considerable interest over the past three decades, progressing from pioneering work by Kim and Turnbull [88]. Shrimpton and co-workers have studied the technique of "charge injection" through experimental [153, 154, 169, 170, 171, 204] and numerical [166, 168] investigations. Notwithstanding these efforts, the complex interactions among electrostatic charge, electric fields, and the dynamics of atomizing liquids are not well understood. Considering the challenges and expense of experiments, high-fidelity numerical simulations should be able to provide some clarity to the underlying fundamentals and dynamics of EHD atomization. While numerical simulations of realistic liquid break-up are challenged by the computational expense required to resolve small structures and the correspondingly large, parallel resources necessary to perform these simulations, recent advances in scientific computing and numerical methods renders simulation a viable complement. With the possibilities of simulations-based research in mind, this chapter extends the numerical methods and computational scheme detailed in Chapter 3 to perform fully three-dimensional direct numerical simulations of electrically charged liquid jets.

4.1 Objectives

To fully explore the dynamics of EHD and its role in primary atomization, three-dimensional DNS of atomizing EHD liquid jets must be conducted. The methodology proposed and validated in Chapter 3 establishes a point of departure for large-scale, high-fidelity

DNS of EHD atomization. In this vein, two fundamental, yet unanswered, research questions guide this initial numerical investigation of EHD atomization:

1. **Role of electro-inertial number, $\mathbf{N}_{ei}$.** Is level of injected charge, q effective in enhancing EHD atomization and controlling the relevant characteristics of the spray? Does q govern the drop size distribution and the onset of atomization for liquid dielectric hydrocarbons, or are these parameters truly *electrohydrodynamic*?

2. **Role of surface tension**. What is the interplay and relative importance of electrostatic effects compared to surface tension for atomization of charged dielectric liquids? What roles do the electric Bond number, N_E, and liquid Weber number, We_l play in primary atomization for the types of flows and sprays considered herein?

To explore these research questions, detailed numerical simulations are performed using carefully chosen parameters. The parameters are selected to gain an understanding of the underlying physical phenomena while maintaining reasonable confidence in the numerical techniques. The following objectives guide this initial investigation of EHD atomization:

- Assess the hydrodynamic inflow conditions for the multiphase simulations;
- Visualize primary atomization and qualitatively compare simulation results to available experimental data;
- Identify principal atomization mechanisms;
- Analyze the effects of the electro-inertial number;
- Analyze the effects of the liquid Weber number;
- Collect and analyze statistics for primary atomization of a charged Diesel-type jet.

This chapter begins with an overview of the simulations test matrix and a description of the computational domain and resolution factors, followed by a brief assessment of hydrodynamic inflows to the multiphase simulation. Then, a series of numerical simulations

is performed across a range of relevant non-dimensional parameters, and some qualitative, global characteristics of each simulation are discussed. An algorithm to identify liquid structures is implemented and used to collect statistics for all structures at different times in each simulations. Statistics are analyzed and spray characteristics, such as the onset of atomization, drop size distribution, and spray cone angle, are assessed. Finally, some simple models are proposed and compared with statistical results.

4.2 Flow Configuration

A charged liquid Diesel-type jet is simulated with liquid injection through a circular port of diameter d_o. The properties for the simulation are inspired by charge injection experiments performed by Shrimpton and co-workers [170, 171, 172, 204]. Simulation parameters are summarized in Table 4.1, with injecting nozzle diameter, d_o, and its bulk velocity, U_o The domain size employed is $L_x = 30d_o$, and $L_y = L_z = 15d_o$ discretized on a uniform mesh of different sizes commensurate with the number of points per nozzle diameter, N_{dia} reported in Table 4.1. The boundary conditions implemented for all simulations are Dirichlet boundary specifying bulk inflow at the upstream $x-$ face, convective outflow conditions on the downstream $x-$face, and zero electric potential on the $y-$ and $z-$faces. The interface is initialized as a liquid cylinder spanning the domain.

As an initial investigation, a campaign of three-dimensional simulations is outlined here.

Four simulations for low density ratios, Cases A0 - A3, are performed for high electric Reynolds number liquid jets, as summarized in Table 4.1, including an uncharged baseline case (A0). These cases strive to explore principal effects of electro-inertial number and liquid Weber number on the onset of atomization and drop-size distribution. The density ratio is set to $\rho_l/\rho_g = 50$, which is commonly observed in Diesel engines and low enough to avoid numerical issues that can plague higher density ratio simulations. The low Reynolds number is chosen to reduce the likelihood of natural breakup in the uncharged case so that this

simulation may be used as a baseline for qualitative assessment. The lower limit of electric charge is selected such that liquid break-up occurs in the latter half of the domain in the axial direction, while the upper limit of volumetric charge is limited by experimental observations of corona discharge. Additionally, the upper limit of electric charge is limited by the computational domain size, since early and rapid liquid disintegration quickly fills the domain and alters the statistical analysis for cone angle. Visualization, qualitative assessment, and statistical analysis are reported in §4.4.

Table 4.1: Summary of liquid jet EHD simulations.

Case	ρ_l/ρ_g	μ_l/μ_g	Re_l	We_l	N_{ei}	Oh	N_{dia}
(A0)	50	50	2000	1000	0	0.015811	26
(A1)	50	50	2000	1000	0.10	0.015811	26
(A2)	50	50	2000	1000	0.15	0.015811	26
(A3)	50	50	2000	1000	0.20	0.015811	26

The resolution required in the computational domain is specified for a DNS simulation of EHD atomization of a liquid jet. The proceeding methodology summarized in this section follows previous work conducted using the NGA code. A schematic of the computational domain that will be employed in our proposed detailed simulations is shown in Fig 4.1. The charged liquid jet is injected from a circular port of diameter D into a quiescent gas from the $y-z$ face. The computational domain previously used to study the Diesel jet is a box of dimensions $L_x \times L_y \times L_z$. In order to prevent the domain boundaries from affecting the evolution of the jet, we set $Lx = 20d$, and $Ly = Lz = 5d$. This domain size has been successfully employed in previous work using the NGA code. However, the addition of the electrostatics requires additional domain spacing in the lateral $(y-z)$ plane to account for the possibility of greater droplet dispersal. The validation case in Chapter 3, Figure 4.6, employs a domain size of $Lx = 21d$, and $Ly = Lz = 7d$. The figure illustrates that this domain size is too small for the parameters used, with liquid structures reaching the lateral sides of

the domain at approximately the axial mid-point. Therefore, for subsequent multiphase simulations reported here, an expanded domain size of $Lx = 30d$, $Ly = Lz = 15d$ is used.

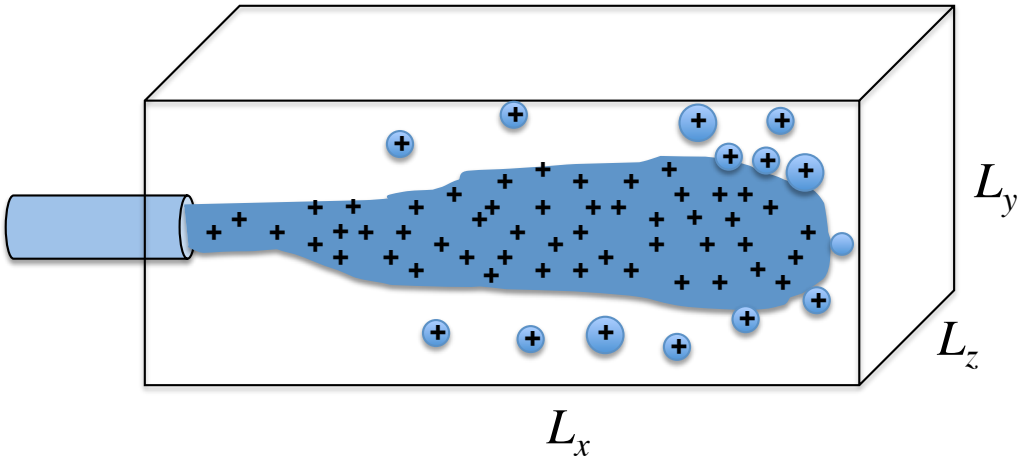

Figure 4.1: Sketch of computational domain employed in simulations

The dynamics of EHD atomization are expected to be dominated by liquid disintegration mechanisms as well as electric disruption. Due to the low values of electric Bond number, N_E, employed in these simulations, it is expected that the Weber number will be the principal determinant of mesh size. Previous studies have shown that drops with Weber numbers of around 10 do not undergo further break-up [96]. This imposes a practical limit on mesh sizing within the computational domain. In our proposed simulations we will require that the Weber number based on mesh spacing, Δx, be smaller than 10. Since the liquid is expected to occupy most of the domain, a uniform mesh is preferred. Using the expanded domain size specified above and a representative liquid Weber number, $We_{liq} \approx 500$, an estimate of the number of grid points in a uniform mesh for a single simulation can be described as

$$We_{\Delta x} = \rho_{liq} U_{liq}^2 \Delta x / \sigma < 10, \tag{4.1}$$

$$N_{dia} > 0.1 We_{liq}, \tag{4.2}$$

$$N_{tot} \approx 1000 d^3 = 1000(0.1 We_{liq}^3). \tag{4.3}$$

For $We = 500$ an estimate for the number of points, N_{tot}, is 125 Million.

4.3 Evaluation of Hydrodynamic Inflow Conditions

The validation results for a three-dimensional simulation of an electrically charge liquid jet in §3.7 are promising. However, the charged jet with an undisturbed bulk inlet flow is not realistic, and some of the liquid breakup may be attributable numerical errors. A brief survey of experimental work shows that hydrodynamic, as well as EHD effects within the nozzle, will produce flow disturbances at the nozzle exit plane. The most descriptive experimental setup is provided by Shrimpton, with details of nozzle body size and emitting electrode placement [169, 170, 171]. Some of Shrimpton's experimental cases fall in the laminar range, with Reynolds number based on nozzle diameter and average nozzle velocity as low as 2000. The majority of his experiments are run in the turbulent or transition range, and therefore the hydrodynamics will introduce flow disturbances through turbulent kinetic energy and large-scale eddies in the low-range of turbulent Reynolds numbers. The placement of the emitting electrode may also contribute to flow disturbances. With these practical factors in mind, a brief investigation of different inflow configurations is deemed relevant. In this section, multiphase simulations are performed using a bulk inflow, and a fully turbulent inflow using the results of a turbulent pipe preliminary simulation. Effects of different inflows are compared to experimental results.

4.3.1 Bulk Inlet

The multiphase simulations employing bulk inflow were presented in §3.7. The simulation is shown here for reference. Figure 4.2 reveals that the domain size chosen for this simulation is too short in the lateral (y and z) directions. The domain size was increased from previous work used to study turbulent atomization of an uncharged Diesel jet to account for greater lateral dispersion resulting from the presence of space charge. However, Fig. 3.17(b) clearly shows that liquid structures reach the domain boundary near $x \approx 15d_o$.

To remedy this issue, the domain size was increased for subsequent simulations.

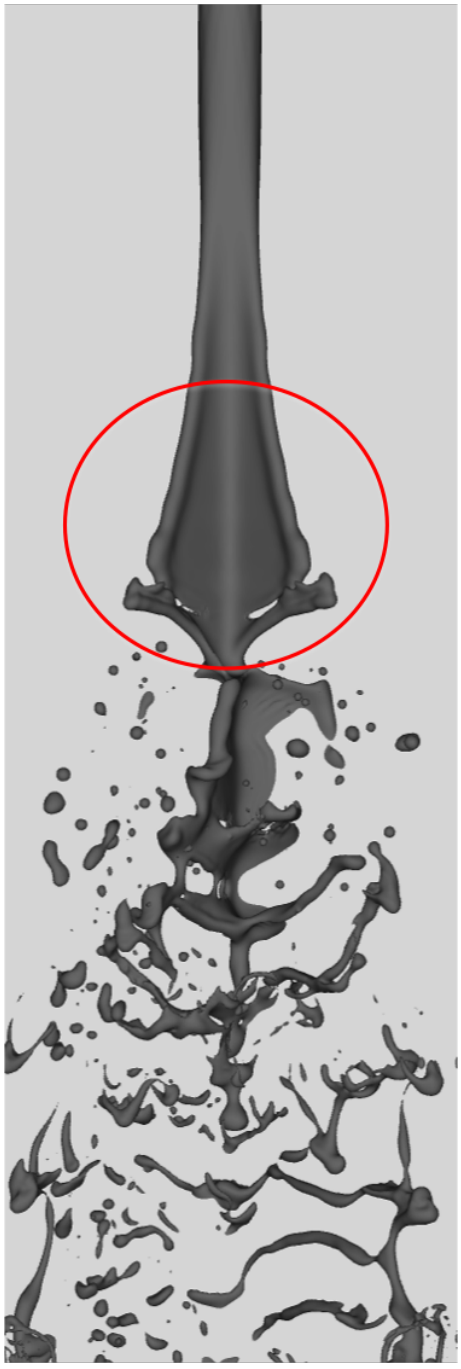

Figure 4.2: Evidence of mesh alignment error in validation simulation employing undistrubed bulk inflow.

While the bulk inflow simulation displays promising qualitative agreement with ex-

periment, the quantity of electric charge employed in the simulation is much higher than experiment. Due to the high electric charge in a cylindrical jet and the boundary conditions on a rectangular domain, this simulation exhibits some evidence of mesh alignment. To explore this issue, a simple test is conducted to demonstrate the effect of the Coulomb force implementation. A two-dimensional simulation of a charged liquid cylinder in a rectangular domain is conducted. Simulations employ 2D periodic cylinders, $R_o = 0.1$, with Dirichlet boundary conditions for the electric potential ($\phi = 0$) on all four sides of a domain of $10R_o \times 10R_o$ with mesh spacing, R_o/h, set to 10. The relative permittivity is set to the value for kerosene, $\epsilon_r = \epsilon_l/\epsilon_g = 2.2$. The ratio of Coulomb force to surface tension takes the form of an electric Bond number, $\mathrm{N}_E = q^2 r_o^3/\gamma\epsilon_o\epsilon_r$, and in this test N_E is set to 100, approximately one order of magnitude greater than experimental value in order to exaggerate the influence of the Coulomb force.

Two simulations are performed and evaluated. The first simulation employs a symmetric circular cylinder. Figure 4.3 displays the mesh alignment of the symmetric cylinder, with the Coulomb force stretching the interface non-uniformly toward the corners of the square domain. The other simulation employs a circular cylinder with a slightly disturbed surface. The surface disturbances are introduced using a cosine function for mode $m = 3$ and a disturbance amplitude equal to $R_o/500$. Also shown in Fig. 4.3 is the disturbed surface case, illustrating that the small disturbances are magnified by the Coulomb force. The surface is deformed in the direction of the three disturbances, commensurate with theory. Given the results of this test, it is expected that the introduction of flow disturbances in the inflow, as well as lower levels of space charge, will eliminate any issues of mesh alignment.

4.3.2 Fully Turbulent Inlet

A second simulation is conducted with relevant non-dimensional parameters matched to Shrimpton's experiment, Case 2 [170]. Simulation parameters are summarized in Table 4.2. To introduce flow disturbances, a turbulent pipe preliminary simulation is performed

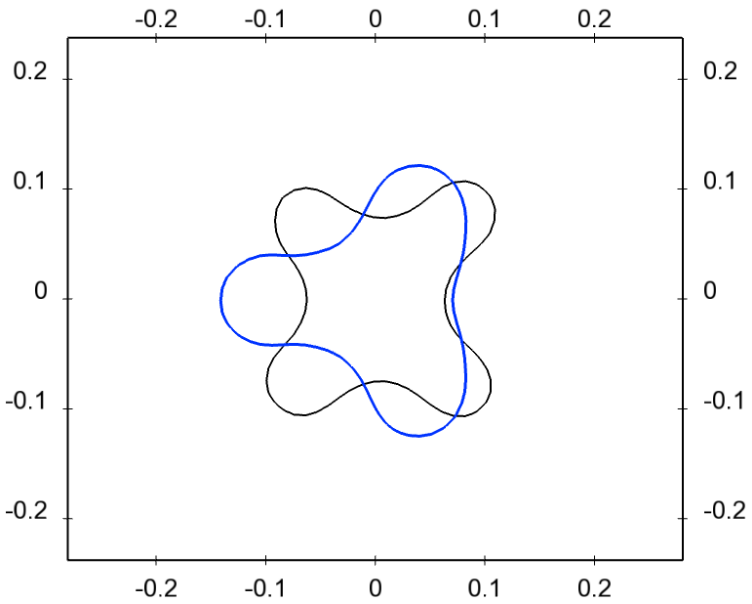

Figure 4.3: Evolution of initially perturbed interface (blue) and unperturbed interface (black) under the influence of the Coulomb force and surface tension.

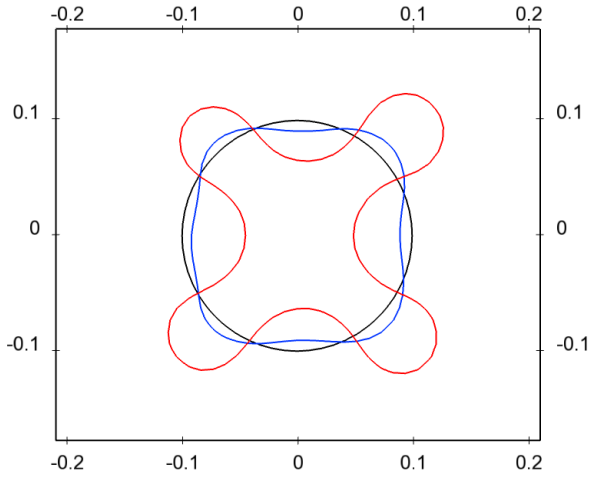

(a) Mesh alignment test with disturbances introduced at mode m=4.

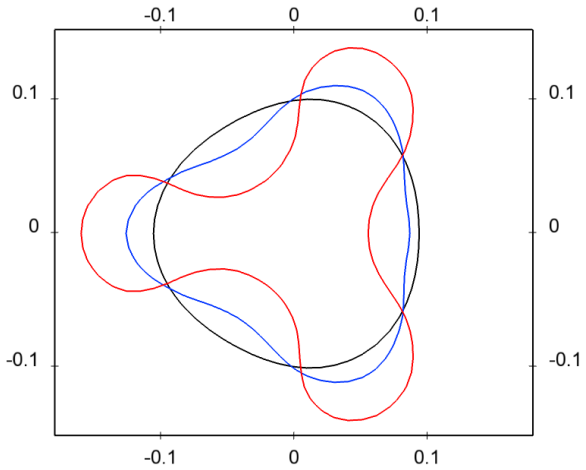

(b) Mesh alignment test with disturbances introduced at mode m=3.

Figure 4.4: Mesh alignment test simulation with interface disturbance of $R_o/500$.

and then used as the inflow to the multiphase simulation. The turbulent pipe preliminary simulation is performed with Re = 4900 to match the experimental value. To ensure fully developed turbulence, the inflow simulation is run until the axial skin friction coefficient, C_{f_x} reaches an approximately constant value, as depicted in Fig. 4.5. The simulation is run in cylindrical coordinates on a domain of $20d_0 \times d_o \times 2\pi$ and discretized on a mesh of $192 \times 96 \times 64$. As mentioned previously, the domain size was increased for this simulation from the $20d_o \times 7d_o \times 7d_o$ domain employed in the bulk inlet simulation to $20d_o \times 10d_o \times 10d_o$ in order to accommodate increased lateral dispersion.

Figures 4.6(a) and 4.6(b) compare Shrimpton's experiment [166] and the charged simulation. Unlike the bulk inflow case, the turbulent inflow shows no evidence of mesh alignment, attributable to lower levels of volumetric charge as well as the presence of flow disturbances introduced by the fully turbulent inflow that contribute to a non-uniform interface at the nozzle exit. The simulated jet shows more liquid disintegration than the experiment, especially near the axial centerline. The experiment shows the liquid core largely intact with satellite ligaments that begin to tear away from the core. The greater disintegration in the

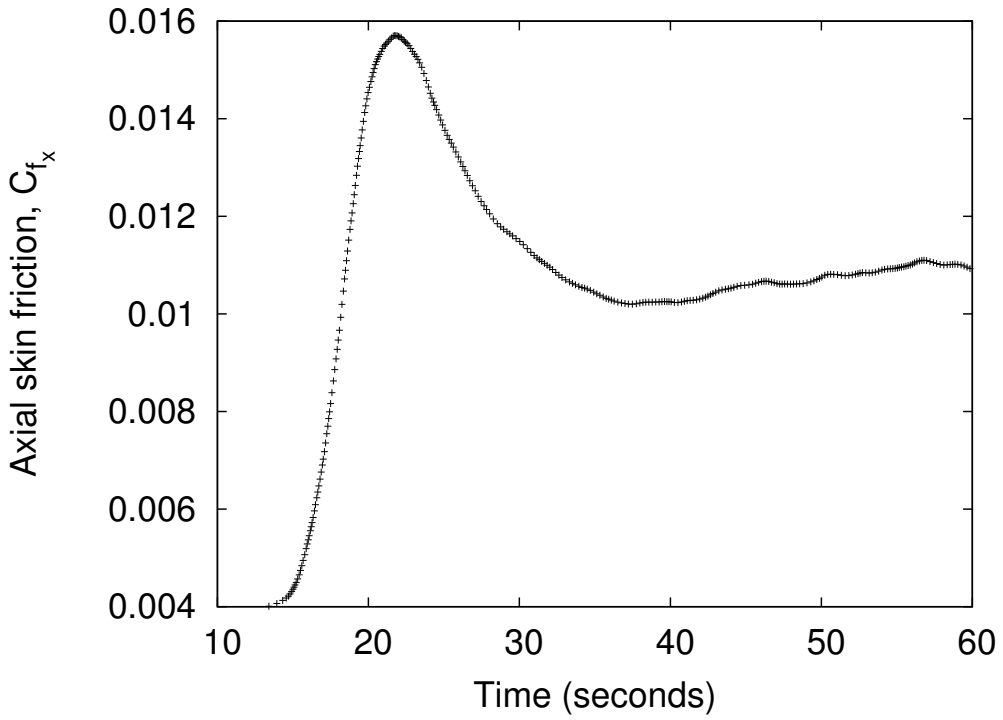

Figure 4.5: Axial skin friction coefficient for turbulent pipe preliminary inflow simulation.

Table 4.2: Parameters for charged liquid kerosene jet simulation employing fully turbulent inflow.

Parameter	Simulation	Experiment
N_{ei}	0.1	
Re	4900	
We	1700	
d_o/h	25	n/a
ρ_l/ρ_g	652	
μ_l/μ_g	56	
ϵ_r	2.2	
γ [N/m]	0.0235	

simulation may be due to the fully turbulent inflow, which appears to carry more turbulent kinetic energy and more flow disturbance than what is noticeable in the experiment shadowgraph, Fig. 4.6(a).

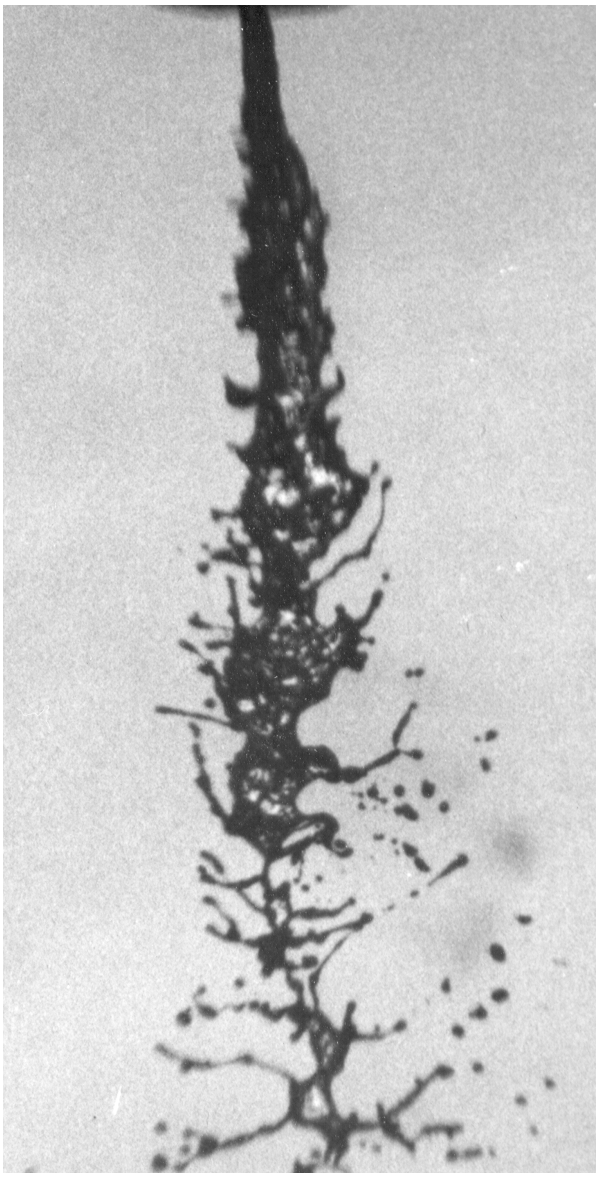

(a) Charge injection experiment, reproduced with permission [166].

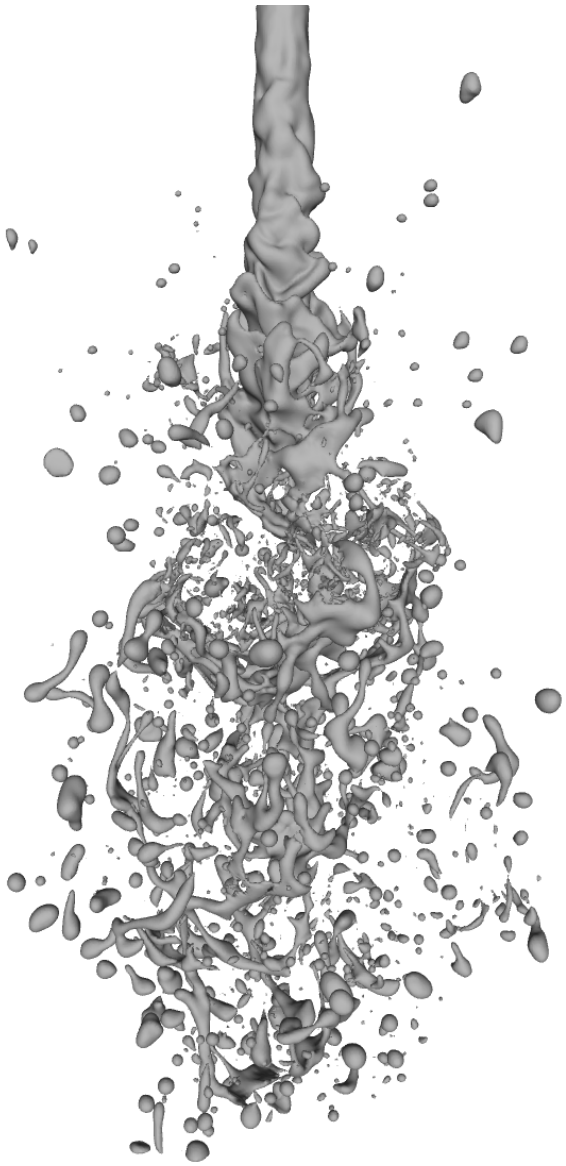

(b) Charged multiphase simulation using fully turbulent inflow.

Figure 4.6: Comparison of experiment and simulation of charged liquid kerosene jet with turbulent inflow.

There are several challenges to determining the correct hydrodynamic inflow conditions for the case of direct charge injection. One such challenge is the lack of detailed knowledge of the electrodynamics in the region within and immediately downstream of the charge injecting nozzle, including the local electric field and distribution of space charge. EHD-generated turbulence and highly complex electrochemical processes within the charge injecting nozzle further complicate this analysis. Finally, the numerical challenge of accurately simulating high-density-ratio, three-dimensional multiphase flows is poorly matched with most experimental work, which almost exclusively employ high density ratio tests. Given these challenges and the favorable results of the mesh alignment study in §4.3.1, the choice is made to employ a bulk inflow simulation with random disturbances as the hydrodynamic inlet to multiphase simulations in the initial series of electrically charged multiphase simulations.

4.4 Simulations of Electrically Charged Diesel-type Jets

This section discusses an initial set of detailed simulations of charged jets, Cases A0, A1, A2, and A3 summarized in Table 4.1 and described in greater detail in Table 4.3. The purpose of these simulations is to assess the fundamental physics and mechanisms of liquid break-up in charged Diesel-type jets, analyze statistics from the simulations, and propose simple models to predict the onset of atomization and drop size. Simulations employ a low density ratio, approximately $\rho_l/\rho_g \approx 50$. Lower density ratio simulations are relevant for many potential applications of this work, and simulations will not suffer from some of the challenging issues that currently plague higher density ratio simulations.

4.4.1 Global Description of the Flow

In this section, the global features of Case A0 - A4 are discussed in some detail, and qualitative observations are made about the nature of the liquid break-up mechanisms. Figure 4.7 captures the uncharged simulation after two flow-through times (FTTs). As expected the simulation shows no liquid breakup, even with the random disturbances introduced into

Table 4.3: Summary of proposed liquid jet EHD simulations. N_{tot} represents the total number of grid cells.

Parameter	Case A0	Case A1	Case A2	Case A3
N_{ei}	0	0.10	0.15	0.20
Re	2000			
We	1000			
d_o/h	25.6			
ρ_l/ρ_g	50			
μ_l/μ_g	50			
ϵ_r	2.2			
γ [N/m]	0.0235			
Domain: $30d \times 15d \times 15d$				
Mesh: $768 \times 384 \times 384$				
N_{tot}: 113 million				

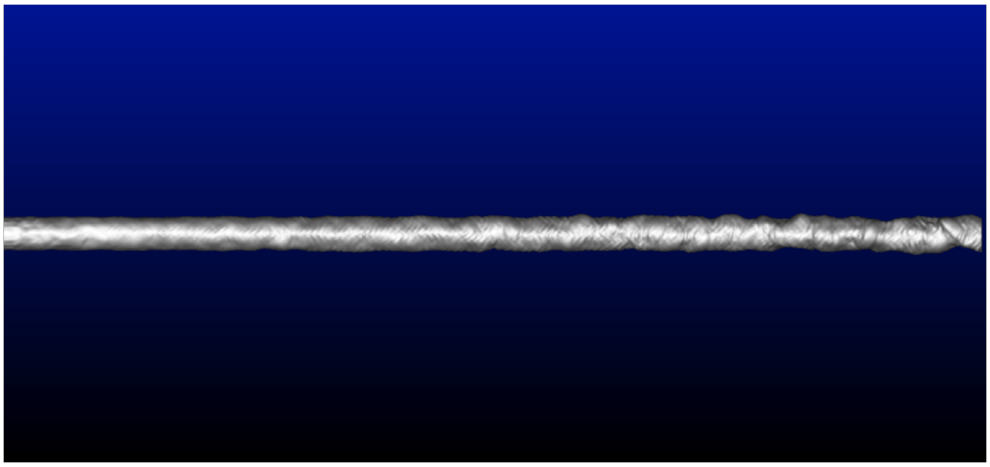

Figure 4.7: Instantaneous phase-interface location for Case A0, uncharged jet.

the bulk inflow. The lower density ratio used in this simulation accentuates the role of aerodynamic forces, however the low Reynolds number chosen for these simulations suppresses liquid breakup.

Figures 4.8(a)-4.8(c) present axial snapshots of the phase-interface for each of the three

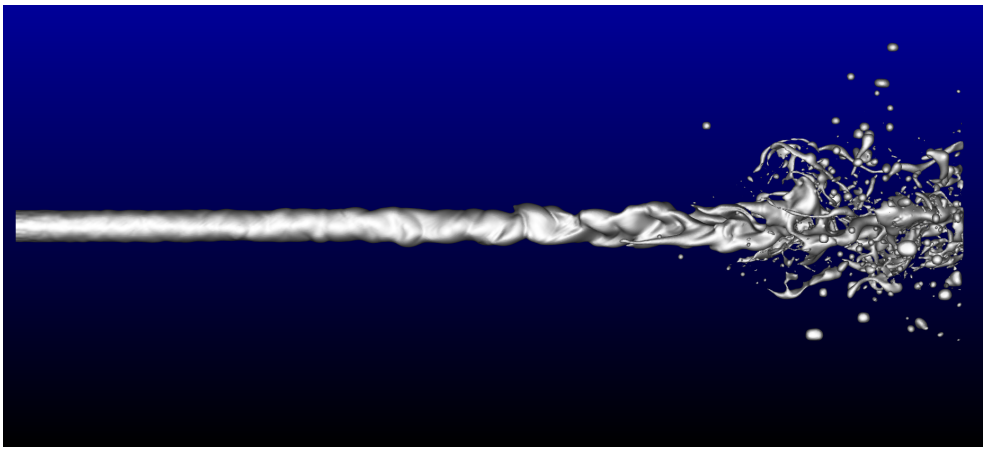

(a) $N_{ei} = 0.10$.

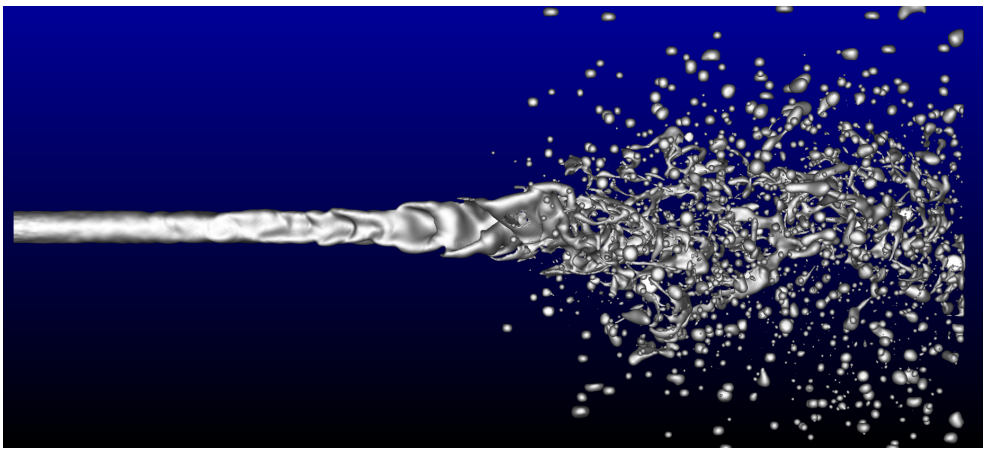

(b) $N_{ei} = 0.15$.

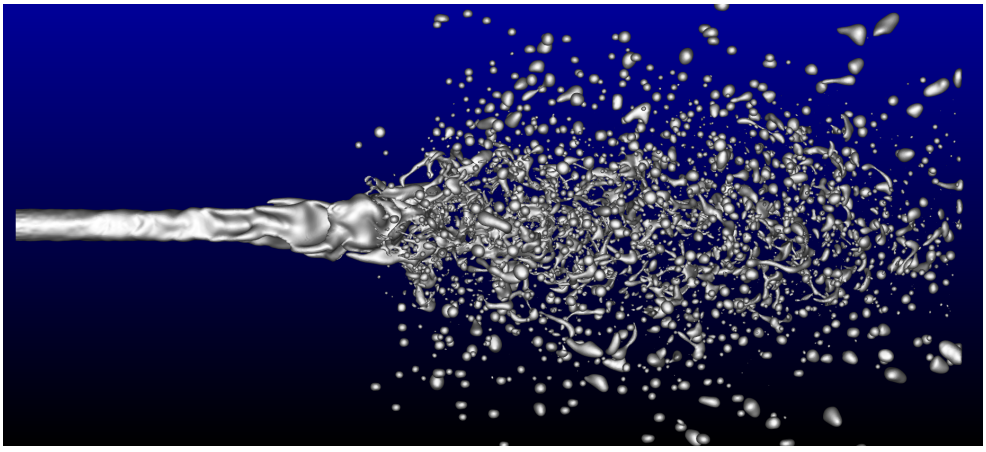

(c) $N_{ei} = 0.20$.

Figure 4.8: Instantaneous phase-interface location for electrically charged simulations, Cases A1-A3.

charged cases at approximately two FTTs. Immediately observable is the marked difference in the onset of atomization among Cases A1 - A3, with the axial point at which primary atomization begins, x_o, moving upstream as the electro-inertial number increases. For the $N_{ei} = 0.10$ case, liquid breakup begins at approximately $x_o \approx 19$. Figure 4.8(a) illustrates a number of long ligaments oriented in the $(-x)$ direction. The orientation arises from the lower density ratio, thereby enhancing the aerodynamic effects on the breakup process. This aerodynamically influenced orientation was observed in experimental work conducted by Wu and Faeith [199] for density ratios on the order of 100. The Coulomb force, oriented radially outward from the charged liquid core, is relatively small in this case, and therefore not expected to significantly alter the orientation of ligaments and structures. Nevertheless, the dispersion of drops and liquid structures from the core is noticeable near the $(x+)$ face, $x/D \geq 25$, even for this weakly charged simulation.

Case A2, shown in Figure 4.8(b), shows a primary atomization onset location significantly further upstream than in Case A1, consistent with the additional disruption and greater electric stresses accompanying higher levels of injected charge. Also, substantially more dislodged liquid structures exist in the domain in Case A2 as compared to Case A1, with a range of sizes, shapes and orientations. More structures with a radial orientation are present, attributable to the greater Coulomb force radial Coulombic repulsion. The domain is largely full of liquid structures at approximately $x/D \geq 20$, and several structures have reached the lateral extent of the domain. The spray cone angle is much wider than for Case A2.

Case A3, shown in Figure 4.8(c), illustrates significant atomization and complete disintegration of the liquid core in the latter half of the computational domain. The figure suggests that atomization begins at approximately $x_o \approx 15$, even further upstream than in Case A2, and the spray cone angle appears to be wider than both Cases A1 and A2. The radial distribution and orientation of structures is more pronounced than in Case A2, clearly illustrating the effects of increased charge and Coulombic repulsion. The higher level of

electric charge is also likely to instigate the rapid disintegration of the core, both through the Coulomb force and the greater electric stresses at the interface. The space charge electric field is greater for this case compared to Cases A1 and A2, and subsequently the EHD contribution to the pressure jump is greater. The combination of these two electric effects yield the rapid and full liquid breakup shown in Figure 4.8(c).

4.4.2 Statistical Results

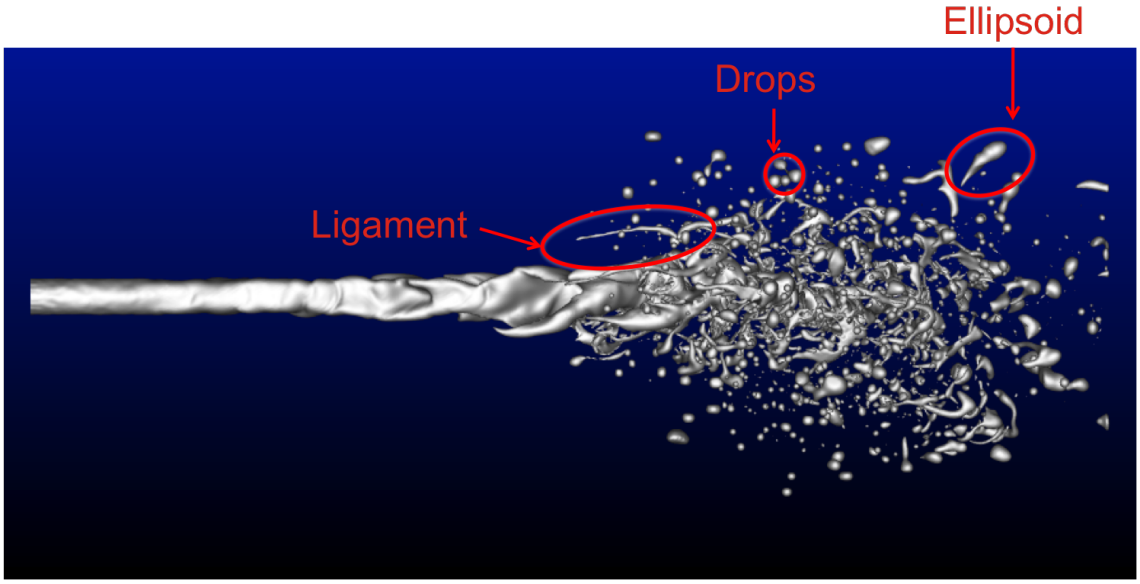

Figure 4.9: Depiction of three distinct structure types observed in simulations of electrically charged Diesel-type jets.

Statistics from simulation data are collected and analyzed for all structures within the domain. The statistics algorithm follows the methodology of Herrmann [76], with identification, synchronization across processors, computation of statistics for structure components, and a final global reduce for statistics for complete, contiguous structures. Statistics computed using this methodology in the NGA EHD module include:

- Structure volume,

- Structure radius, based upon spherical volume,
- Structure eccentricity, defined as $e = \max \frac{\|\boldsymbol{x}-\boldsymbol{x_d}\|}{\max(\Delta x, r_d)}$,
- Coordinates of structure volume-averaged center of gravity,
- Cartesian components of structure velocity (volume-averaged),
- Principal axis of orientation,
- Derived statistics: radial location and radial velocity.

Statistics permit classification of structures as *drops*, *ellipsoids*, or *ligaments*. The eccentricity statistic provides a convenient basis to classify structures. These three principal structure types are depicted in Figure and the distinction among the structure types can be summarized by their shape and expected behavior in the following manner:

- *Drops* are mostly spherical, with an eccentricity, $1 < e < 2$,
- *Ellipsoids* are elongated drops, with eccentricity in the range, $2 < e < 4$. For smaller ellipsoidal structures, surface tension forces will likely restore the structure to a spherical shape,
- *Ligaments* are very long, thin strucutres, typically having $e > 4$. Ligaments will generally neck and thin and subsequently break into multiple drop-like structures.

Additional details of the structure statistics algorithm are provided in Appendix B

Figures 4.10(a)-4.10(c) plot the radial location against axial position for all liquid structures in Cases A1 - A3, with dotted red lines annotating the axial point of atomization onset and an approximation of spray cone angle. The number and radial location of structures in these charts is similar to the instantaneous visualizations provided in Figures 4.8(a)-4.8(c). Similar characteristics and marked differences among the three cases are immediately noticeable in the statistical scatter plots of structure location, such as:

- The late onset of breakup and limited radial influence and orientation of structure location for the lowest charge case, A1;
- The point of atomization onset moving progressively upstream as the electro-inertial number increases;
- An increase in number of structures and "radial fullness" of liquid as electro-inertial number increases;
- A wider spray cone for Cases A2 and A3 compared to Case A1.

Onset of atomization and spray angle

Using the statistical results in Figures 4.10(a)-4.10(c), the axial point of atomization onset normalized by nozzle diameter, x_o/D, and spray cone angle, α, can be identified for each case and these results are summarized in Table 4.4. Clearly, the onset of atomization moves upstream as injected charge increases. Spray cone angle increases from Case A1 to A2, however no change is observed in the two cases with the highest electro-inertial numbers. Spray cone angle is likely limited by the domain size, as the instantaneous phase interface location in Figures 4.8(b) and 4.8(c) clearly show that liquid structures reach the lateral extent of the domain for both Cases A2 and A3.

Table 4.4: Onset of atomization and approximate spray cone angle for Cases A1 - A3.

Case	N_{ei}	x_o/D	α
A1	0.10	19.5	$\sim 50°$
A2	0.15	14.2	$\sim 75°$
A3	0.20	10.1	$\sim 75°$

As mentioned previously and supported by the phase-interface locations, Figures 4.8(a)-4.8(c), the number of liquid structures within the domain appears to increase with charge

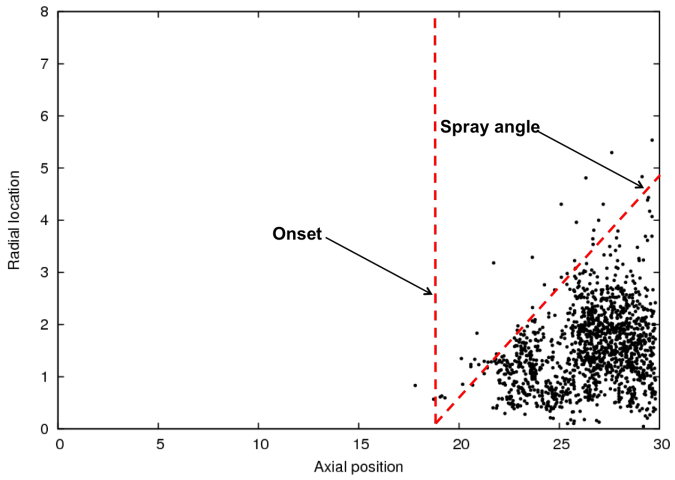

(a) Case A1: $N_{ei} = 0.10$

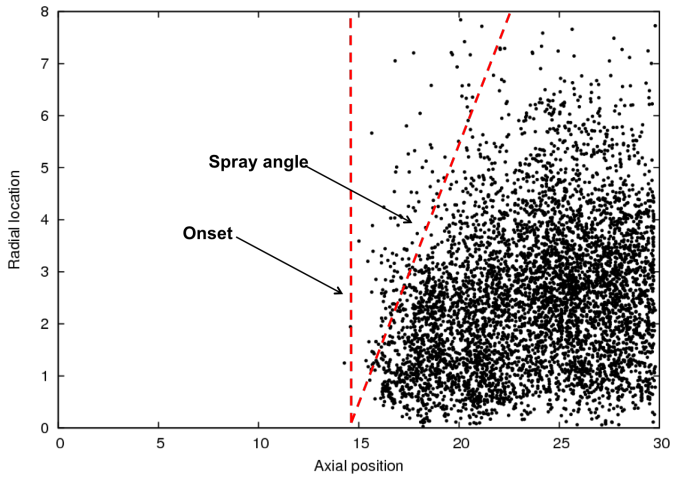

(b) Case A1: $N_{ei} = 0.15$

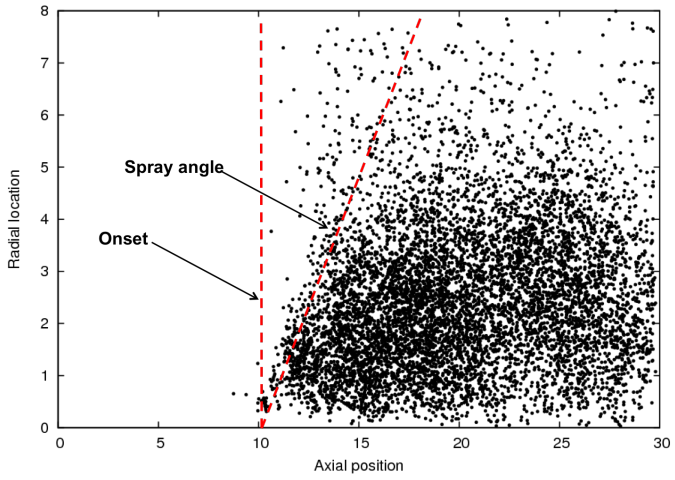

(c) Case A1: $N_{ei} = 0.20$

Figure 4.10: Plot of radial position versus axial location for Cases A1 - A3, with annotations for location of onset of atomization and approximation for spray cone angle.

level. Figure 4.11 confirms this observation, depicting a steady increase in total structures as well as ligaments, which are defined as having eccentricity, $e > 4$.

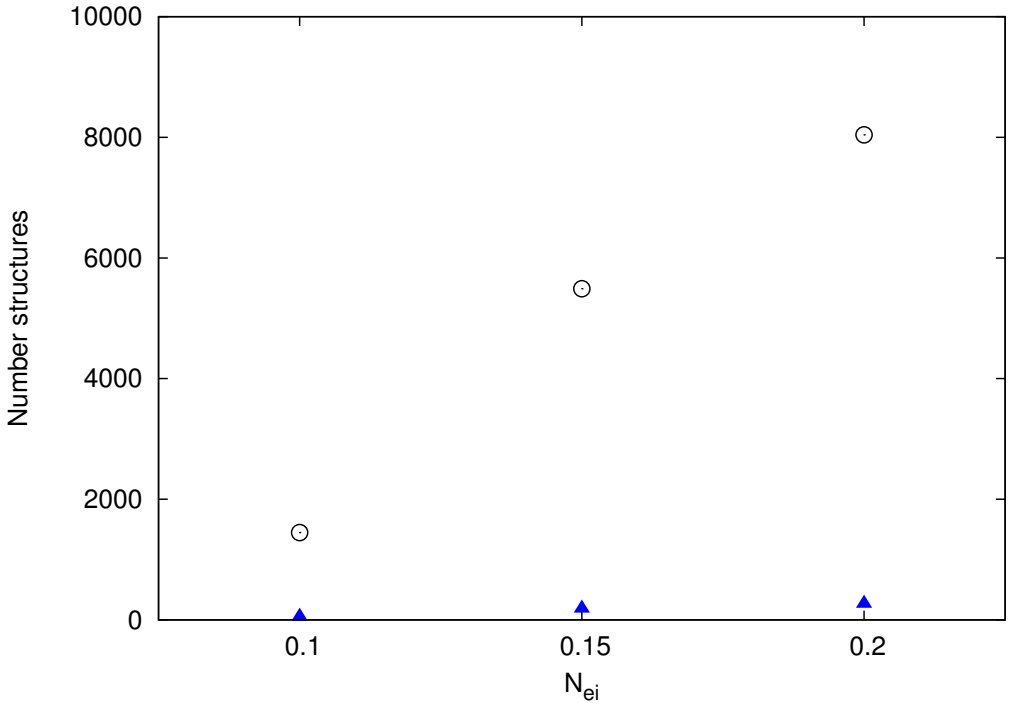

Figure 4.11: Number of total structures (unfilled circles) and ligament structures (blue triangles) for Cases A1 - A3.

Drop size distribution Drop size distribution suggests a reasonably good fit with log-normal distribution for a range of drop diameters, as depicted in Figure 4.12. Drop sizes smaller than this range are poorly resolved, suggesting mesh refinement is necessary. The drop diameter PDF illustrates a bi-modal distribution, with some preference for larger sized structures.

4.4.3 Modeling

This section strives to explain the interacting effects of electrostatics and hydrodynamics using simple scaling estimates for the dominant physical mechanisms. The methodology

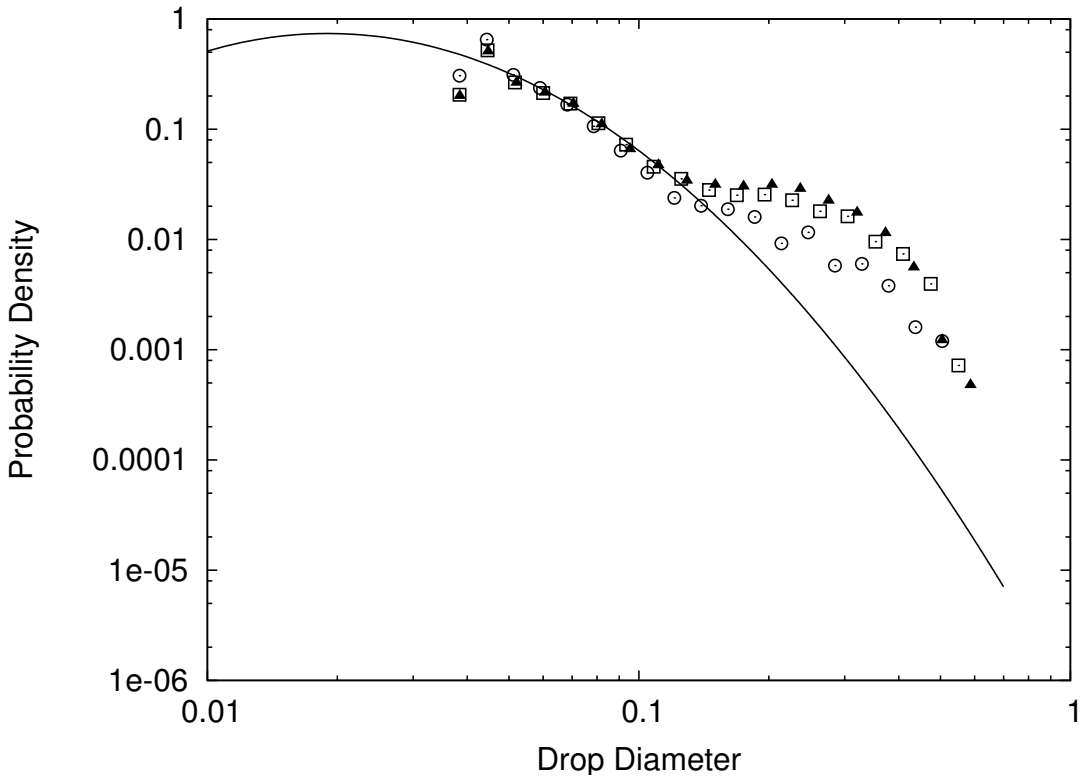

Figure 4.12: Drop size probability density function for Cases A2 (circles), A3 (squares), and A4 (triangles), and fitted log-normal distribution (line).

follows the analysis proposed by Wu and Faeith [199] and subsequently conducted by Desjardins and Pitsch [44].

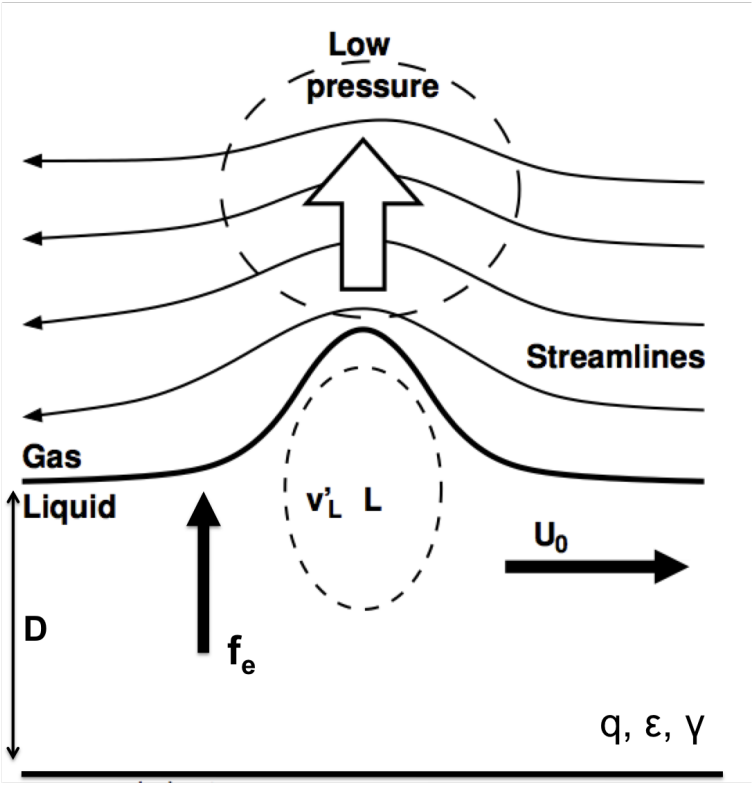

Figure 4.13: Schematic of the mechanisms leading to liquid breakup, including aerodynamic accentuation of breakup through lift effect.

A simple force balance in the radial direction is used to approximate the axial point at which liquid break-up begins. From qualitative observations, the radial orientation of liquid structures is attributable to Coulombic repulsion that arises from the space charge field, and is similar to that discussed elsewhere, for example in [180]. Coulombic repulsion leads to an electric field oriented radially from the liquid core. The Coulomb force is, therefore, a disruptive force that gives rise to the shape and orientation of the structures dislodged from the liquid core.Figure 4.13 illustrates the interacting forces for an initial deformation of the interface. In the figure, L is the deformation length scale, v'_L represents the local velocity of the deformation, D is the diameter of the liquid core, and liquid has previously

defined material properties of electric permittivity, ϵ, surface tension coefficient, γ, and bulk volumetric electric charge, q. Following the methodology employed by Wu and Faeth [199], a simple scaling of each principal force can be expressed per unit volume as:

- Coulomb force: $\boldsymbol{f_e} \sim q^2 D/\epsilon_l$
- Aerodynamic lift force: $\boldsymbol{f_L} \sim \rho_g U_o^2/L$
- Surface tension force: $\boldsymbol{f_{ST}} \sim \gamma/L^2$

It should be noted that this model neglects turbulent kinetic energy, assumed to be small for the Reynolds number employed in Cases A1 - A3.

Assuming that a radial velocity, $u_r(x)$, spatially varies in x only, one can write a simple force balance of aerodynamic, Coulomb, and surface tension forces, as

$$\rho_l \frac{du_r(x)}{dt} = \left(\frac{q^2 D}{\epsilon_l} + \rho_g u_o^2 - \frac{\gamma}{L^2}\right) \tag{4.4}$$

where $u_r(x)$ is one-dimensional radial velocity, u_o is the bulk velocity issuing from the nozzle. Assuming a time scale of $t \approx x/u_o$, where x is the axial location from the nozzle exit, allows to integrate with respect to time and obtain an expression for the radial distance as a function of the axial location, as

$$\rho_l \frac{dr(x)}{dt} = \left(\frac{q^2 D}{\epsilon_l} + \rho_g u_o^2 - \frac{\gamma}{L^2}\right)\frac{x}{u_o} \tag{4.5}$$

$$r(x) = \left(\frac{q^2 D}{\rho_l \epsilon_l} + \frac{\rho_g u_o^2}{\rho_l} - \frac{\gamma}{\rho_l L^2}\right)\frac{x^2}{u_o^2} \approx \frac{D}{2} \tag{4.6}$$

Solving for the axial location at which atomization begins normalized by the nozzle diameter, x_o/D, yields an expression including the electro-inertial number, N_{ei}, the density ratio, and the liquid Weber number, We_l

$$\frac{x_o}{D} = \left(\frac{2q^2 D^2}{\rho_l \epsilon_l u_o^2} + \frac{2D}{L_o}\frac{\rho_g}{\rho_l} - \frac{2\gamma}{\rho_l L^2 u_o^2}\right)^{-1/2} \tag{4.7}$$

$$\frac{x_o}{D} \propto \left(\mathrm{N}_{ei} + \frac{\rho_g}{\rho_l} - \mathrm{We}_l\right)^{-1/2} \tag{4.8}$$

$$\frac{x_o}{D} \approx \left(A\mathrm{N}_{ei} + B\frac{\rho_g}{\rho_l} - \frac{C}{\mathrm{We}_l}\right)^{-1/2} \tag{4.9}$$

where A, B, and C are coefficients.

As a first approximation, assume that aerodynamic effects are negligible. For Cases A2 - A4, the Weber number is constant, and therefore the axial location of the onset of atomization scales with $\mathrm{N}_{ei}^{-1/2}$, as

$$\frac{x_o}{D} \propto (\mathrm{N}_{ei})^{-1/2} \tag{4.10}$$

Figure 4.14 plots the axial point of atomization onset for Cases A2 - A4 and a line of $\mathrm{N}_{ei}^{-1/2}$ scaled to Case A2, showing reasonable agreement even for the simplification of negligible aerodynamic lift force effects.

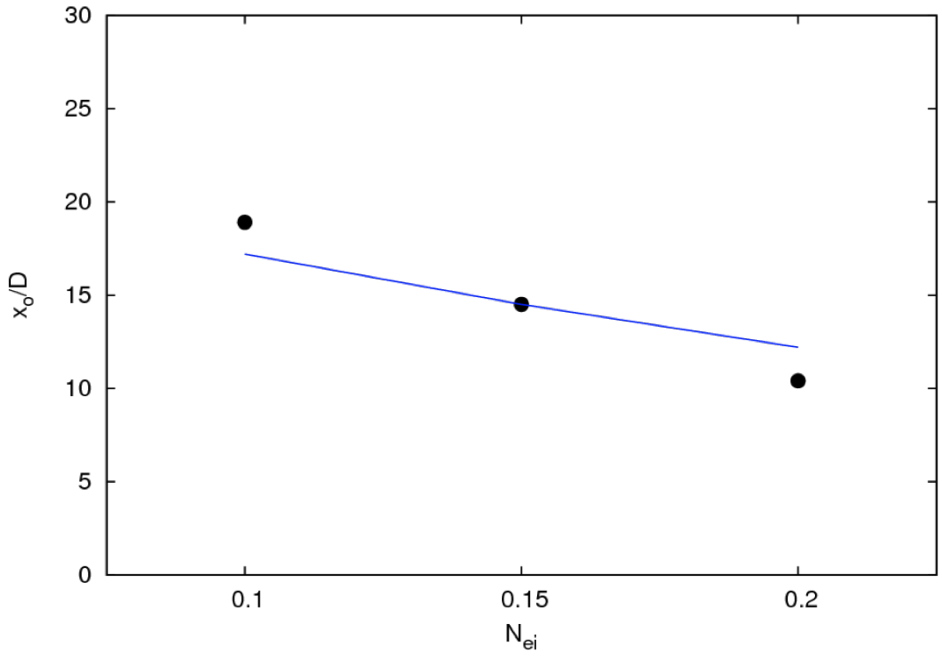

Figure 4.14: Plot of axial location of atomization onset for all three cases of electro-inertial number (filled circles) and scaled one-dimensional model predicting location of atomization onset (blue line)

4.5 Summary and Conclusions

This work strives to enhance the engineering community's understanding of the fundamental mechanisms of electrohydrodynamic-aided primary atomization of dielectric liquid

hydrocarbons through detailed numerical simulations. In the past decade, numerical techniques and computational resources have evolved rapidly, to the point that high-fidelity simulations of complex multiphysics, multiphase fluid flows can be conducted. This chapter extends recently developed numerical schemes based on first principles to perform fully three-dimensional direct numerical simulations of electrically charged liquid jets. The level set approach is combined with the ghost fluid method (GFM) to accurately simulate primary atomization phenomena for this class of flows. The numerical schemes are implemented within a conservative finite difference scheme of high-order accuracy that employs state-of-the-art interface transport techniques. A detailed numerical study of EHD atomization is conducted for a range of relevant dimensionless parameters for low density ratio test cases. Flow visualization is provided and qualitative, global characteristics of each simulation are discussed. An algorithm to identify liquid structures is implemented and used to collect statistics for all structures at different times in each simulations. Statistics are analyzed and spray characteristics, such as the onset of atomization, drop size distribution, and spray cone angle, are assessed. Finally, some simple models are proposed and compared with statistical results.

For simulations involving low density ratios, the effects of aerodynamic lift are enhanced, with the orientation of liquid structures deflected toward the upstream end of the computational domain. The aerodynamic effect is more pronounced for cases with lower electro-inertial numbers. This observation is congruent with observations reported in experimental work [199] and computational studies [44]. The axial location at which atomization commences moves progressively upstream as the electro-inertial number, and therefore the level of electrical charge, increases. The additional disruption of the Coulomb force, oriented radially outward from the liquid core and opposed by surface tension forces, as well as greater EHD surface stresses that accompany a higher space charge electric field both contribute to the upstream migration of the atomization onset point. Spray cone angle appears to increase with greater electro-inertial number, and this is confirmed for comparison among

the lowest-charged simulation and higher-charged simulations. However, visualization and statistical data suggest that the computational domain size limits conclusive remarks regarding spray angle for the higher-charged cases. Structures dislodged from the liquid core increase with greater electro-inertial number, consistent with increased Coulombic repulsion and electrical surface stresses. Drop size distribution suggests a reasonably good fit with log-normal distribution for a range of drop diameters. Drop sizes smaller than this range are poorly resolved, suggesting mesh refinement is necessary. The drop diameter PDF suggests a bi-modal distribution, with some preference for larger sized structures. Simple models for drop-size distribution and onset of atomization are derived using energy formulation and force balance methods, respectively, and account for inertial, surface tension, Coulombic, and aerodynamic effects. Statistical results for simulations show reasonable agreement with models, even in the one-dimensional formulations presented, and suggest that liquid Weber number, electro-inertial number, and density ratio are principal determinants of atomization onset location as well as drop size.

This chapter serves as a first step toward a much broader application of high-fidelity simulations for EHD flows. Continuation of this work will permit the development of a much-needed DNS database to support future efforts, both experimental and computational, within the engineering community. Additionally, the methodologies developed in Chapter 3 and validated in this work open new, simulations-based avenues of exploration within a broader category of electrohydrodynamics, including the colloquially-termed "electrosprays" and "Taylor cones" observed in electrostatic-aided spraying of semi-conducting liquids with much higher electrical conductivities.

Chapter 5

Conclusions and Perspectives

The complex, three-dimensional nature of electrohydrodynamic atomization of dielectric liquid hydrocarbon fuels has, for the first time, been explored in direct numerical simulation. Significant advances in computational methods have been made, combining the level set approach with the ghost fluid method (GFM) in three dimensions to model primary atomization for an electrically charged liquid hydrocarbon fuel. A high electric Reynolds number regime is assumed, and interface as well as bulk dynamics are modeled. The model is implemented within a conservative finite difference scheme of high-order accuracy that employs state-of-the-art interface transport techniques. This approach, validated using several cases with exact analytical solutions, demonstrates significant improvements in accuracy and efficiency compared to previous methods used for EHD modeling. The model is applied in direct numerical simulation of a charged and uncharged liquid Kerosene jet. Finally, a detailed numerical study of EHD atomization is conducted for a range of relevant dimensionless parameters to predict the onset of breakup, identify characteristic modes of liquid disintegration, and report elucidating statistics such as drop size and spray dispersion.

The methodologies developed and validated in this work open new, simulations-based avenues of exploration within a broader category of electrohydrodynamics. As identified in Chapter 2, the regions upstream (*e.g.* the injecting nozzle) and downstream (characterized by secondary atomization phenomena) represent topics of study that will improve upon this work and offer a comprehensive picture of EHD atomization for the engineering community.

Additionally, many engineering applications, such as colloid propulsion and inkjet printing, employ liquids classified as "semi-conducting" with much higher electrical conductivities. In such situations, the opposite regime of electric Reynolds number is dominant, whereby electric charge can be considered fully relaxed in a time scale much shorter than the governing hydrodynamic time scale (whether that be advection, viscous or capillary). While this class of EHD sprays has long been the subject of research, computational efforts have been limited to one- and two-dimensional axisymmetric models. The combination of NGA's state-of-the-art interface transport schemes with robust and accurate numerical methods for electrodynamics suggests a natural extension of this work to EHD sprays in the semi-conducting class. Some additional perspectives on the extension or continuation of this work are developed in the proceeding sections.

5.1 Multiple orifice, pulsed injection systems

Single orifice charge injection systems have been tested and proven beneficial by a number of investigators [85, 88, 97, 169, 170, 171, 204]. A few limitations of the single orifice, also called "point-plane," atomizer systems prevents broad use of these systems in combustion devices and applications. One particular drawback is a practical limit of fuel flow rate through the nozzle and the corresponding maximum volumetric charge that can be injected. Shrimpton and co-workers [90, 170, 171] have observed in experiments that the radial component of the electric field at the nozzle exit, given as

$$E_r = \frac{qd_o}{4\epsilon_r\epsilon_o}, \tag{5.1}$$

maintains an approximately constant maximum value, beyond which corona discharge occurs. The relationship between charge and nozzle diameter suggests that a smaller nozzle permits higher levels of injected charge. Nozzle diameter, though, is limited by manufacturing processes, practical considerations such as fouling and clogging, as well as the need for higher fuel flow rates with larger engines.

Considering the challenges of single orifice systems, multiple-orifice designs offer a practical alternative. Ongoing research at the University of Southampton investigates multiple orifice configurations, which improves flow rate limitations that continue to plague single orifice systems [90]. Simulating multiple orifice systems is a straightforward extension of the work described in this thesis, and computational efforts can be performed in parallel with ongoing experimental work performed by Nabity and Shrimpton, with the following proposed research objectives:

- Assess the effects of flow rate, level of electric charge, and hole pattern and geometry on spray characteristics.
- Evaluate the dynamics and interactions between sprays, including coallescence and charge transfer.
- Guide design and subsequent experimental work, and predict electric and hydrodynamic efficiencies for different designs.
- Predict spray patterns and quality for multiple orifice systems that employ advanced, time-varying "pulsed-injection" schemes.

5.2 Electrohydrodynamics within a charge-injecting nozzle

Charge injection atomizers operate by introducing electric charge into a highly insulating liquid hydrocarbon fuel. Charge injection systems have been demonstrated [85, 88, 97] and experimentally investigated [153, 154, 169, 170, 171, 177, 204]. The physical processes that yield charge in a dielectric liquid are believed to be electrochemical in nature and differ fundamentally from charging mechanisms in conducting liquids [19, 90]. In most practical configurations, the process entails a sharp-tipped metallic electrode housed in a nozzle body through which liquid fuel is flowed. A number of nozzle configurations have been tested [153, 154, 169, 170, 171, 204], and multiple orifice designs are currently the subject of

ongoing research [90].

Some limited work has been performed to understand the complicated physical mechanisms and electric-hydrodynamic interactions inside the charge injecting nozzle. Shrimpton [90, 165, 167] has conducted a two-dimensional computational study of this flow for one nozzle configuration using a Rayleigh-Benard analogy. The complexities of the coupled electric field, space charge distribution, momentum field, and a litany of relevant process mechanisms suggest that a high-fidelity, three-dimensional detailed numerical study is warranted. Some possible research objectives may include:

- Describe and visualize the hydrodynamic and electric fields.
- Assess the space charge distribution within the nozzle body and the nozzle exit plane, which may confirm the presence and proportion of relaxed surface charge on the liquid-gas interface at the nozzle exit.
- Assess the roles of convection and diffusion effects, as well as EHD turbulence [90].

5.3 Secondary atomization modeling

Beyond the region where the coherent liquid core begins to de-stabilize, depicted in Figure 5.1, secondary atomization phenomena become relevant. Secondary atomization is characterized by many "modes" of breakup, and one recent review provides some useful description of these modes [68]. One component that should be modeled in electrostatic-type sprays is evaporation. Efforts pursuing this end will be greatly facilitated by the numerical framework presented herein, as permits the use of a conservative variable density formulation, while preserving the simplicity of accounting for discontinuous variables by using GFM. The extension including phase-change will enable the investigation of more complex aspects of evaporation, such as multi-component evaporation, and will also enable validation of Lagrangian-based spray models.

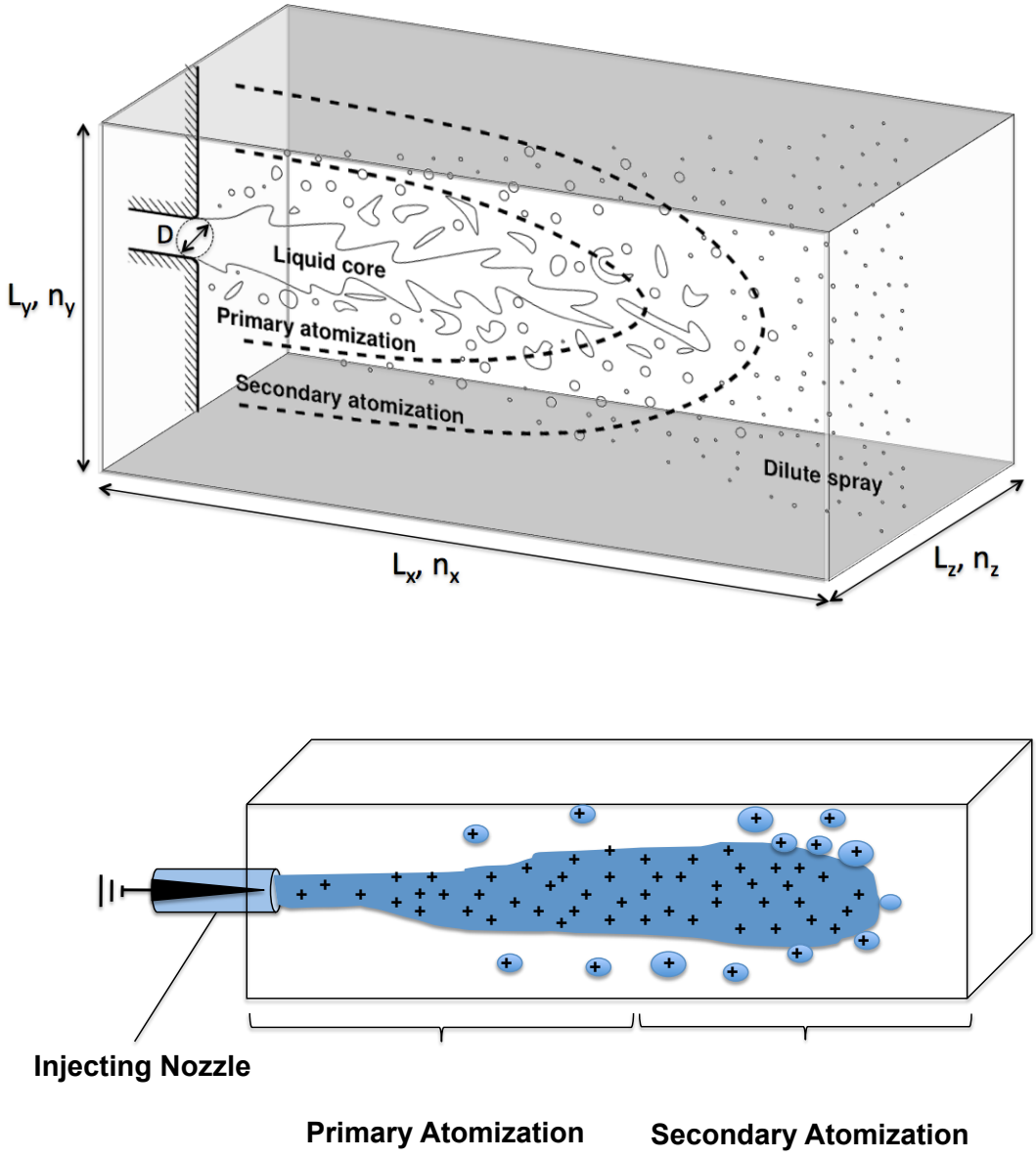

Figure 5.1: Sketch of primary and secondary atomization regions.

5.4 Modeling the low electric Reynolds number regime

The problem of electrostatic spraying in the range of "semi-insulating" to "semi-conducting" liquids, with electrical conductivities, $\sigma > 10^{-8}$ S/m, has been well-studied. The ability to control the spray and accelerate doplets has wide application in engineering, including micro-scale propulsion [124], inkjet printing [19, 83, 122], agriculture and spray-coating applications such as painting [3, 96]. A number of theoretical [158, 176, 183, 184], and computational studies [9, 10, 31, 56, 55] have been performed, with most employing two-dimensional axisymmetric assumptions. One of the most widely cited experimental investigations is that of Tang and Gomez [180], in which they combined flash shadowgraph technology for spray visualization, phase Doppler anemometry for drop size distribution, and one-dimensional analytical and semi-empirical models to validate results.

Given the high-fidelity, three-dimensional results reported in this thesis and related work with the NGA code [42, 48, 43, 47, 46], an extension of the methods detailed herein to the low electric Reynolds regime seems reasonable and worthy of investigation. Using a similar, yet diametric assumption to that discussed in §3.2, electric charge relaxation can be shown to occur at time scales much smaller than relevant hydrodynamic times scales, *e.g.* viscous, capillary, or advective. Thus, the governing equations introduced in Chapter 2 can be simplified to a negligible Coulomb force,

$$\boldsymbol{f}_e = 0, \tag{5.2}$$

in the absence of bulk, volumetric charge; solenoidal current density, described by

$$\nabla \cdot \boldsymbol{J} = 0; \tag{5.3}$$

and an electric potential that satisfies the Laplace equation vice the Poisson equation in the absence of bulk, native charge, as

$$\nabla^2 \phi = 0. \tag{5.4}$$

While the governing equations simplify in comparison to the modeling strategy discussed in this thesis, the boundary conditions become more complicated. The presence of a non-zero surface charge implies a discontinuity in the normal component of the electric displacement vector, as

$$\boldsymbol{n} \cdot [\boldsymbol{D}]_\Gamma = q_s, \tag{5.5}$$

and the tangential electric stresses at the surface balance viscous stresses so that

$$\left[\boldsymbol{n}^\mathsf{T} \cdot (\boldsymbol{\sigma}^f) \cdot \boldsymbol{t_i}\right]_\Gamma + q_s \boldsymbol{E} \cdot \boldsymbol{t_i} = 0. \tag{5.6}$$

Additionally, and perhaps most challenging, the surface current density, given as

$$[\boldsymbol{J} \cdot \boldsymbol{n}]_\Gamma + \nabla_s \cdot \boldsymbol{J_s} = (\boldsymbol{n} \cdot \boldsymbol{u})[q]_\Gamma - \frac{\partial q_s}{\partial t} - \boldsymbol{u_s} \cdot \nabla_s q_s + q_s \boldsymbol{n} \cdot (\boldsymbol{n} \cdot \nabla)\boldsymbol{u}. \tag{5.7}$$

cannot be wholly neglected, although some terms may be eliminated through an order of magnitude assessment.

To account for the tangential electric stresses, which play a substantial role in EHD systems dominated by interfacial dynamics, different numerical methods must be developed. The methods developed in this thesis assume that the normal component of the electric field is dominant, and the simplification of Liu *et. al* [102] is reasonable. For the low electric Reynolds number regime, the tangential smearing characteristic of this simplification will contribute to inaccuracies in the tangential stresses. Discontinuous Galerkin methods, integrated with the GFM in a compact stencil, should be considered to alleviate this tangential smearing while permitting an implementation that is true to all relevant interfacial boundary conditions.

Appendix A

General Formulation for Jump in Product of Multiple Factors

It is convenient to derive a general expression for the jump of the product of two or more material properties. This can generalized for the case of two factors as

$$\begin{aligned}
[a \cdot b]_\Gamma &= a_1 \cdot b_1 - a_2 \cdot b_2 \\
&= (a_1 \cdot b_1) - (a_2 \cdot b_2) + (a_1 \cdot b_2 - a_1 \cdot b_2) \\
&= (a_1 \cdot b_1) - (a_1 \cdot b_2) + (a_1 \cdot b_2) - (a_2 \cdot b_2) \\
&= a_1 \cdot (b_1 - b_2) + b_2 \cdot (a_1 - a_2) \\
&= a_1 \cdot [b]_\Gamma + b_2 \cdot [a]_\Gamma
\end{aligned} \tag{A.1}$$

The algebraic expansion is symmetric, thereby yielding:

$$[a \cdot b]_\Gamma = a_1 \cdot [b]_\Gamma + b_2 \cdot [a]_\Gamma = a_2 \cdot [b]_\Gamma + b_1 \cdot [a]_\Gamma \tag{A.2}$$

For the case of three factors, Eq A.1 can be extended to:

$$\begin{aligned}
[a \cdot b \cdot c]_\Gamma &= a_1 \cdot b_1 \cdot c_1 - a_2 \cdot b_2 \cdot c_2 \\
&= a_1 \cdot [b \cdot c]_\Gamma + b_2 \cdot c_2 \cdot [a]_\Gamma \\
&= a_1 \cdot (b_1 \cdot [c]_\Gamma + c_2 \cdot [b]_\Gamma) + b_2 \cdot c_2 \cdot [a]_\Gamma
\end{aligned} \tag{A.3}$$

Appendix B

Pseudo Code for Identifying, Synchronizing, and Computing Statistics for Liquid Structures

For the sake of completeness, the post-processing algorithms are summarized. The methodology outlined here follows the approach detailed in Herrmann [76]. In the first algorithm, linked lists with derived data structures are employed to identify the "corner" of an untagged liquid structure and subsequently "grow" the contiguous structure as efficiently as possible. Structure growth continues until the structure ends or the computational block boundary. The algorithm is summarized in Figure B.1, and the concept is depicted in Figure B.3.

In a parallelized computational scheme, many structures will extend beyond a single block or processor, and consequently must be joined across the processors. A synchronization algorithm is required to achieve this joining task. The algorithm employs the ghost nodes, regardless of scheme order, to compare structures across computational blocks. Employing a processor communication step, the identification tags on the interior border of the domain are copied onto the ghost cells of the adjacent processor block. If the ghost node tag value is lower than the interior border tag, the interior block tag is updated. The algorithm employs the global ID tag array described in Figure B.2 and the linked lists to efficiently synchronize identification tags for the same contiguous structure across multiple blocks. The concept is depicted in Figure B.4

Subsequent subroutines perform matching, merging and reduction of a list of unique

identification tags, and a global reduce operation for calculating statistics for contiguous drops, such as volume, approximate diameter, eccentricity, volume-averaged coordinates of center of mass, and volume-averaged components of structure velocity.

Data structure used for efficient linked list:

$drop\%id$ → drop unique ID
$drop\%nnode$ → number of nodes in structure
$drop\%node\%i,j,k$ → index of individual node belonging to current structure
$drop\%node\%S$ → **S** marking for node
$drop\%node\%C$ → **C** marking for node

```
begin
  idd_local = 1
  tag_offset = (nx * ny * nz)/(npx * npy * npz)
  idd = idd_local + tag_offset
  drop ⇒ first_drop                    // point linked list to head element
  for i = 1 to n_x do
    for j = 1 to n_y do
      for k = 1 to n_z do
        if G > 0 and id(i,j,k) = 0 then    // find first untagged node in the
        liquid
          id(i,j,k) = idd
          S(i,j,k) = 1                          // Mark node with S
          while drop%S(:) ≠ 0 do
            for l = 1 to dim do
              for m = 1 to dir do
                if G(ii,jj,kk) > 0, id(ii,jj,kk) ≠ 0 then
                  nnode = nnode + 1
                  call drop_resize
                  drop%node%C = 1
                  idd(ii,jj,kk) = idd
                end
              end
            end
            drop%node%S(:) = 0                  // zero the S nodes
            drop%node%S(:) = drop%node%C(:)  // update the S nodes
            drop%node%C(:) = 0                  // zero the C nodes
          end
          drop ⇒ drop%next      // allocate next linked list element
          idd = idd + 1
        end
      end
    end
  end
  nullify(drop%next)      // found all structures, set appropriate pointer
end
```

Figure B.1: Multi-block algorithm to identify and tag structures

```
begin
    global_stop = 1
    counter = 0
    while global_stop = 1 do
        call boundary_update_border_integer

        // Begin marching along interior border, begin at i_min

        for j = 1 to n_y do
            for k = 1 to n_z do
                if idd(i_min − 1, j, k) > 0, idd(i_min, j, k) > idd(i_min − 1, j, k)) then
                // check ID tags of ghost and border nodes
                    idd(i_min, j, k) = idd(i_min − 1, j, k)
                    drop ⇒ first_drop
                    while associated(drop%next) do
                        if drop%id = idd(i_min, j, k) then
                            drop%id = idd(i_min − 1, j, k)
                            stop = 1
                        end
                    end
                end
            end
        end
    end

    // repeat for i_max, j_min, j_max, k_min, k_max

    call parallel_max(stop, global_stop)
end
```

Figure B.2: Multi-block algorithm to synchronize ID tags for the same structure across multiple processors

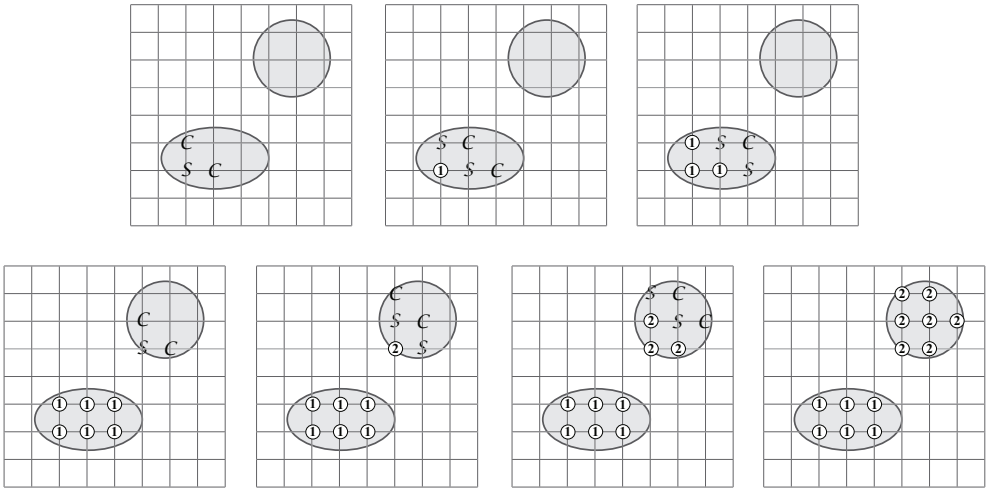

Figure B.3: Basic, single-block structure "growth" algorithm, showing nodes which are identified as "candidates", ***C*** and nodes that are "'confirmed", ***S***. Figure, from [76], used with permission

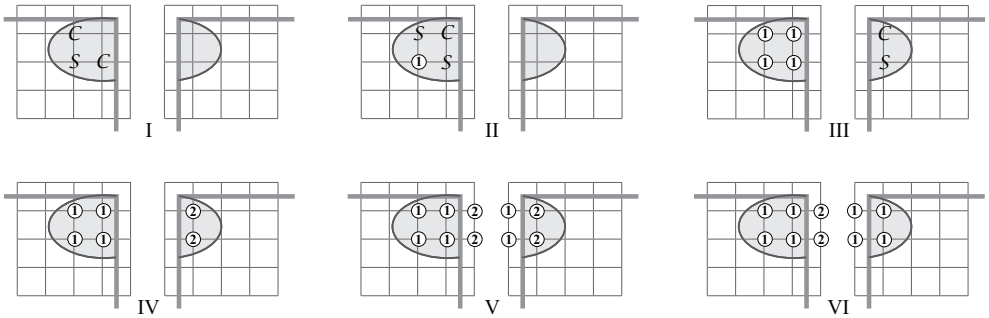

Figure B.4: Drop synchronization schematic, showing second step in synchronizing identification tags for components of structures across processor blocks. Figure used with permission from [76]

Bibliography

[1] Environmental impacts of newly regulated nonroad engines. Technical report, US Environmental Protection Agency, Feb 2002.

[2] R Allan and S Mason. Particle behaviour in shear and electric fields. i. deformation and burst of fluid drops. Proceedings of the Royal Society of London. Series A, Jan 1962.

[3] Adrian G. Bailey. Electrostatic spraying of liquids. Jan 1988.

[4] W Balachandran and W Machowski. Electrohydrodynamic atomization of insulating liquids. Electrical Insulation and Dielectric Phenomena, Jan 1998.

[5] W BALACHANDRAN, W MACHOWSKI, M Halimic, and C Wilson. Space charge modeling in a charge injected electrostatic atomiser. Proceedings of the 1998 IEEE Industry Applications Conference, 1998.

[6] W Balachandran, W Machowski, and Z Huneiti. Advances in electrohydrodynamic atomization of liquids. Atomization, Jan 1999.

[7] H Barnett and R Hibbard. Basic Considerations in the Combustion of Hydrocarbon Fuels with Air. National Advisory Committee for Aeronautics, Jan 1957.

[8] A Barrero, AM Ganan-Calvo, J Davila, A Palacio, and E Gomez-Gonzalez. Low and high reynolds number flows inside taylor cones. J. Fluid Mech Phys Rev E, 58:7309, 1992.

[9] O Basaran. Axisymmetric shapes and stability of pendant and sessile drops in an electric field. Journal of Colloid and Interface Science, 140(1):10–30, Nov 1990.

[10] JC Baygents, NJ Rivette, and HA Stone. Electrohydrodynamic deformation and interaction of drop pairs. J. Fluid Mech., 368:359–375, 1998.

[11] J Benajes, S Molina, K De Rudder, D Maroteaux, and H Hamouda. The use of micro-orifice nozzles and swirl in a small hsdi engine operating at a late split-injection ltc regime. Proceedings of the Institution of Mechanical Engineers, Part D: Journal of Automobile Engineering, 220(12):1807–1817, Jan 2006.

[12] D Benson. Computational methods in lagrangian and eulerian hydrocodes. Computer methods in applied mechanics and engineering, pages 1–160, Sep 1992.

[13] Erik Bjorklund. The level-set method applied to droplet dynamics in the presence of an electric field. Computers and Fluids, 38(2):358–369, Jan 2008.

[14] T Bourouina and J Grandchamp. Modeling micropumps with electrical equivalent networks. J. Micromech. Microeng., Jan 1996.

[15] J Brackbill, D Kothe, and C Zemach. A continuum method for modeling surface tension. Journal of Computational Physics, 100(2), Jun 1992.

[16] N Bremond, C Clanet, and E Villermaux. Atomization of undulating liquid sheets. J. Fluid Mech., 585:421–456, 2007.

[17] J Carretero and M Martínez-Sánchez. Numerical simulation of a colloidal thruster in the droplet regime. Computer Physics Communications, 164(1-3):202–208, 2004.

[18] A Castellanos. Coulomb-driven convection in electrohydrodynamics. IEEE Transactions on Electrical Insulation, 26(6):1201–1215, 1991.

[19] Antonio Castellanos. Electrohydrodynamics. Springer, Jan 1998.

[20] Texas Advanced Computing Center. Ranger User Guide, Feb 2009.

[21] J. Chang, Arnold J. Kelly, and Joseph M. Crowley. Handbook of electrostatic processes. Marcel Dekker, Inc., Jan 1995.

[22] H Cheng. Ejection interaction of two adjacent micropumps. ASME Journal of Fluids Engineering, pages 1–9, Jul 2006.

[23] HP Cheng and CP Chien. Ejection characteristics of micropumps for motorcycle fuel atomizer in high-temperature environment. Applied Thermal Engineering, 28(2-3):94–109, 2008.

[24] KJ Cheng and JB Chaddock. Deformation and stability of drops and bubbles in an electric field. Physics Letters A, 106:51–53, 1984.

[25] R Chicon, A Castellanos, and E Martin. Charge density distribution in electrohydrodynamics of insulatingliquids. Electrical Insulation and Dielectric Phenomena, 1997. IEEE 1997 Annual Report., Conference on, 2, 1997.

[26] JP Cocchi and R Saurel. A riemann problem based method for the resolution of compressible multimaterial flows. Journal of Computational Physics, 137(2):265–298, 1997.

[27] B Cockburn, S Hou, and CW Shu. The Runge-Kutta local projection discontinuous Galerkin finite element method for conservation laws. IV: The multidimensional case. Mathematics of Computation, pages 545–581, 1990.

[28] B Cockburn, SY Lin, and CW Shu. TVB Runge-Kutta local projection discontinuous Galerkin finite element method for conservation laws III: one-dimensional systems. J. Comput. Phys, 84(1):90–113, 1989.

[29] B Cockburn and CW Shu. TVB Runge-Kutta local projection discontinuous Galerkin finite element method for conservation laws II: general framework. Mathematics of Computation, pages 411–435, 1989.

[30] B Cockburn and CW Shu. The Runge-Kutta discontinuous Galerkin method for conservation laws V multidimensional systems. Journal of Computational Physics, 141(2):199–224, 1998.

[31] Robert T Collins, Michael T Harris, and Osman A Basaran. Breakup of electrified jets. J. Fluid Mech., 588, Oct 2007.

[32] JM Crowley. Electrohydrodynamic droplet generators. J. Electrostatics, 14:121–134, 1983.

[33] JM Crowley. Fundamentals of applied electrostatics. Laplacian Press, 1986.

[34] A Denat, B Gosse, and J Gosse. Ion injections in hydrocarbons. Journal of Electrostatics, 7:205–225, Aug 1979.

[35] A Denat, B Gosse, and J Gosse. High field dc and ac conductivity of electrolyte solutions in hydrocarbons. Journal of Electrostatics, 11(3):179–194, Feb 1982.

[36] A Denat, JP Gosse, and B Gosse. Electrical conduction of purified cyclohexane in a divergent electric field. IEEE Transactions on Electrical Insulation, 23(4):545–554, 1988.

[37] J.E. Dendy. Black box multigrid. Journal of Computational Physics, 48:366–386, 1982.

[38] O. Desjardins, G. Blanquart, G. Balarac, and H. Pitsch. High order conservative finite difference scheme for variable density low mach number turbulent flows. Journal of Computational Physics, 227(15):7125–7159, 2008.

[39] O. Desjardins, R.O. Fox, and P. Villedieu. A quadrature-based moment method for dilute fluid-particle flows. Journal of Computational Physics, 227(4):2514–2539, 2008.

[40] O. Desjardins and V. Moureau. Towards robust numerical simulation of air-blast atomization with high density ratios. In 61st Annual Meeting of the APS Division of Fluid Dynamics, November 23-25, 2008, Jan 2008.

[41] O. Desjardins, V. Moureau, E. Knudsen, and M. Herrmann. Numerical simulation of the primary atomization of a turbulent coaxial liquid jet using a conservative level set/ghost fluid method. American Physical Society, Jan 2006.

[42] O. Desjardins, V. Moureau, and H. Pitsch. An accurate conservative level set/ghost fluid method for simulating turbulent atomization. Journal of Computational Physics, 227, Jan 2008.

[43] O. Desjardins and H. Pitsch. A spectrally refined interface approach for simulating multiphase flows. Journal of Computational Physics, 228(5):1658–1677, Mar 2009.

[44] O Desjardins and H Pitsch. Detailed numerical investigation of turbulent atomization of liquid jets. Journal of Atomization and Sprays, 20(4):311–336, May 2010.

[45] O. Desjardins, V. Raman, S. Apte, and H. Pitsch. Sub-filter models for large eddy simulation of particle-laden flows. American Physical Society, Jan 2004.

[46] Olivier Desjardins. Adaptive spectral refinement for accurate simulations of turbulent multiphase flows. In ICLASS 2009, Vail, Colorado, July, 2009, Aug.

[47] Olivier Desjardins. Detailed numerical investigation of turbulent atomization of liquid jets. In ICLASS 2009, Vail, Colorado, July, 2009, August.

[48] Olivier Desjardins. Numerical Methods for Liquid Atomization and Application in Detailed Simulations of a Diesel Jet. PhD thesis, Jun 2008.

[49] T Edwards, W.E Harrison, and L.Q Maurice. Properties and usage of air force fuel: Jp-8. 39th AIAA Aerospace Sciences Meeting and Exhibit, January 8 - 11, 2001, Reno, NV, pages 1–12, Jan 2001.

[50] B Fan, G Song, and F Hussain. Simulation of a piezoelectrically actuated valveless micropump. Smart Mater. Struct., 14(2):400–405, Mar 2005.

[51] O Fawehinmi, P Gaskell, P Jimack, N Kapur, and H Thompson. A combined experimental and computational fluid dynamics analysis of the dynamics of drop formation. Proceedings of the Institution of Mechanical Engineers, Part C: Journal of Mechanical Engineering Science, 219(9):933–947, Apr 2005.

[52] R.P. Fedkiw, T. Aslam, B. Merriman, and S. Osher. A non-oscillatory eulerian approach to interfaces in multimaterial flows (the ghost fluid method). Journal of Computational Physics, 152(2):457–492, 1999.

[53] N Felici. Conduction and electrification in dielectric liquids: two related phenomena of the same electrochemical nature. J. Electrostatics, 15:291–297, 1984.

[54] N Felici and R Tobazeon. Charge carrier elimination and production by electrodialytic polymers in contact with dielectric liquids. Journal of Electrostatics, 11(2):135–161, Sep 1981.

[55] J Feng and T Scott. A computational analysis of electrohydrodynamics of a leaky dielectric drop in an electric field. J. Fluid Mech, 311:289–326, Jan 1996.

[56] JQ Feng. Electrohydrodynamic behaviour of a drop subjected to a steady uniform electric field at finite electric reynolds number. Proceedings: Mathematical, Physical and Engineering Sciences, 455(1986):2245–2269, 1999.

[57] Joel H. Ferziger. Numerical Methods for Engineering Applications. John Wiley and Sons, Inc., 1998.

[58] Joel H. Ferziger and Milovan Perić. Computational methods for fluid dynamics. Springer, 1996.

[59] R Fox, O Desjardins, P Villedieu, and H Pitsch. Eulerian models for dilute sprays using quadrature methods. American Physical Society, Jan 2006.

[60] A Gamboa, C Morrs, and F Forster. Improvements in fixed-valve micropump performance through shape optimization of valves. ASME Journal of Fluids Engineering, pages 1–8, Apr 2005.

[61] Manuel Gamero-Castaño. The structure of electrospray beams in vacuum. J. Fluid Mech., 604:1–30, Jun 2008.

[62] Alfonso M Gañán-Calvo, José M López-Herrera, and Pascual Riesco-Chueca. The combination of electrospray and flow focusing. J. Fluid Mech., 566:421, Nov 2006.

[63] A Geipel, A Doll, P Jantscheff, N Esser, U Massing, P Woias, and F Goldschmidtboeing. A novel two-stage backpressure-independent micropump: modeling and characterization. J. Micromech. Microeng., 17(5):949–959, Apr 2007.

[64] Gogosov, V Polyanskii, and I Semenova. Ehd flows at large electric reynolds numbers. Journal of Applied Mechanics and Technical Physics, Jan 1969.

[65] M Gorokhovski and M Herrmann. Modeling primary atomization. Annual Review of Fluid Mechanics, 2008.

[66] Ronald L Grimm. Fundamental studies of the mechanisms and applications of field-induced droplet ionization mass spectrometry and electrospray mass spectrometry. Technical report, Oct 2005.

[67] Sergey I Gubarenko, Paul Chiarot, Ridha Ben Mrad, and Pierre E Sullivan. Plane model of fluid interface rupture in an electric field. Phys. Fluids, 20(4):043601, Jan 2008.

[68] D. R Guildenbecher, C Lopez-Rivera, and P. E Sojka. Secondary atomization. Experiments in Fluids, 46(3):371–402, January 2009.

[69] Dan Guildenbecher. Secondary Atomization of Electrostatically Charged Drops. PhD thesis, Purdue University, Jul 2009.

[70] M Haidara and A Denat. Electron multiplication in liquid cyclohexane and propane: an estimation of the ionization coefficient. Conduction and Breakdown in Dielectric Liquids, 1990. ICDL 1990. Conference Record., 10th International Conference on, pages 397 – 401, Aug 1990.

[71] Bret Halpern. Field emission in liquids. J. Chem. Phys., 51(3):1031, Jan 1969.

[72] Bret Halpern. Field ionization in liquids. J. Chem. Phys., 51(3):1048, Jan 1969.

[73] Hermann A. Haus and James R. Melcher. Electromagnetic fields and energy. Prentice-Hall, 1989.

[74] M Takada S Yonesige K Nagoka M Hayakawa and D Takeda. Fuel spray simulation of slit nozzle injector for direct-injection gasoline engine. Society of Automotive Engineers, pages 1–8, Oct 2002.

[75] M Herrmann. A balanced force refined level set grid method for two-phase flows on unstructured flow solver grids. Journal of Computational Physics, 227(4):2674–2706, 2008.

[76] M Herrmann. A parallel eulerian interface tracking/lagrangian point particle multiscale coupling procedure. Journal of Computational Physics, 229(3):745–759, Jan 2010.

[77] C.W Hirt and B.D Nichols. Volume of fluid (vof) method for the dynamics of free boundaries. Journal of Computational Physics, 39:201–225, Dec 1981.

[78] D Horning. A study of the high-temperature autoignition and thermal decomposition of hydrocarbons. Report No. TSD-135, Standord University, Jun 2001.

[79] X Huang and TK Chuan. Mems-micropumps: A review.

[80] L Pease III and W Russel. Electrostatically induced submicron patterning of thin perfect and leaky dielectric films: A generalized linear stability analysis. J. Chem. Phys., Jan 2003.

[81] John David Jackson. Classical Electrodynamics. John Wiley and Sons, Inc., 1999.

[82] A Jaworek and AT Sobczyk. Electrospraying route to nanotechnology: An overview. Journal of Electrostatics, 66(3-4):197–219, 2008.

[83] S Kamisuki, T Hagata, C Tezuka, Y Nose, and M Fujii. A low power, small, electrostatically-driven commercial inkjet head. Micro Electro Mechanical Systems, Jan 1998.

[84] A.J Kelly. Electrostatic metallic spray theory. Journal of Applied Physics, 47(12), Dec 1976.

[85] AJ Kelly. The electrostatic atomization of hydrocarbons. J. Inst. Energy, 1984.

[86] A.J. Kelly. Charge injection electrostatic atomizer modeling. Aerosol Sci Tech, 12(3):526–537, Jan 1990.

[87] A.J Kelly. On the statistical, quantum and practical mechanics of electrostatic atomization. Journal of Aerosol Science, 25(6), Mar 1994.

[88] K Kim and R Turnbull. Generation of charged drops on insulating liquids by electrostatic spraying. Journal of Applied Physics, 47(5), May 1976.

[89] E Knudsen and H Pitsch. A general flamelet transformation useful for distinguishing between premixed and non-premixed modes of combustion. Combustion and Flame, 156(3):678–696, 2009.

[90] A Kourmatzis and J S Shrimpton. Electrohydrodynamics and charge injection atomizers: A review of the governing equations and turbulence. Journal of Atomization and Sprays, 19:1045–1063, Dec 2009.

[91] G Krishnan, J Daily, and J Nabity. Simulation of an electrostatically driven microinjector. Journal of Propulsion and Power, Jan 2007.

[92] R Lagumbay. Modeling and Simulation of Multiphase/multicomponent Flows. PhD thesis, Jan 2006.

[93] Lev Davidovich Landau and E M Lifshitz. Electrodynamics of Continuous Media. Pergamon, Oxford, 1975.

[94] Chun Lang. Numerical investigation of liquid jet emanating from plain-orifice atomizers with chamfered or rounded orifice inlets. JSME International Journal, 47:1–11, Mar 2004.

[95] D J Laser and J G Santiago. A review of micropumps. J. Micromech. Microeng., 14(6):R35–R64, Apr 2004.

[96] A Lefebvre. Atomization and sprays. CRC Press, Jan 1989.

[97] W. Lehr and W. Hiller. Electrostatic atomization of liquid hydrocarbons. Journal of Electrostatics, 30:433–440, May 1993.

[98] J Li, YY Renardy, and M Renardy. Numerical simulation of breakup of a viscous drop in simple shear flow through a volume-of-fluid method. Phys. Fluids, 12:269, 2000.

[99] R.D Reitz S.P. Lin. Drop and spray formation from a liquid jet. Annual Review of Fluid Mechanics, 30:1–22, Aug 1998.

[100] MA Linne, M Paciaroni, E Berrocal, and D Sedarsky. Ballistic imaging of liquid breakup processes in dense sprays. Proceedings of the Combustion Institute, 32(2):2147–2161, 2009.

[101] X Liu, S Osher, and T Chan. Weighted essentially non-oscillatory schemes. Journal of Computational Physics, Jan 1994.

[102] XD Liu, RP Fedkiw, and M Kang. A boundary condition capturing method for poisson's equation on irregular domains. Journal of Computational Physics, 160(1):151–178, 2000.

[103] D Lorstad, M Francois, W Shyy, and L Fuchs. Assessment of volume of fluid and immersed boundary methods for droplet computations. International Journal for Numerical Methods in Fluids, 46(2), 2004.

[104] H Luo, JD Baum, and R Löhner. A discontinuous galerkin method based on a taylor basis for the compressible flows on arbitrary grids. Journal of Computational Physics, 2008.

[105] SP MacLachlan and CW Oosterlee. Algebraic multigrid solvers for complex-valued matrices. SIAM Journal on Scientific Computing, 30(3):1548–1571, 2008.

[106] E Marchandise, P Geuzaine, N Chevaugeon, and J Remacle. A stabilized finite element method using a discontinuous level set approach for the computation of bubble dynamics. Journal of Computational Physics, 225(1):949–974, Jul 2007.

[107] P Marmottant and E Villermaux. On spray formation. J. Fluid Mech., 498:73–111, Jan 2004.

[108] Phillippe Marmottant. Atomisation d'un Liquide par un Courant Gazeux. PhD thesis, Institut National Polytechnique De Grenoble, Feb 2002.

[109] J Melcher and C Smith. Electrohydrodynamic charge relaxation and interfacial perpendicular-field instability. Phys. Fluids, Jan 1969.

[110] J Melcher and G Taylor. Electrohydrodynamics: a review of the role of interfacial shear stresses. Annual Review of Fluid Mechanics, 1(111-146), Jan 1969.

[111] James R. Melcher. Continuum Electromechanics. MIT Press, 1981.

[112] JR Melcher. Charge relaxation on a moving liquid interface. Phys. Fluids, 10(2), 1967.

[113] R.A Millikan. On the elementary electrical charge and the avogadro constant. The Physical Review, Series II, 2(1):109–143, Apr 1913.

[114] R Mittal and G Iaccarino. Immersed boundary methods. 2005.

[115] Y. Morinishi, T.S. Lund, O.V. Vasilyev, and P. Moin. Fully conservative higher order finite difference schemes for incompressible flow. Journal of Computational Physics, 143(1):90–124, 1998.

[116] Y. Morinishi, O.V. Vasilyev, and T. Ogi. Fully conservative finite difference scheme in cylindrical coordinates for incompressible flow simulations. Journal of Computational Physics, 197(2):686–710, 2004.

[117] CJ Morris and FK Forster. Low-order modeling of resonance for fixed-valve micropumps based on first principles. Microelectromechanical Systems, Journal of, 12(3):325–334, 2003.

[118] J Nabity and J Daily. A mems fuel atomizer for advanced engines. AIAA CANEUS Conference, pages 1–9, Nov 2004.

[119] J Nabity, J Daily, B Vanpoppel, and B Spatafore. Actively controlled self-aspirating microelectromechanical (mems) fuel atomizer. Phase I SBIR, Contract Number OII-0539625, Final Report, Jan 2009.

[120] J Nabity and S Rooney. Mems technology for jet fuel atomization. Technical report, TDA Research, Inc., 2004.

[121] J Nabity, A Wickham, B Windecker, J Daily, and B Spatafore. A mems pulsed injection electrostatic atomizer for small engines. STTR Phase I Technical Final Report, pages 1–55, Mar 2009.

[122] James Nabity. Mems jet fuel atomizer. Technical report, TDA Research, Inc., Jan 2004.

[123] James Nabity. Mems jet fuel atomizer. AF Phase I Final Report, pages 1–39, Mar 2005.

[124] James Nabity. The Miniaturization of the Colloid Thruster to the Micro Scale. PhD thesis, Jan 2007.

[125] James Nabity. NSF Phase I STTR. Dec 2007.

[126] NK Nayyab and GS Murty. The flattening of dielectric liquid drop in a uniform electric field. Proceedings of the National Institute of Sciences of India, page 373, 1959.

[127] NT Nguyen and X Huang. Numerical simulation of pulse-width-modulated micropumps with diffuser/nozzle elements. Technical Proc. of the Int. Conf. on Modeling and Simulation of Microsystems (San Diego, CA, pages 636–9, 2000.

[128] G Nhumaio and A Watkins. Simulation of electrosprays in model direct-injection spark-ignition engine in-cylinder flows. International Journal of Engine Research, 6(6):527–546, Apr 2005.

[129] A Olsson, G Stemme, and E Stemme. A valve-less planar fluid pump with two pump chambers. Sensors & Actuators: A. Physical, 47(1-3):549–556, 1995.

[130] A Olsson, G Stemme, and E Stemme. Micromachined diffuser/nozzle elements for valve-less pumps. Micro Electro Mechanical Systems, 1996, MEMS'96, Proceedings.'An Investigation of Micro Structures, Sensors, Actuators, Machines and Systems'. IEEE, The Ninth Annual International Workshop on, pages 378–383, 1996.

[131] A Olsson, G Stemme, and E Stemme. Simulation studies of diffuser and nozzle elements for valve-less micropumps. Solid State Sensors and Actuators, 1997. TRANSDUCERS'97 Chicago., 1997 International Conference on, 2, 1997.

[132] A Olsson, G Stemme, and E Stemme. A numerical design study of the valveless diffuser pump using a lumped-mass model. J. Micromech. Microeng., Jan 1999.

[133] E. Olsson and G. Kreiss. A conservative level set method for two phase flow. Journal of Computational Physics, 210(1):225–246, 2005.

[134] Stanley Osher and Ronald P. Fedkiw. Level set methods and dynamic implicit surfaces. Springer, 2002.

[135] M Pai, O Desjardins, and H Pitsch. Modeling primary break-up of turbulent liquid jets in cross-flow using detailed numerical simulation. American Physical Society, Jan 2008.

[136] M Pai, H Pitsch, and O Desjardins. Detailed numerical simulations of primary atomization of liquid jets in crossflow. In 47th AIAA Aerospace Sciences Meeting, Mar 2009.

[137] LS Pan, TY Ng, XH Wu, and HP Lee. Analysis of valveless micropumps with inertial effects. J. Micromech. Microeng., 13(3):390–399, 2003.

[138] S Yoon S Heister H. Park. A nonlinear atomization model for computation of drop size distributions and spray simulations. Int. J. Numer. Meth. Engng, 48:1–22, Jul 2005.

[139] T.L Pham and S.D Heister. Spray modeling using lagrangian droplet tracking in a homogeneous flow model. Journal of Atomization and Sprays, 12:687–707, Feb 2002.

[140] Charles D Pierce. Progress-variable approach for large-eddy simulation of turbulent combustion. Ph.D. Thesis, Stanford University, 2001.

[141] H Pitsch and O Desjardins. An accurate conservative level set/ghost fluid method for the simulation of turbulent primary atomization. American Physical Society, Jan 2007.

[142] H Pitsch and O Desjardins. Detailed simulation of atomizing liquid jets using a spectrally refined interface (sri) approach. American Physical Society, Jan 2008.

[143] H Pitsch, O Desjardins, G Balarac, and M Ihme. Large-eddy simulation of turbulent reacting flows. Progress in Aerospace Sciences, Jan 2008.

[144] Stephen B Pope. Turbulent Flows. Cambridge University Press, Jan 2008.

[145] B. Van Poppel, O. Desjardins, and J.W. Daily. A Ghost Fluid, Level Set Methodology for Simulating Electrohydrodynamic Atomization of Liquid Fuels. submitted to Journal of Computational Physics, 2010.

[146] B. Van Poppel, O. Desjardins, and J.W. Daily. Modeling two-phase electrohydrodynamic flows. In 48th Annual AIAA Aerospace Sciences Meeting. AIAA, January 5-8 2010.

[147] B. Van Poppel, B. Spatafore, J.W. Daily, and J. Nabity. Simulation of an electrostatically driven mems fuel pump. 47th Annual AIAA Aerospace Sciences Meeting, 2009.

[148] V Raman, H Koo, and O Desjardins. Les/filtered-density function approach for turbulent spray combustion. American Physical Society, Jan 2007.

[149] L Rayleigh. On the capillary phenomena of jets. Proceedings of the Royal Society of London, Jan 1879.

[150] Lord Rayleigh. On the equilibrium of liquid conducting masses. Philisophical Magazine, Series 5, 14:184–186, Apr 1882.

[151] R Reitz and R Diwaker. Effect of drop breakup on fuel sprays. Society of Automotive Engineers international congress and exposition, Jan 1986.

[152] S. N Reznik, A. L Yarin, A Theron, and E Zussman. Transient and steady shapes of droplets attached to a surface in a strong electric field. J. Fluid Mech., 516:349–377, Oct 2004.

[153] A Rigit and J Shrimpton. Electrical performance of charge injection electrostatic atomizers. Journal of Atomization and Sprays, pages 1–20, Dec 2006.

[154] A Rigit and J Shrimpton. Spray characteristics of charge injection electrostatic atomizers with small-orifice diameters. Journal of Atomization and Sprays, 16:1–22, Dec 2006.

[155] NJ Rivette and JC Baygents. A note on the electrostatic force and torque acting on an isolated body in an electric field. Chemical Engineering Science, 51(23):5205–5211, 1996.

[156] AJ Rulison and RC Flagan. Scale-up of electrospray atomization using linear arrays of taylor cones. Review of Scientific Instruments, 64(3):683, 1993.

[157] AJ Rulison and RC Flagan. Electrospray atomization of electrolytic solutions. Journal of Colloid and Interface Science, 167(1):135–145, 1994.

[158] D Saville. Electrohydrodynamic stability: effects of charge relaxation at the interface of a liquid jet. Journal of Fluid Mechanics, 48(4):815–827, 1971.

[159] DA Saville. Electrohydrodynamics: the taylor-melcher leaky dielectric model. Annual Review of Fluid Mechanics, 29(1):27–64, 1997.

[160] R Scardovelli and S Zaleski. Direct numerical simulation of free-surface and interfacial flow. Annual Review of Fluid Mechanics, 31(1):567–603, 1999.

[161] PK Senecal, DP Schmidt, I Nouar, CJ Rutland, RD Reitz, and ML Corradini. Modeling high-speed viscous liquid sheet atomization. International Journal of Multiphase Flow, 25(6-7):1073–1097, 1999.

[162] James Albert Sethian. Level set methods and fast marching methods. Cambridge University Press, 1999.

[163] Yair Shapira. Matrix-Based Multigrid. Springer, 2007.

[164] JD Sherwood. Breakup of fluid droplets in electric and magnetic fields. J. Fluid Mech, 188:133–146, 1988.

[165] John Shrimpton. Charge Injection Systems: Physical Principles, Experimental and Theoretical Work. Springer-Verlag, 2009.

[166] J.S. Shrimpton. Pulsed charged sprays: application to disi engines during early injection. Int. J. Numer. Meth. Engng, 58(3), Jan 2003.

[167] J.S. Shrimpton and A. Kourmatzis. Direct numerical simulation of forced flow dielectric ehd within charge injection atomizers. IEEE Transactions on Dielectrics and Electrical Insulation, pages 1–8, Jan 2010.

[168] J.S. Shrimpton and Y. Laoonual. Dynamics of electrically charged transient evaporating sprays. Int. J. Numer. Meth. Engng, 67(8), 2006.

[169] J.S. Shrimpton and A.J. Yule. Characterisation of charged hydrocarbon sprays for application in combustion systems. Experiments in Fluids, 26(5):460–469, Jan 1999.

[170] J.S. Shrimpton and A.J. Yule. Atomization, combustion, and control of charged hydrocarbon sprays. Journal of Atomization and Sprays, 11:365–396, Feb 2001.

[171] J.S. Shrimpton and A.J. Yule. Electrohydrodynamics of charge injection atomization: Regimes and fundamental limits. Journal of Atomization and Sprays, 13:173–190, Feb 2003.

[172] J.S. Shrimpton and A.J. Yule. Design issues concerning charge injection atomizers. Journal of Atomization and Sprays, 14:127–142, Feb 2004.

[173] V Singhal, SV Garimella, and JY Murthy. Low reynolds number flow through nozzle-diffuser elements in valveless micropumps. Sensors & Actuators: A. Physical, 113(2):226–235, 2004.

[174] Vishal Singhal. Numerical characterization of low reynolds number flow through the nozzle-diffuster element in a valveless micropump. Unpublished., pages 1–8, Apr 2002.

[175] Sun Soft. Fortran 90 User's Guide, May 1995.

[176] C Sozou. Electrohydrodynamics of a pair of liquid drops. J. Fluid Mech., 67:339–348, 1975.

[177] B. Spatafore, B. VanPoppel, J.W. Daily, and J. Nabity. A pulsed injection, electrostatic atomizer for small internal combustion engines. In 45th AIAA/ASME/ASEE Joint Propulsion Conference and Exhibit, Denver, Colorado, Aug 2009.

[178] E Stemme and G Stemme. A valveless diffuser/nozzle-based fluid pump. Sensors and actuators. A, Jan 1993.

[179] M Sussman, K Smith, M Hussaini, and M Ohta. A sharp interface method for incompressible two-phase flows. Journal of Computational Physics, Jan 2007.

[180] K Tang and A Gomez. On the structure of an electrostatic spray of monodisperse droplets. Physics of Fluids, 6(7):2317–2332, Jan 1994.

[181] John C. Tannehill, Dale Arden Anderson, and Richard H. Pletcher. Computational fluid mechanics and heat transfer. Taylor and Francis, 1997.

[182] Y Tatemoto, R Ishikawa, M Takeuchi, T Takeshita, K Noda, and T Okazaki. An electrospray method using a multi-capillary nozzle emitter. Chem. Eng. Technol., 30(9):1274–1279, Sep 2007.

[183] G Taylor. Studies in electrohydrodynamics. i. the circulation produced in a drop by electrical field. Proceedings of the Royal Society of London. Series A, Mathematical and Physical Sciences (1934-1990), 291(1425):159–166, 1966.

[184] Geoffrey Taylor. Disintegration of water drops in an electric field. Proceedings of the Royal Society of London. Series A, Mathematical and Physical Sciences (1934-1990), 280(1382):383–397, Jun 1965.

[185] Stephen Timoshenko and S Woinowsky-Krieger. Theory of Plates and Shells. McGraw-Hill, Jan 1959.

[186] G Tomar, D Gerlach, G Biswas, N Alleborn, A Sharma, F Durst, SWJ Welch, and A Delgado. Two-phase electrohydrodynamic simulations using a volume-of-fluid approach. Journal of Computational Physics, 227(2):1267–1285, 2007.

[187] H Chen C Trinh. Modeling of turbulence effects on liquid jet atomization and breakup. 43rd AIAA Aerospace Sciences Meeting, pages 1–21, Feb 2005.

[188] TQ Truong and NT Nguyen. Simulation and optimization of tesla valves. Technical Proceedings of the 2003 Nanotechnology Conference and Trade Show (NanoTech 2003), pages 178–181.

[189] O.V. Vasilyev. High order finite difference schemes on non-uniform meshes with good conservation properties. Journal of Computational Physics, 157(2):746–761, 2000.

[190] F Vega and AT Perez. Instability in a non-ohmic/ohmic fluid interface under a perpendicular electric field and unipolar injection. Phys. Fluids, 14:2738, 2002.

[191] F Vega, AT Perez, FJ Garcia, and A Castellanos. Perpendicular-field ehd instabilities visualized in a tip-plane configuration. Electrical Insulation and Dielectric Phenomena, 2002 Annual Report Conference on, pages 216–219, 2002.

[192] E Villermaux. Fragmentation. 2006.

[193] L Wang, R Stevens, A Malik, P Rockett, M Paine, P Adkin, S Martyn, K Smith, J Stark, and P Dobson. High-aspect-ratio silica nozzle fabrication for nano-emitter electrospray applications. Microelectronic Engineering, 84(5-8):1190–1193, 2007.

[194] H Watanabe, T Matsuyama, and H Yamamoto. Experimental study on electrostatic atomization of highly viscous liquids. Journal of Electrostatics, 57(2):183–197, 2003.

[195] P Woias. Micropumps: summarizing the first two decades. Proceedings of SPIE, 4560:39, 2001.

[196] P Woias. Micropumps—past, progress and future prospects. Sensors & Actuators: B. Chemical, 105(1):28–38, 2005.

[197] H Wong, D Rumschitzki, and C Maldarelli. On the surfactant mass balance at a deforming fluid interface. Phys. Fluids, Jan 1996.

[198] Herbert H. Woodson and James R. Melcher. Electromechanical Dynamics. John Wiley and Sons, Inc., Jan 1968.

[199] P.K. Wu and G.M. Faeth. Aerodynamic effects on primary breakup of turbulent liquids. Atomization and Sprays, 3(3):265–289, 1993.

[200] Q Xu, D Cheng, G Trapaga, N Yang, and EJ Lavernia. Numerical analyses of fluid dynamics of an atomization configuration. J. Mater. Res, 17(1):157, 2002.

[201] Kai-Shing Yang, Ing-Young Chen, Bor-Yuan Shew, and Chi-Chuan Wang. Investigation of the flow characteristics within a micronozzle/diffuser. J. Micromech. Microeng., 14(1):26–31, Aug 2003.

[202] Yong Yi and Rolf D Reitz. A one-dimensional breakup model for low-speed jets. Journal of Atomization and Sprays, 12:667–685, Feb 2002.

[203] P Young and K Mohseni. Calculation of dep and ewod forces for application in digital microfluidics. J. Fluids Eng., Jan 2008.

[204] A.J Yule, J S Shrimpton, and W Watkins. Electrostatically atomized hydrocarbon sprays. Fuel, 74(7), Jul 1994.

[205] Markus Zahn. Drift-dominated conduction within an ohmic medium. Journal of Applied Physics, 47(7):3122, Jan 1976.

[206] J Zeleny. The electrical discharge from liquid points, and a hydrostatic method of measuring the electric intensity at their interfaces. Physical Review, III(2), 1914.

[207] J Zeleny. Instability of electrified liquid surfaces. Proc. Camb. Philos. Soc Phys Rev, Jan 1915.

[208] H. B Zhang, M. J Edirisinghe, and S. N Jayasinghe. Flow behaviour of dielectric liquids in an electric field. J. Fluid Mech., 558:103, Jul 2006.

[209] J Zhang and D Kwok. A 2d lattice boltzmann study on electrohydrodynamic drop deformation with the leaky dielectric theory. Journal of Computational Physics, 206:150–161, Jan 2005.